# Collected figures from HELIOPHYSICS IV. ACTIVE STARS, THEIR ASTROSPHERES, AND IMPACTS ON PLANETARY ENVIRONMENTS

*edited by*
*CAROLUS J. SCHRIJVER,*
Lockheed Martin Advanced Technology Center

*FRANCES BAGENAL*
University of Colorado

and

*JAN J. SOJKA*
Utah State University

This document contains the figures from the published volume of Heliophysics IV as submitted to Cambridge University Press, prior to possible revisions in the graphics and captions during the copy editing process. This collection is intended only as an aid to students and teachers for use in, e.g., lectures and study sessions.

# Contents

*Margaret G. Kivelson*

# 1

# Introduction

*Carolus J. Schrijver, Frances Bagenal, and Jan J. Sojka*

## 1.1 Chapter outlines

Chapter 2 discusses explosive events on the Sun and stars like the Sun in temperature and internal structure. These involve the changing of magnetic configurations and subsequent liberation of energy. The chapter reviews how flares manifest themselves differentially across the electromagnetic spectrum - from hard X-rays to radio - and the difficulty in observing any associated energetic particles and coronal mass ejections that propagate into astrospheres. The sections in this chapter discuss key stellar and wavelength-dependent parameters important to a discussion of explosive events. The examination of explosive events proceeds as a function of the star's age, from birth to beyond the current age of the Sun, with energies of over a thousand times that of the largest solar flares down to flares that disappear in the background atmospheric emission of the Sun-like "cool stars."

Chapter 3 discusses interactions of stars with their galactic environment, in the context of how that might affect orbiting planets. The characteristics of astrospheres depend on the properties of the stellar winds and on those of the interstellar medium (ISM) into which the winds are expanding. The chapter therefore includes a discussion of what is known about stellar winds and how they evolve with time, and a discussion of different sorts of ISM within the Galaxy. Particular attention is given to our own Sun and to the surrounding heliosphere as it is carved out of the ISM by the solar wind. Observational studies of global heliospheric structure are reviewed, and speculation is offered as to how this heliospheric structure might change in response to different ISM environments and long-term solar wind evolution.

Chapter 4 reviews how changes in stellar magnetic activity of Sun-like stars

throughout their evolution translate into changes in their stellar winds, the structure of their interplanetary space, as well as of their astrospheres, the transport of particles, and the propagation and evolution of CMEs. Young, rapidly spinning stars have strong high-latitude fields and substantial effects of rotational forces in their winds. Old, slowly-spinning stars have winds with fields would up into the Parker-spiral pattern characteristic of the heliospheric structure. All stars likely exhibit coronal mass ejections (CMEs) that contribute in different degrees to stellar angular momentum loss. CMEs and the background stellar winds affect the evolution of planetary atmospheres, and the activity of planetary magnetospheres, depending also on the planet's orbital radius. The strength, pattern, and dynamics of asterospheric fields changes the galactic cosmic ray (GCR) population that penetrates deep into astrospheres; Earth has been subjected to the associated changes in GCR intensities and energy spectra over its 4.5-billion year history.

Chapter 5 focuses on exoplanet systems. Search techniques for exoplanets include Doppler measurements, transit photometry, micro-lensing, direct imaging and astrometry. Each detection technique has some type of observational incompleteness that imposes a biased view of the underlying population of exoplanets. With such partial information, we must piece together an understanding of exoplanet architectures by counting planets in the regimes where techniques are robust and then estimating correction factors when possible. This chapter therefore begins with a review of the exoplanet detection techniques with particular consideration of the observational biases. Only then can we discuss the implications of the rapidly-growing multitude of exoplanet systems for planet formation with an eye toward how our solar system compares. We can begin to address questions about how planetary systems form and evolve: How do planetary systems - including gas and debris disks, and planetary migration by mutual gravitational interactions - evolve over time? In what ways do exoplanetary systems mirror our solar system? How are they different? Does the presence of a binary star affect planet formation? What are the formation histories of "terrestrial" planets and of gas giants? Are Earth analogs common?

Chapter 6 reviews planetary dynamos which produce the magnetospheres that are a crucial component of the study of heliophysics and the interactions of solar and stellar winds with planets. This chapter reviews the current understanding of planetary dynamos, including theoretical foundations, and our knowledge of planetary magnetic fields from spacecraft data. It discusses planetary interior structure and processes responsible for the different magnetic fields seen in the solar system, focusing on recent findings. It also discusses

the possibilities of extrasolar planet magnetic fields and what we can learn about exoplanets from them.

Chapter 7 addresses how a planet's atmosphere and surface habitability are inextricably linked. Life at Earth's surface has been made possible by atmospheric conditions, and has modified them. Planetary climates are not static, but instead change as energy or particles are added or removed from the atmosphere. The Sun plays a large role in shaping climate in a variety of ways. Of particular interest for this volume are heliophysical processes that remove particles from the upper layers of terrestrial planet atmospheres. This chapter describes the present-day climates of Venus, Earth, and Mars, and evidence for how their atmospheres have changed over time. The present understanding of the role of heliophysical processes in driving these changes is summarized. Special attention is paid to how atmospheric escape varies with changes in solar photon fluxes, solar wind, and the interplanetary magnetic field, and the role of global-scale planetary magnetic fields in inhibiting escape. We discuss the importance of applying lessons from the terrestrial planets to exoplanetary atmospheres.

Chapter 8 reviews how the upper atmospheres of planets represent a key transition region between a dense atmosphere below and a tenuous space environment above. An array of complex coupling processes from below and from above lead to a highly coupled system, with neutrals, plasmas, and electromagnetic processes linking surfaces to magnetospheres and to the solar wind, and ultimately to the Sun itself. Evidence of these coupling processes includes various upper atmospheric emissions, such as dayglow and nightglow, resulting from the absorption of solar photons, and aurorae, produced from the energy deposition of energetic particles from the space environment. The chapter gives an overview of the current state of knowledge of giant planet atmospheres, first focusing on thermospheres and ionospheres, next on the processes coupling planetary atmospheres and magnetospheres, and finally on the auroral emissions resulting from those coupling processes. Giant planet aurorae are spectacular displays of magnetosphere-atmosphere coupling, the most powerful in the solar system. Furthermore, by studying the giant planets in our own neighborhood we can lay a solid foundation for understanding the rapidly accumulating zoo of exoplanets.

Chapter 9 reviews how upper atmospheres of terrestrial planets are affected by processes from above and from below. One of the new paradigms in solar-terrestrial research is that meteorological forcing from the lower atmospheres of planets can affect planetary upper atmospheres and drive space weather. Concurrently, general circulation models of planetary lower atmospheres are being coupled with planetary thermospheres and ionospheres. We are thus

witnessing the beginning of the era of whole atmosphere modeling of space weather. Ultimately, these whole atmosphere models will be linked to heliophysics models to produce true solar-terrestrial simulation systems. This chapter focuses on the specific phenomena which have been recently identified to couple the lower atmospheres of terrestrial planets, mainly Earth and Mars, with their respective upper atmospheres and ionospheres. It describes the basic state of terrestrial planetary upper atmospheres and ionospheres and how they depend upon atmospheric composition. It also discusses specific differences between the two worlds such as Martian dust storms or effects from the differing magnetic field environment of both planets.

Chapter 10 explores couplings between smaller bodies in the solar system and their space environment. A body such as a planet, a moon, an asteroid, or a comet, typically enveloped in a tenuous neutral gas, perturbs its surroundings in a flowing, magnetized plasma. The structure of field and plasma resulting from the interaction depends on properties of the ambient plasma, of the atmosphere and internal structure of the body onto which the plasma flows, and on the relative speeds expressed in terms of propagation velocities of acoustic and magnetohydrodynamic waves. This chapter addresses the interaction of solar system plasmas with a number of small bodies of the solar system by exploring magnetohydrodynamic couplings as a function of several dimensionless numbers. The interaction regions surrounding the small bodies of interest vary in global geometric configuration, in spatial extent relative to the size of the central body, and in the nature of the plasma disturbances.

Chapter 11 starts with an introduction of selected heliospheric observations that indicate dusty plasma effects on the flow of interstellar dust through the heliosphere, the effects of dust impacts on electric field measurements on spacecraft, and on the ion composition of the solar wind. After describing the basic dust charging processes, the chapter describes the unusual dynamics of charged dust particles in planetary magnetospheres, and the possible role dusty plasma waves might play in cometary environments. Dust particles immersed in plasmas and UV radiation collect electrostatic charges and respond to electromagnetic forces in addition to all the other forces acting on uncharged grains. Simultaneously, dust can alter its plasma environment as it can act both as a sink and a source of ions, and electrons. Dust particles in plasmas are unusual charge carriers. They are many orders of magnitude heavier than any other plasma particles, and they can have time-dependent (positive or negative) charges that are many orders of magnitude larger. Their presence can influence the collective plasma behavior, for example, by altering the traditional plasma wave modes and by triggering new types of waves

and instabilities. Dusty plasmas represent the most general form of space, laboratory, and industrial plasmas.

Chapter 12 argues that energetic-particle environments in the solar system are fundamental to understand the plasma physics processes in our universe. Energetic ions and electrons are found everywhere in the heliosphere and beyond. The knowledge of their composition, energy and spatial distributions in different plasma environments provide an enormous source of information to investigate the origin, evolution, and current state of our solar system. Originating outside and inside the heliosphere the distribution of energetic particles is widely used to study acceleration phenomena in space near shocks, to study the configuration and dynamics of planetary magnetospheres, atmospheres, rings, neutral gas and dust clouds in the vicinity of planets and moons. They are also very important to study the interaction processes between planets/moons and their local plasma environment and can help to discover formerly unknown objects.

Chapter 13 explores how remote sensing can tell us about tenuous environments, primarily by focusing on radio waves as diagnostics. The density irregularities in the solar wind can be observed by remote sensing techniques using ground-based or space-based coronagraphs for the inner solar wind as it emerges from the Suns corona, by space-based white-light heliospheric imagers, and by radio observations of distant compact radio sources to indirectly observe the solar wind through scintillation and Faraday rotation in the radio signal received from distant astronomical or artificial radio sources. This chapter focuses on the development of radio scintillation methods since the middle of the 20th Century, from localized observations of irregularities along particular source directions with a single antenna, to large-scale, three-dimensional, evolving tomographic modeling of outflow velocities and density structures throughout large parts of the inner heliosphere including the inclusion and determination of magnetic fields, that can utilize multi-antenna, multi-wavelength observational methods.

Table 1.1. *Titles of the volumes in the Heliophysics series. References in this volume to chapters in other volumes use the numbering as in this table.*

| Volume | Title and focus |
|--------|-----------------|
| I | Plasma physics of the local cosmos |
| II | Space storms and radiation: causes and effects |
| III | Evolving solar activity and the climates of space and Earth |
| IV | Active stars, their astrospheres, and impacts on planetary environments |
| V* | Space weather and society |

* Available on line at
http://www.vsp.ucar.edu/Heliophysics/science-resources-textbooks.shtml

Table 1.2. *Chapters and their authors in the Heliophysics series sorted by theme (continued on the next page), not showing introductory chapters.*

| Universal and fundamental processes, diagnostics, and methods |
|---|
| I.2. Introduction to heliophysics ........................................ *T. Bogdan* |
| I.3. Creation and destruction of magnetic field ........................ *M. Rempel* |
| I.4. Magnetic field topology ......................................... *D. Longcope* |
| I.5. Magnetic reconnection ............................................ *T. Forbes* |
| I.6. Structures of the magnetic field ........................... *M. Moldwin* et al. |
| II.3 In-situ detection of energetic particles .......................... *G. Gloeckler* |
| II.4 Radiative signatures of energetic particles ........................ *T. Bastian* |
| II.7 Shocks in heliophysics ............................................ *M. Opher* |
| II.8 Particle acceleration in shocks ........................... *D. Krauss-Varban* |
| II.9 Energetic particle transport .................................... *J. Giacalone* |
| II.11 Energization of trapped particles ................................. *J. Green* |
| IV.11 Dusty plasmas ................................................. *M. Horányi* |
| IV.12 Energetic-particle environments in the solar system .............. *N. Krupp* |
| IV.13 Heliophysics with radio scintillation and occultation ................. *M. Bisi* |

| Stars, their planetary systems, planetary habitability, and climates |
|---|
| III.3 Formation and early evol. of stars and proto-planetary disks .... *L. Hartmann* |
| III.4 Planetary habitability on astronomical time scales .............. *D. Brownlee* |
| III.11 Astrophysical influences on planetary climate systems .............. *J. Beer* |
| III.12 Assessing the Sun-climate relationship in paleoclimate records ... *T. Crowley* |
| III.14 Long-term evolution of the geospace climate ...................... *J. Sojka* |
| III.15 Waves and transport processes in atmosph. and oceans ..... *R. Walterscheid* |
| IV.5 Characteristics of planetary systems ................... *D. Fischer & J. Wang* |
| IV.7 Climates of terrestrial planets ..................................... *D. Brain* |

| The Sun, its dynamo, and its magnetic activity; past, present, and future |
|---|
| I.8. The solar atmosphere .......................................... *V. Hansteen* |
| II.5 Observations of solar and stellar eruptions, flares, and jets ......... *H. Hudson* |
| II.6 Models of coronal mass ejections and flares ........................ *T. Forbes* |
| III.2 Long-term evolution of magnetic activity of Sun-like stars ....... *C. Schrijver* |
| III.5 Solar internal flows and dynamo action .......................... *M. Miesch* |
| III.6 Modeling solar and stellar dynamos ......................... *P. Charbonneau* |
| III.10 Solar irradiance: measurements and models ............ *J. Lean & T. Woods* |
| IV.2 Solar explosive activity throughout the evol. of the solar system ..... *R. Osten* |

Table 1.2. *(Continued from the previous page) Chapters and their authors in the Heliophysics series sorted by theme, not showing introductory chapters.*

| Astro-/heliospheres, the interstellar environment, and galactic cosmic rays |
|---|
| I.7. Turbulence in space plasmas .......................................... *C. Smith* |
| I.9. Stellar winds and magnetic fields ................................. *V. Hansteen* |
| III.8 The structure and evolution of the 3D solar wind .................. *J. Gosling* |
| III.9 The heliosphere and cosmic rays ................................... *J. Jokipii* |
| IV.3 Astrospheres, stellar winds, and the interst. medium .... *B. Wood & J. Linsky* |
| IV.4 Effects of stellar eruptions throughout astrospheres ................. *O. Cohen* |

| Dynamos and environments of planets, moons, asteroids, and comets |
|---|
| I.10. Fundamentals of planetary magnetospheres .................... *V. Vasyliūnas* |
| I.11. Solar-wind magnetosphere coupling ............... *F. Toffoletto & G. Siscoe* |
| I.13. Comparative planetary environments ............................ *F. Bagenal* |
| II.10 Energy conversion in planetary magnetospheres ............... *V. Vasyliūnas* |
| III.7 Planetary fields and dynamos ................................ *U. Christensen* |
| IV.6 Planetary dynamos: updates and new frontiers .................... *S. Stanley* |
| IV.10 Moons, asteroids, and comets interact. with their surround. ..... *M. Kivelson* |

| Planetary upper atmospheres |
|---|
| I.12. On the ionosphere and chromosphere ........ *T. Fuller-Rowell & C. Schrijver* |
| II.12 Flares, CMEs, and atmospheric responses .... *T. Fuller-Rowell & S. Solomon* |
| III.13 Ionospheres of the terrestrial planets ........................... *S. Solomon* |
| III.16 Solar variability, climate, and atmosph. photochemistry ... *G. Brasseur* et al. |
| IV.8 Upper atmospheres of the giant planets ...................... *L. Moore* et al. |
| IV.9 Aeronomy of terrestrial upper atmospheres .......... *D. Siskind & S. Bougher* |

| Technological and societal impacts of space weather phenomena |
|---|
| II.2 Introduction to space storms and radiation ...................... *S. Odenwald* |
| II.13 Energetic particles and manned spaceflight ......... *S. Guetersloh & N. Zapp* |
| II.14 Energetic particles and technology ............................... *A. Tribble* |
| V.2 Space weather: impacts, mitigation, forecasting .................. *S. Odenwald* |
| V.3 Commercial space weather in response to societal needs ........... *W. Tobiska* |
| V.4 The impact of space weather on the electric power grid ............. *D. Boteler* |
| V.5 Radio waves for communication and ionospheric probing .......... *N. Jakowski* |

# 2

# Solar explosive activity throughout the evolution of the solar system

*Rachel Osten*
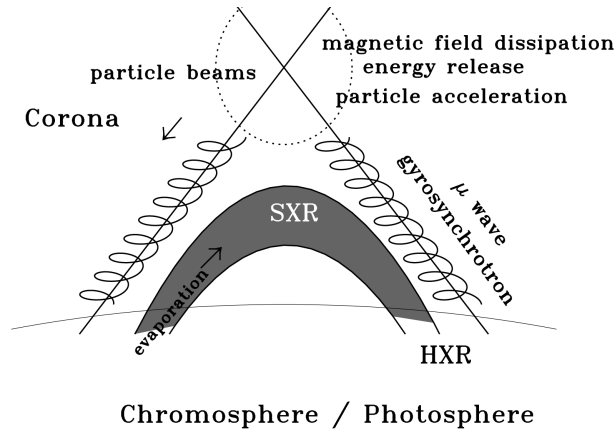
Fig. 2.1. Schematic arrangement in the outer atmosphere of the Sun or a comparable cool star indicating the flow of energy during a flare: a flare starts with magnetic reconnection high in the atmosphere which accelerates particles, leading to motion along field lines upward away from or downward towards the visible surface. Resulting emissions include hard X-rays (HXR), soft X-rays (SXR), and microwave emission. Figure from Osten (2002).
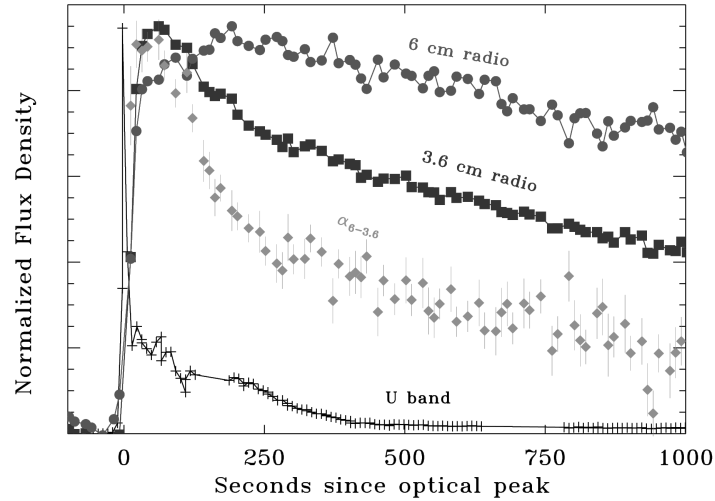
Fig. 2.2. Example radio-optical flare seen on the nearby M dwarf flare star EV Lac (from Osten *et al.*, 2006). Circles and squares show time evolution of radio flux density at wavelengths of 6 and 3.6 cm, respectively. Diamonds show the time variation of the radio spectral index, a measure of the relative strength of emission at the two wavelengths. The plus symbols show the temporal variability of optical emission in the U filter (cf. Fig. 2.5). Because the radio flux arises due to gyrosynchrotron emission from a population of accelerated particles, and the optical emission originates from a black body formed as the result of deposition of accelerated particles in the lower stellar atmosphere, one expects to see a temporal correlation between the two, which is observed for this flare.

Fig. 2.3. Temperature coverage of chromospheric, transition region, and coronal lines from different elements and ionic stages obtained by combining spectra from ultraviolet through X-ray wavelengths; for the stellar case these instruments are the Space Telescope Imaging Spectrograph on the Hubble Space Telescope (HST/STIS), the Far Ultraviolet Spectroscopic Explorer (FUSE), and the Chandra X-ray Observatory High Energy Transmission Grating Spectrometer (HETGS). The elements are ordered in terms of increasing first ionization potential (FIP), a quantity which gives the amount of energy required to remove the outermost electron from an atom of this element. These lines are formed under the conditions of collisional ionization equilibrium, and are generally optically thin, two conditions which permit inversion of their intensities to determine the temperature structure from the upper chromosphere to corona. (Figure from Osten, 2002)
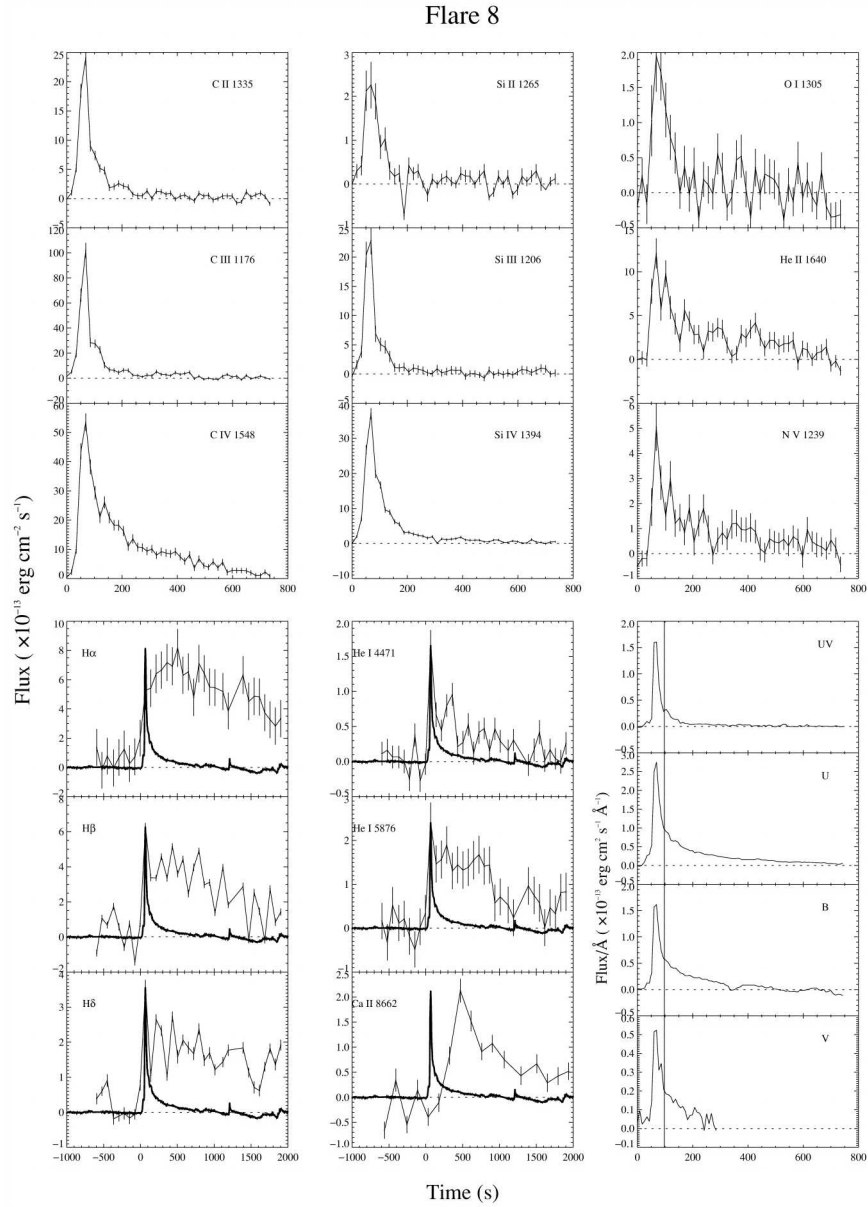
Flare 8



Fig. 2.4. Behavior of emission lines in the optical and ultraviolet during a well-studied flare on the nearby flare star AD Leo (from Hawley *et al.*, 2003). Ultraviolet emission lines (C II, Si II, O I, C III, Si III, He II, C IV, Si IV, N V) have time scales comparable to that seen in the broadband filters (UV, U, B, V) that measure primarily impulsive flare continuum emission. In contrast, the variation of emission lines originating from lower in the stellar atmosphere (H$\alpha$, H$\beta$, H$\delta$, He I, and Ca II) have a delayed response to the flare energy input seen from the hot black body, as well as a longer decay time scale.
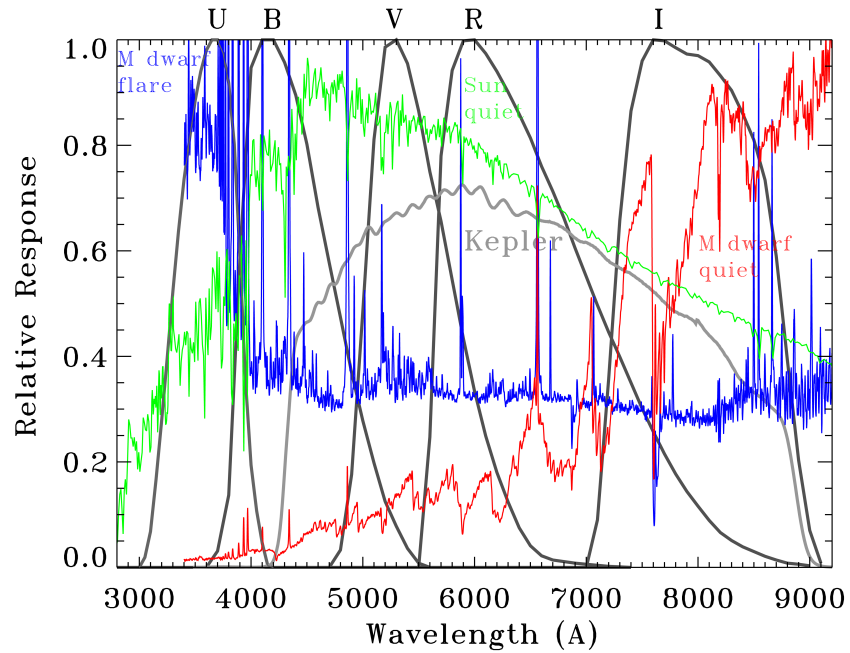
Fig. 2.5. Wavelength coverage of several standard filters used in optical astronomy, along with the wavelength coverage of the filter used in the Kepler mission. Overplotted are also spectral energy distributions of a quiescent and flaring M dwarf atmosphere, taken from Kowalski *et al.* (2013). The solar spectrum is the 1985 Wehrli Standard Extraterrestrial Solar Irradiance Spectrum from http://rredc.nrel.gov/solar/spectra/am0/.
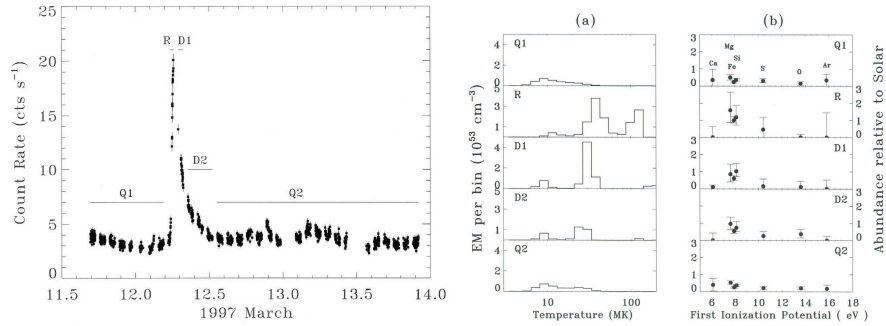
Fig. 2.6. Example stellar flare X-ray light curve *(left)* and corresponding change of temperatures and abundances in the phases of the flare *(right)*. This flare was observed on the active binary system TZ CrB, which is composed of two solar-like stars rotating at a period of 1.1 days (from Osten *et al.*, 2000).
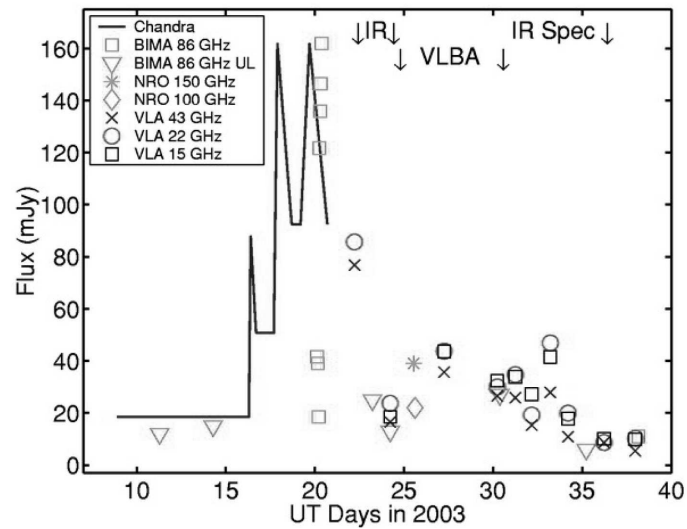
Fig. 2.7. Unusual radio/X-ray flare observed on a pre-main sequence K type star in the Orion Nebula. The strong outburst was observed first at radio wavelengths, then at X-ray wavelengths, in contradiction to the pattern usually seen for solar explosive events. Figure from Bower *et al.* (2003).
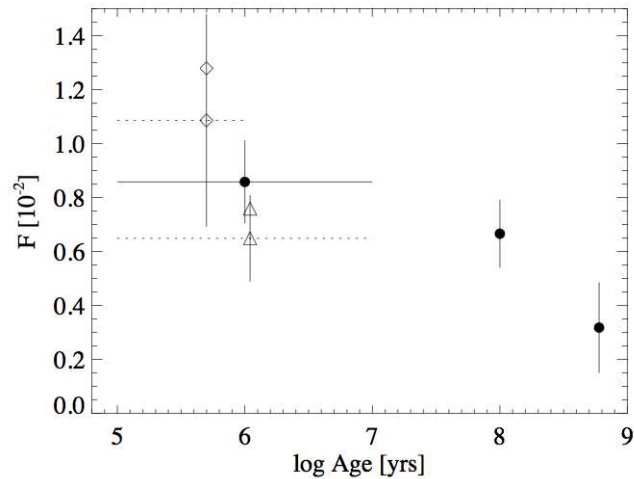
Fig. 2.8. X-ray flare rate expressed as a percent of observing time for stars of different ages, from the study of Stelzer *et al.* (2000). The sensitivity to flares is set to a uniform value to account for the differing distances. Diamonds indicate classical T Tauri stars, triangles weak-lined T Tauri stars. The horizontal line gives the age spread of the young stellar objects. There is a clear drop in flare rate by the age of the Hyades (800 Myr).
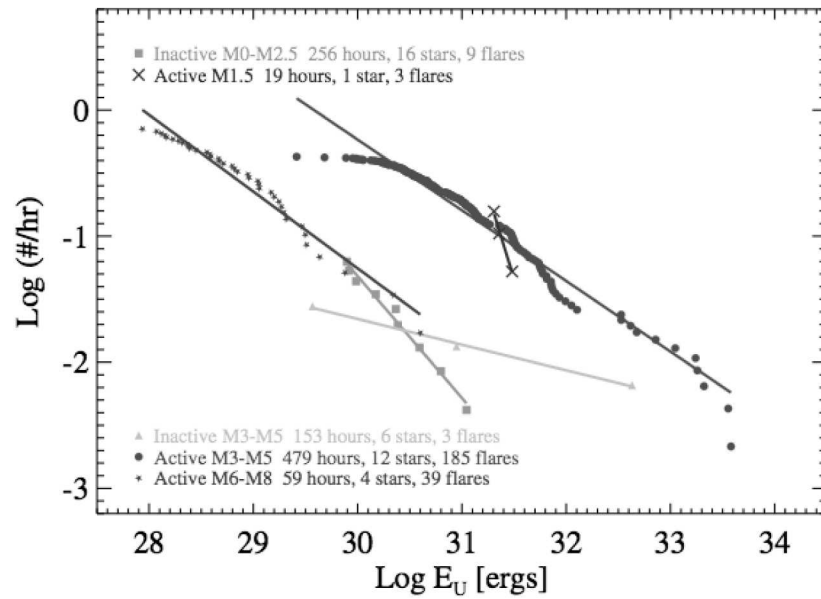
Fig. 2.9. Cumulative flare frequency distributions for different categories of M dwarfs, from the PhD thesis of Eric Hilton. Through long stares at different classes of M dwarfs, the difference in the occurrence rate of flares of different U band energies can be determined.
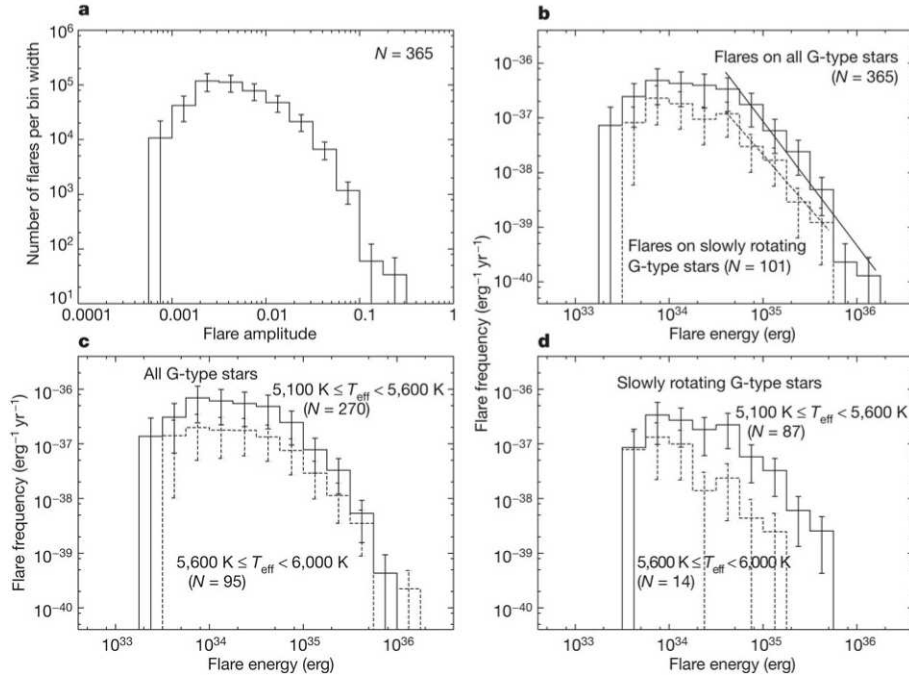
Fig. 2.10. Summary of flare characteristics seen on G-type stars from Maehara *et al.* (2012). *(top left)* The peak flare amplitudes are 10% or less of the star's underlying brightness. *(top right)* The distribution of flares with energy on slowly rotating stars appears similar to that of all G-type stars surveyed. *(bottom left)* The distribution of flares with energy appears similar when breaking the stars up in hotter vs. cooler stars. *(bottom right)* The slowly rotating hot stars show a decrease in flare frequency.
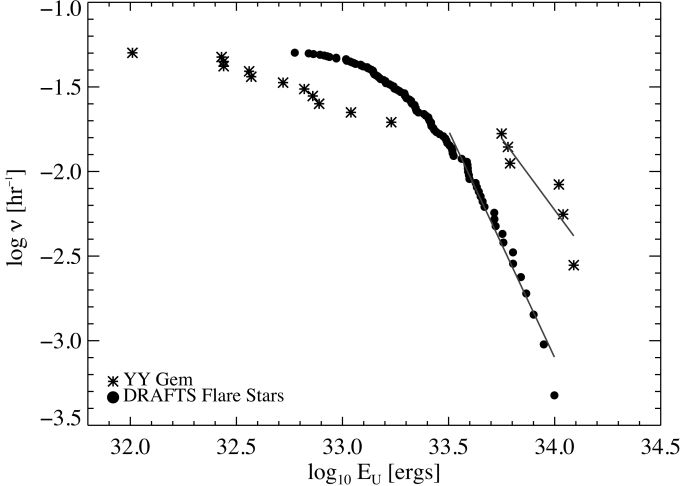
Fig. 2.11. Flare frequency distribution of flares observed on 10-Gyr stars in the Galactic bulge. (From Osten *et al.*, 2012).

# 3

# Astrospheres, stellar winds, and the interstellar medium

*Brian Wood and Jeffrey L. Linsky*
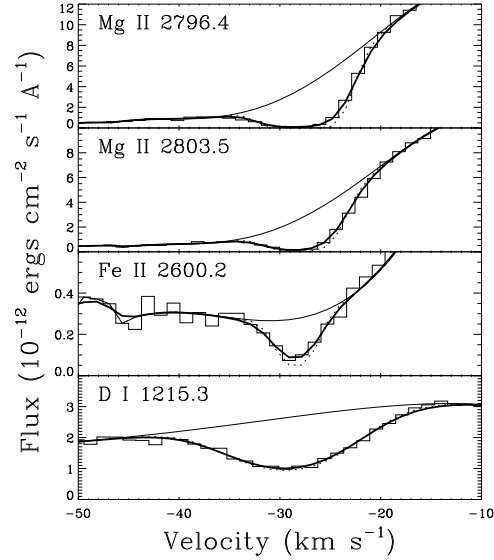
Fig. 3.1. High-resolution spectra of the star 36 Oph showing interstellar absorption in Mg II, Fe II, and D I lines, with wavelengths provided in Å units. The spectra are plotted in a heliocentric rest frame. Note the different absorption widths, with D I being broadest due to deuterium atoms having the lowest mass and therefore the highest thermal speeds. (From Wood et al., 2000)
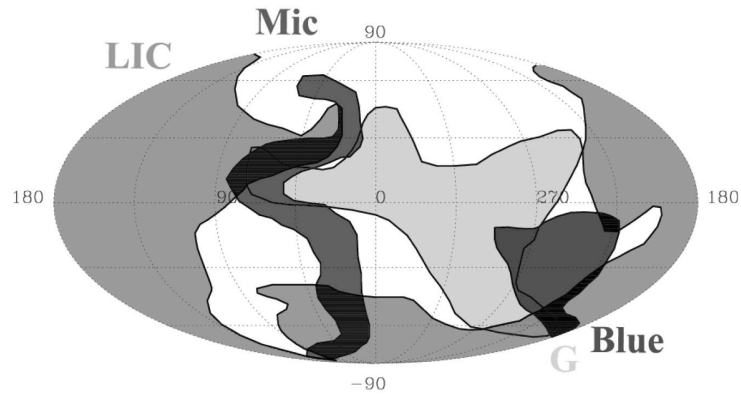
Fig. 3.2. Map in Galactic coordinates of the four partially ionized warm interstellar clouds that are closest to the Sun, mapped using ISM absorption lines. The Sun is likely located inside of the Local Interstellar Cloud (LIC), but very near the edge, explaining why LIC absorption is not detectable in all directions and therefore the ISM absorption lines by the LIC do not fill the sky. (From Redfield and Linsky, 2008)
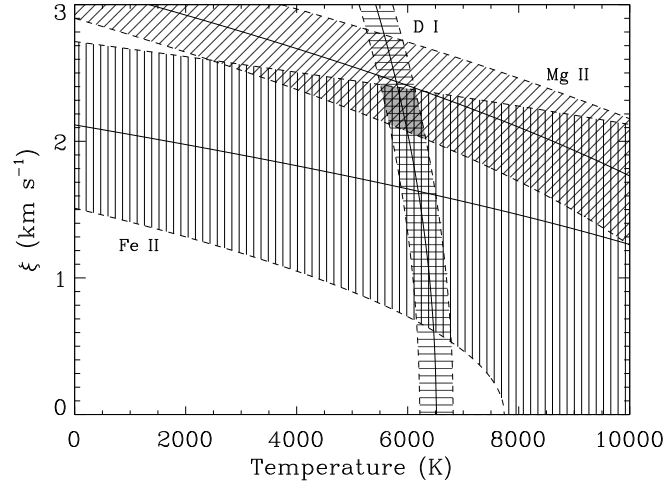
Fig. 3.3. Non-thermal ISM speeds ($\xi$; see Eq. 3.1) plotted versus temperature, based on the Doppler width parameters measured from the lines in Fig. 3.1. The shaded area where the three curves overlap indicates the best temperature and $\xi$ value. (From Wood et al., 2000)
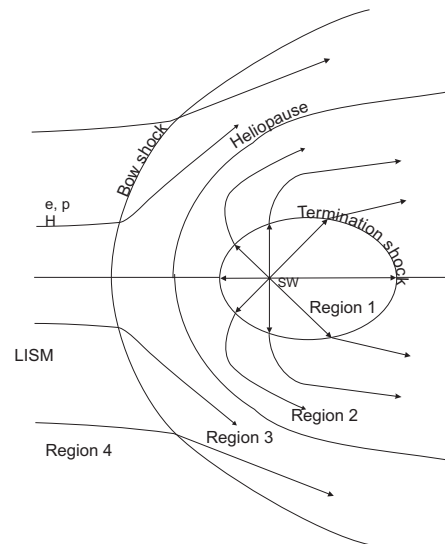
Fig. 3.4. Basic structure of the global heliosphere, with three discontinuities: the termination shock (TS), heliopause (HP), and bow shock (BS). These discontinuities separate the heliosphere into four regions, with significantly different plasma properties: 1. supersonic solar wind; 2. decelerated, heated, and deflected solar wind; 3. decelerated, heated, and deflected ISM, and 4. undisturbed local ISM (LISM) flow, here assumed supersonic, resulting in a bow shock. (From Izmodenov et al., 2002)
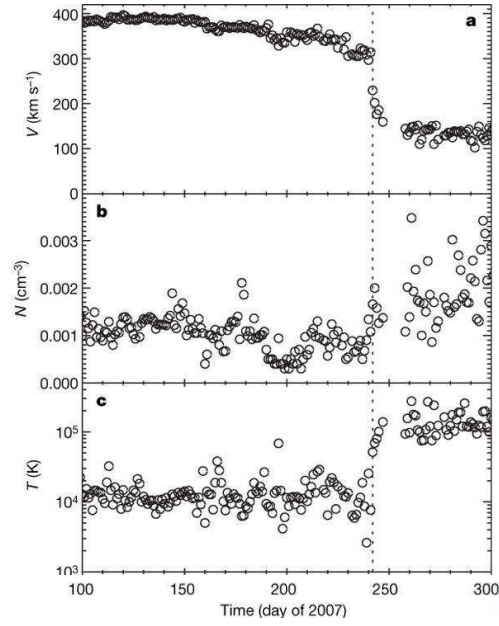
Fig. 3.5. *Voyager 2* observations of solar wind (a) speed, (b) proton number density, and (c) temperature. The dotted line indicates the termination shock (TS) crossing on 2007 August 30 at a distance of 84 AU from the Sun. (From Richardson et al., 2008)
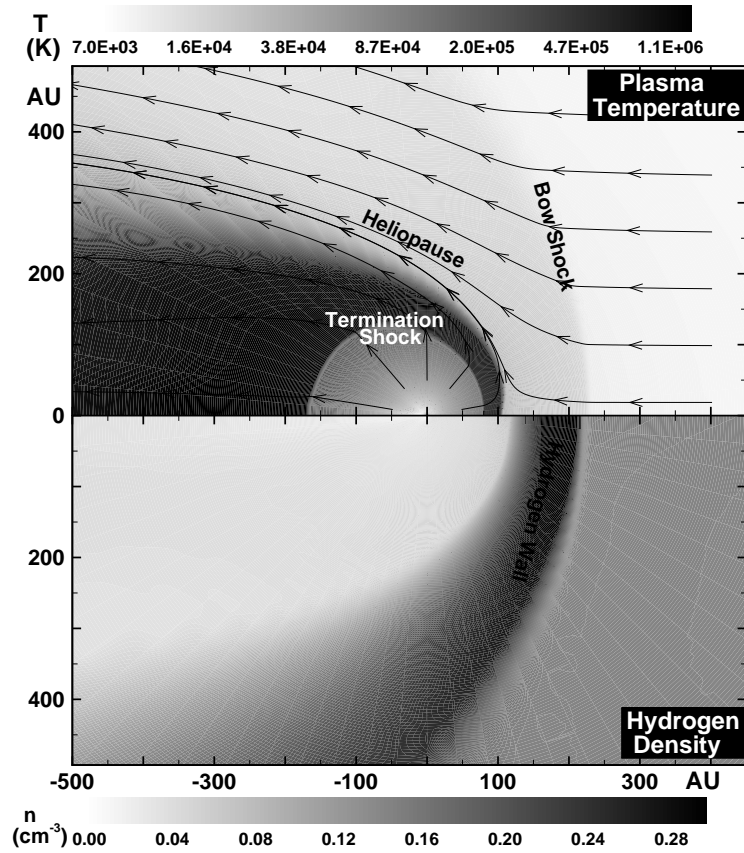
Fig. 3.6. A 2.5D axisymmetric, hydrodynamic model of the heliosphere from Müller & Zank (2004). The upper panel shows plasma temperature, and the bottom panel shows neutral hydrogen density.
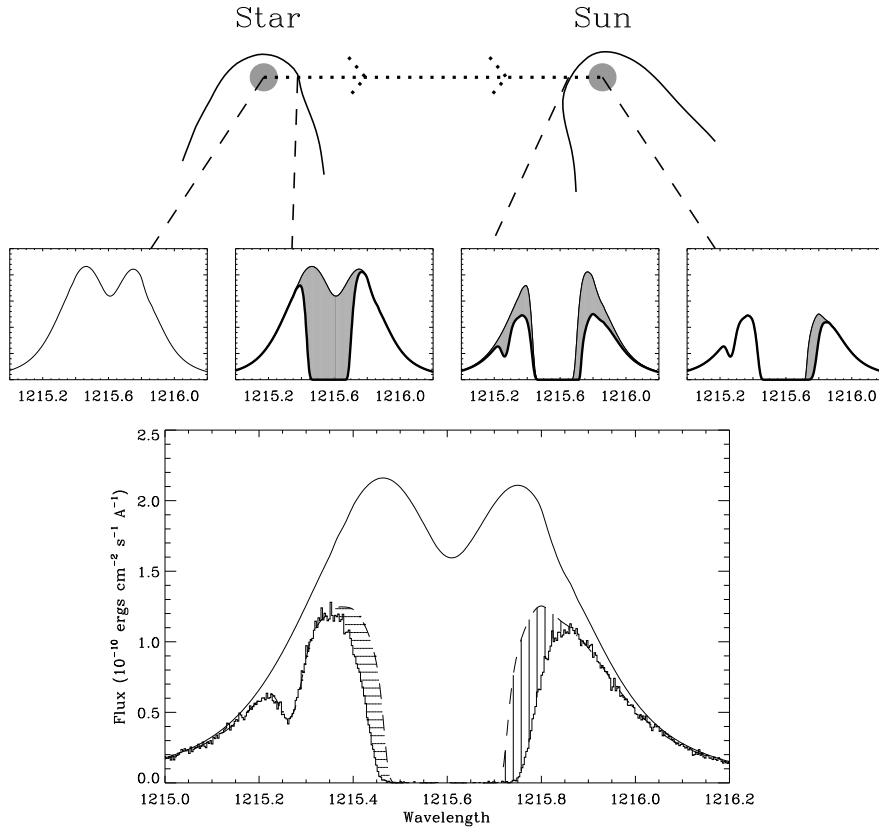
Fig. 3.7. *Top panel:* The journey of a Lyman-$\alpha$ photon from a star through its astrosphere, the interstellar medium, and the heliosphere. *Middle panel from left to right:* The Lyman-$\alpha$ emission line emitted by the star, absorption due to the stellar astrosphere, additional absorption due to the interstellar medium, and additional absorption due to the heliosphere. *Bottom panel:* HST Lyman-$\alpha$ spectrum of $\alpha$ Cen B, showing broad H I absorption at 1215.6 Å and D I absorption at 1215.25 Å. The upper solid line is the assumed stellar emission profile and the dashed line is the ISM absorption alone. The excess absorption is due to heliospheric H I (vertical lines) and astrospheric H I (horizontal lines). (From Wood, 2004)
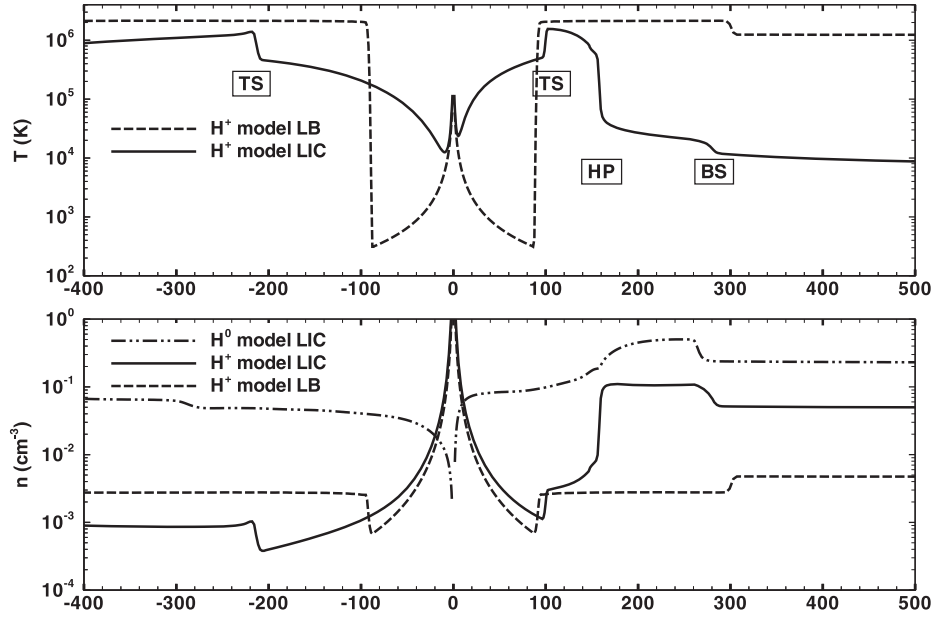
Fig. 3.8. *Top:* Plots of the temperature vs. distance in Sun-Earth distances (astronomical units, or AU) relative to the Sun (interstellar flow upwind direction to the right and downwind to the left) for a heliosphere model with the Sun located inside of the local interstellar cloud (LIC; solid line) or inside a $10^6$ K hot interstellar medium (dashed line). The heliosphere in the LIC model has a termination shock (TS), heliopause (HP) and bowshock (BS) structure. *Bottom:* Density structures for the LIC neutral hydrogen (solid line), LIC protons (dot-dash line), and hot interstellar model protons (dashed line). Note that the hydrogen wall at 150–280 AU exists when the heliosphere is located inside partially neutral interstellar gas but not when it is inside fully ionized interstellar gas. (Figure from Müller *et al.*, 2009)
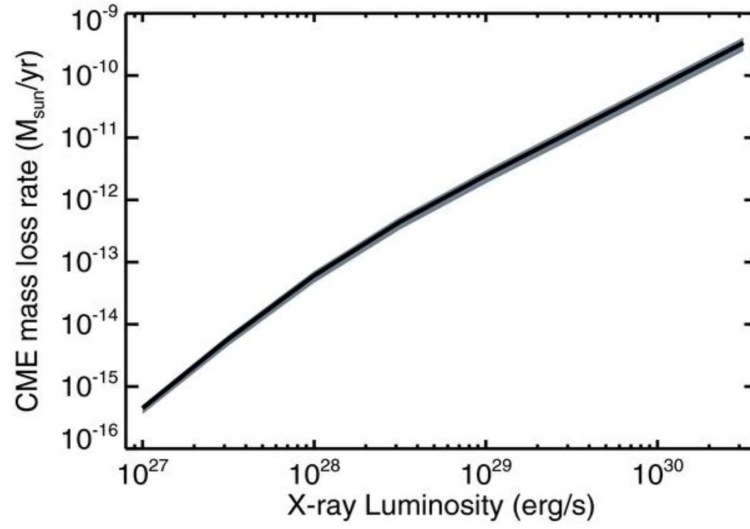
Fig. 3.9. Plausible stellar mass loss rate due to CMEs as a function of coronal X-ray luminosity, computed by assuming that the solar-flare/CME-mass correlation can be extrapolated to younger, more active stars. Note that the solar X-ray luminosity is $L_X \sim 2 \times 10^{27}$ ergs s$^{-1}$. (From Drake *et al.*, 2013)
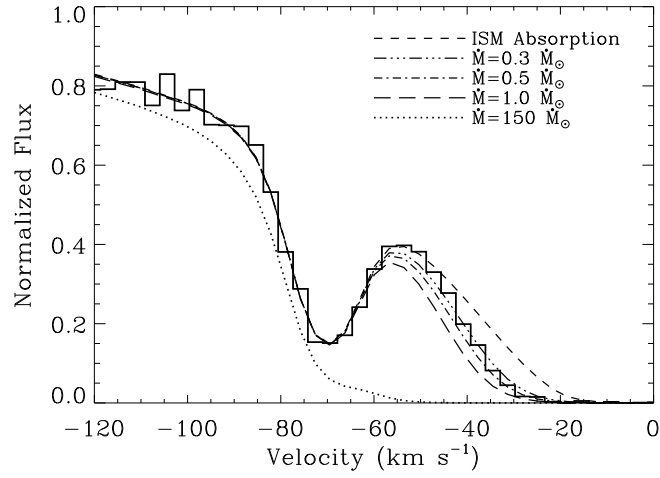
Fig. 3.10. The blue side of the Lyman-$\alpha$ absorption line of $\pi^1$ UMa, plotted on a heliocentric velocity scale. The absorption at $-70$ km s$^{-1}$ is from interstellar D I. Because the ISM absorption cannot explain all of the H I absorption, the excess is assumed to be from the stellar astrosphere. The astrospheric absorption signature is compared with absorption predictions from four hydrodynamic models of the astrosphere, assuming four different mass-loss rates for $\pi^1$ UMa (after the astrospheric absorption is added to that of the ISM). (From Wood *et al.*, 2014)
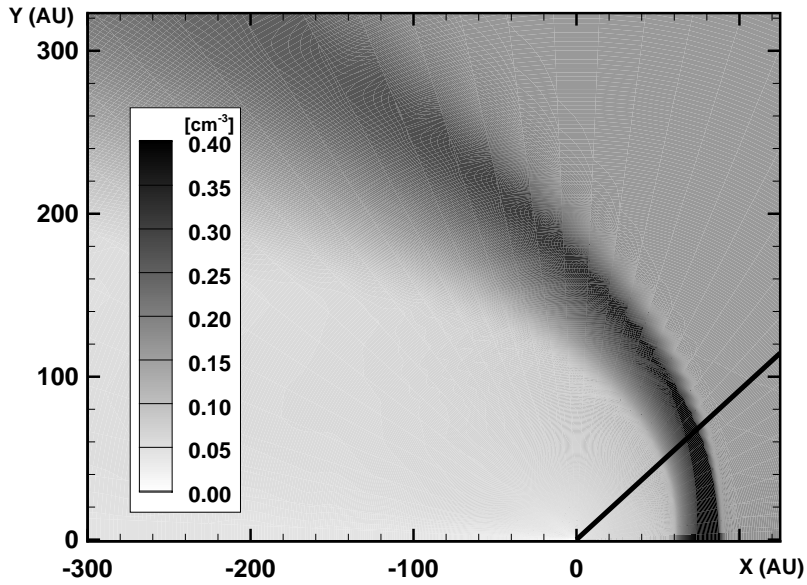
Fig. 3.11. The H I density distribution of a hydrodynamic model of the $\pi^1$ UMa astrosphere, assuming $\dot{M} = 0.5\dot{M}_\odot$, which leads to the best fit to the data in Fig. 3.10. The star is at the origin, and the ISM is flowing from the right in this figure. The "hydrogen wall" is the parabolic shaped high-density region stretching around the star. The black line indicates our line of sight to the star. (From Wood *et al.*, 2014)
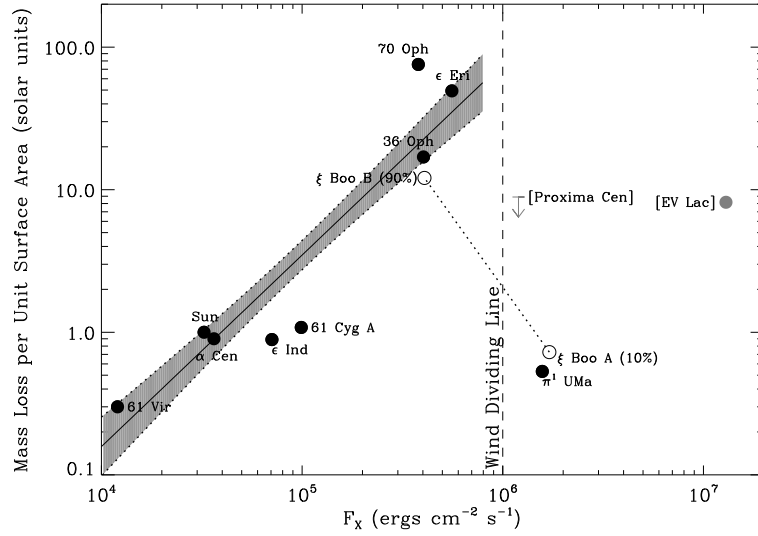
Fig. 3.12. A plot of mass loss rate (per unit surface area) versus X-ray surface flux density for all main sequence stars with measured winds. Most of these have spectral types of G (like the Sun) or (cooler) K, but the two with square-bracketed labels are (much cooler) tiny M dwarf stars. Separate points are plotted for the two members of the $\xi$ Boo binary, assuming $\xi$ Boo B accounts for 90% of the binary's wind, and $\xi$ Boo A only accounts for 10%. A power law, $\dot{M} \propto F_X^{1.34\pm0.18}$, is fitted to the less active stars where a wind/corona relation seems to exist, but this relation seems to fail for stars to the right of the "Wind Dividing Line" in the figure. From Wood *et al.*, 2014)
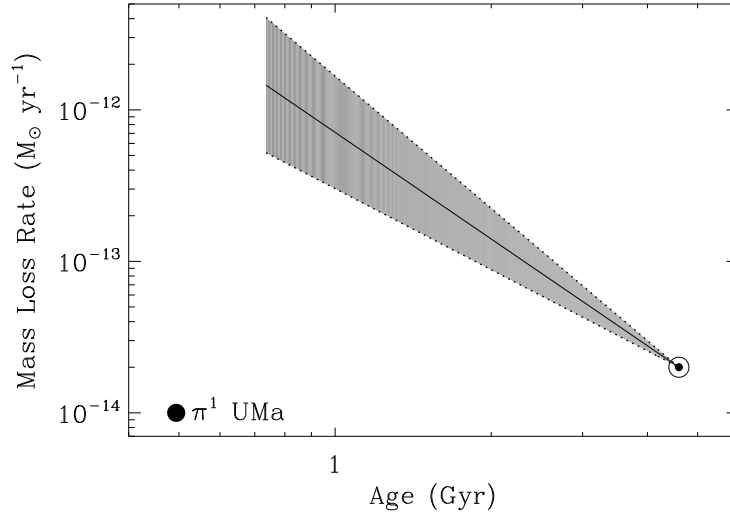
Fig. 3.13. The mass loss history of the Sun inferred from the power law relation in Fig. 3.12. The truncation of the relation in Fig. 3.12 means that the mass-loss/age relation is truncated as well. The low mass loss measurement for $\pi^1$ UMa suggests that the wind weakens at $t \approx 0.7$ Gyr as one goes back in time. (From Wood *et al.*, 2005)

# 4

# Effects of stellar eruptions throughout astrospheres

*Ofer Cohen*
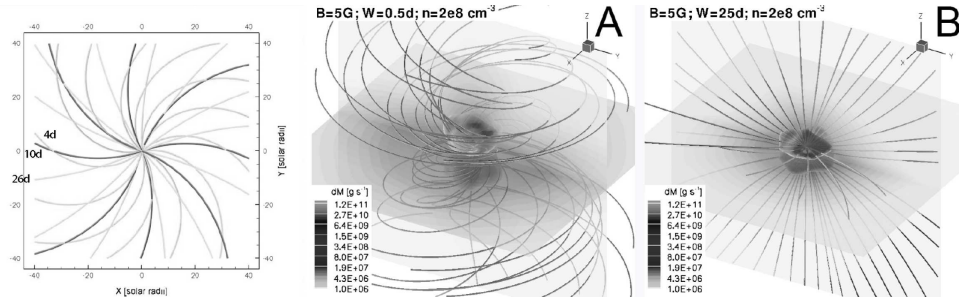
Fig. 4.1. *Left:* Conceptual display of different stellar-wind magnetic field spirals for a Sun with a 4.6 day rotation period, a 10 day period, and a 26 day period, as a function of distance in solar radii (From Cohen *et al.*, 2012). *Center/right:* Results from numerical simulations for the stellar coronae of solar analogs with rotation period of 0.5 day (middle) and 25 days (right). The astrospheric field lines are shown in grey. Also shown is the surface at which the Alfvénic Mach number equals unity. In the original figure (Cohen and Drake, 2014) the meridional and equatorial plains are colored with contours of the mass-loss rate, but these are not adequately reproduced in this gray-scale rendering.
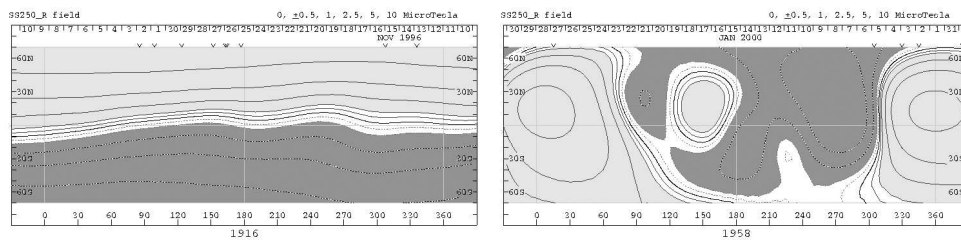
Fig. 4.2. The distribution of the solar magnetic field at $r = 2.5R_{\odot}$ ($B_0$) for solar minimum period (left, November 1996), and solar maximum period (right, January 2000) obtained by the Wilcox Solar Observatory (WSO, wso.stanford.edu).
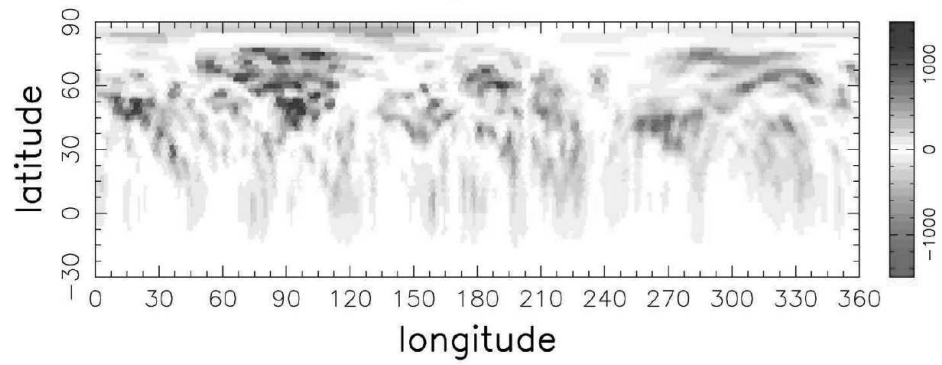
Fig. 4.3. Longitude-latitude map of the photospheric radial magnetic field of AB Doradus. Note that field in the deep southern hemisphere cannot be observed owing to the tilt of the spin axis. (From Hussain *et al.*, 2007)
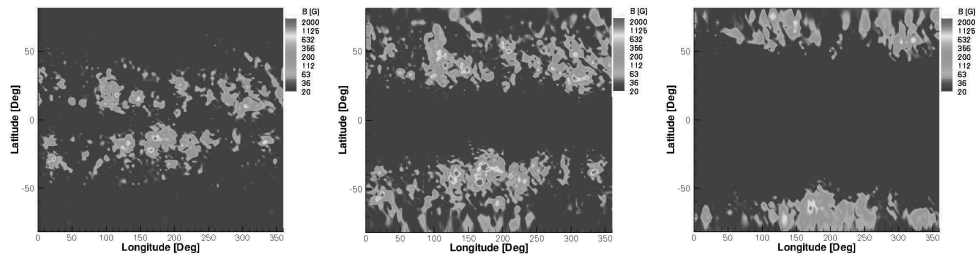
Fig. 4.4. A map of the solar photospheric radial magnetic field (magnetogram) during Carrington Rotation 1958 (January 2000, solar maximum period) shown on the left. The middle and right panels show manipulation of the original map, where the active regions have been shifted by 30 and 60 degrees towards the pole, respectively. (From Cohen *et al.*, 2012)
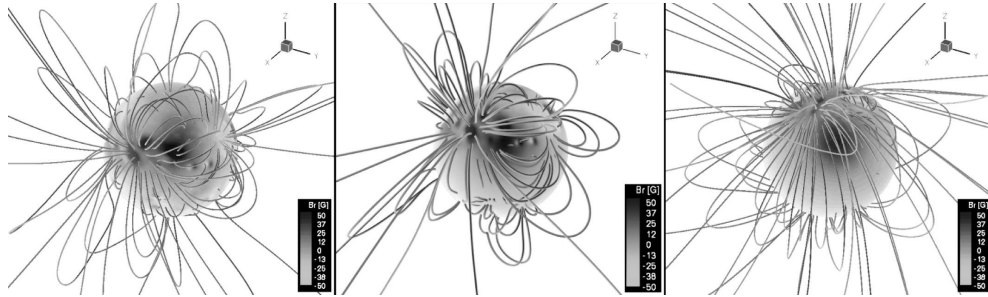
Fig. 4.5. The three-dimensional magnetic field corresponding to the surface distribution of the photospheric radial magnetic field (shown on a sphere of $r = R_\odot$) during solar maximum (left), and for manipulated photospheric filed with the active regions shifted by 30 (middle) and 60 (right) degrees towards the poles, as shown in the figure above. (From Cohen *et al.*, 2012)
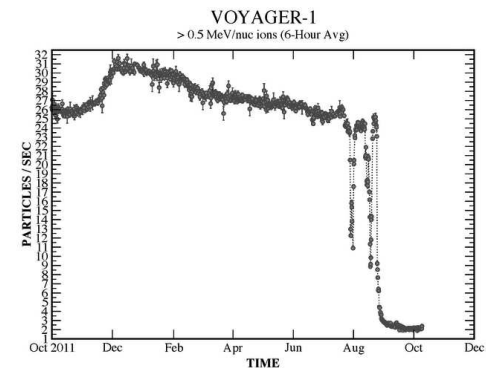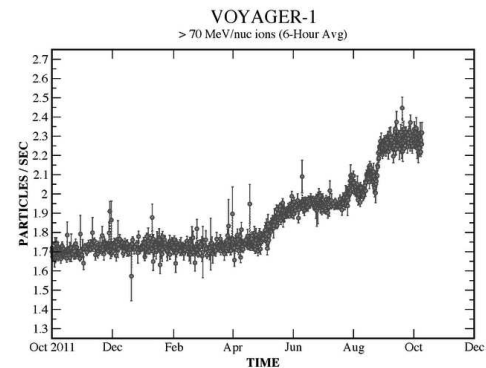
Fig. 4.6. The dramatic increase in cosmic-ray flux (top) and decrease in solar wind particle flux (bottom) observed by Voyager 1 around September 2012. This observation strongly suggests that Voyager 1 reached the ISM at the time of the change. (Figures from science.nasa.gov)
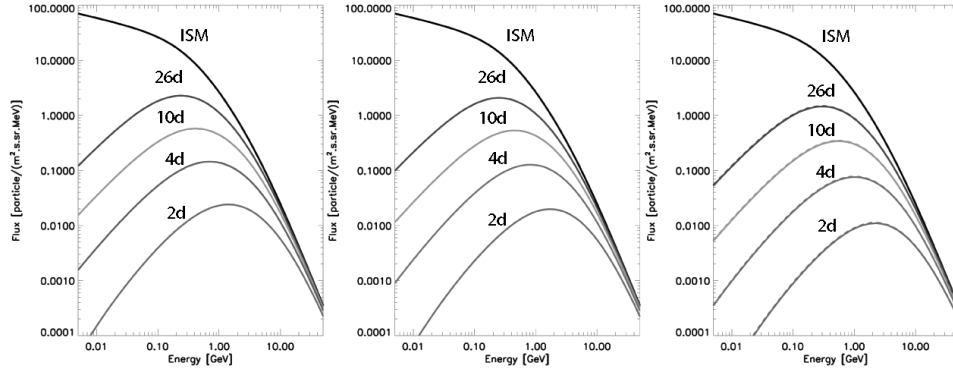
Fig. 4.7. Cosmic-ray energy spectrum for modeled solar rotation periods of 26d (current rotation), 10d, 4.6d, and 2d, along with the local ISM spectrum. Plots are for the current Sun (left), spots shifted towards the pole by 30 degrees (middle), and spots shifted towards the pole by 60 degrees (right). This plot is similar to Figure 11.11 in Vol. III, except that the x-axis unit is in GeV instead of MeV, and the flux is normalized by the additional steradian (sr) geometrical factor.
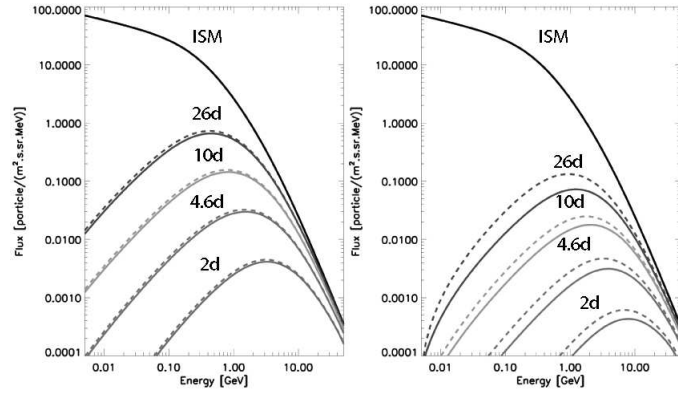
Fig. 4.8. Same as the right panel of Figure 4.7, but with the dipole component enhanced by a factor of 10 (left), and the spot component enhanced by a factor of 10 (right). Solid lines represent the spectrum with the Termination Shock (TS) scaled with the solar wind dynamic pressure, while dashed lines represent the spectrum for the TS fixed at 90 AU.
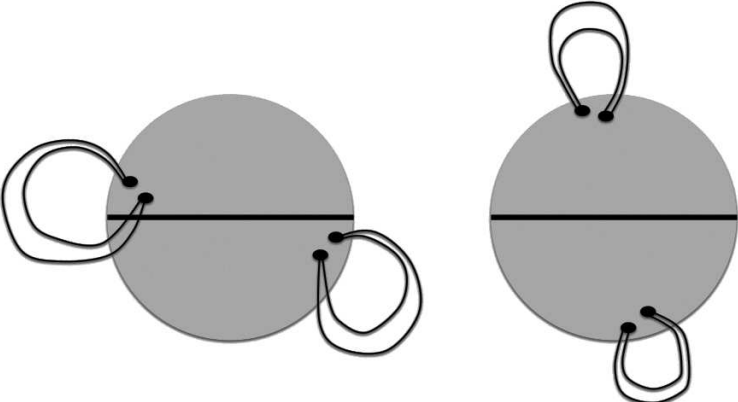
Fig. 4.9. On the Sun, CMEs are launched from active regions emerge at low latitudes near the equator (left). In active young stars, magnetic activity appears at high, polar latitudes. Therefore, CMEs may be launched mostly towards the polar astrospheric regions (right).
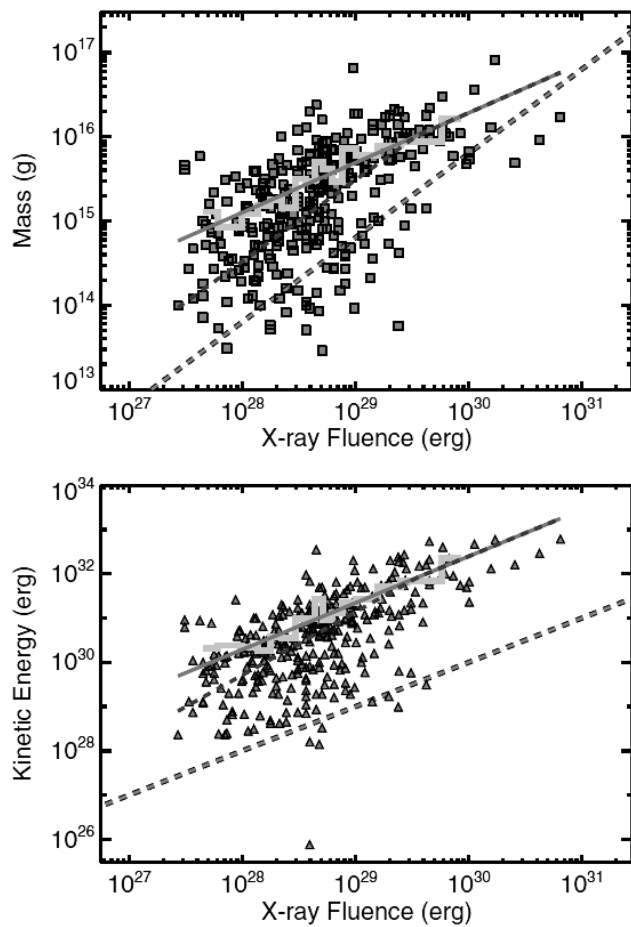
Fig. 4.10. Distribution of solar CME mass (top) and kinetic energy (bottom) as a function of flare energy. The light-grey histograms are the means over 20 data points and the solid lines are linear fits to these means. (From Drake *et al.*, 2013)
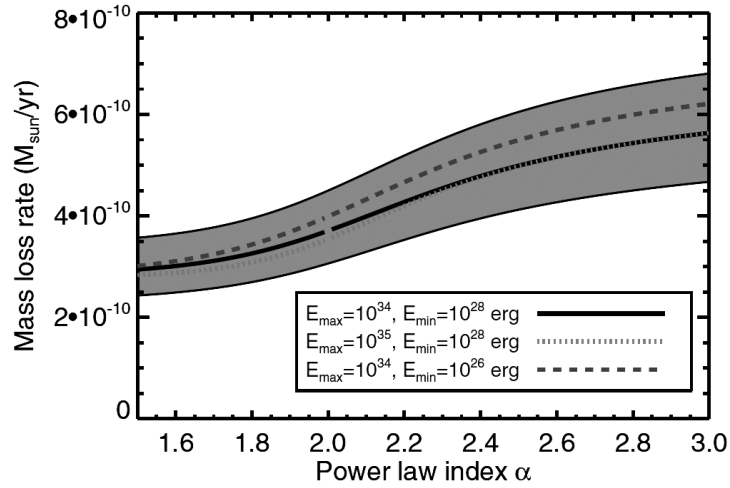
Fig. 4.11. The expected mass-loss rate due to CMEs as a function of the power index $\alpha$ for $L_x = 10^{30}$ ergs s$^{-1}$ and for different maximum and minimum event energies. The grey area represents the uncertainty in the other power-law indices. (From Drake *et al.*, 2013)
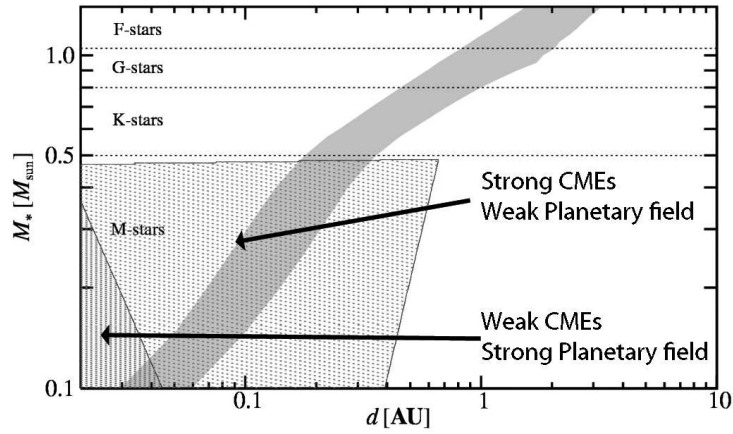
Fig. 4.12. Comparison between the habitable zone (HZ; shaded area) and the areas where strong magnetospheric compression is possible by CMEs (lightly and heavily dotted areas). The lightly dotted area indicates Earth-like exoplanets with a minimum value of the magnetic moment exposed to strong (dense) CMEs. This area denotes the region where CMEs compress the magnetosphere down to 1.15 Earth radii or less (*i.e.*, 1,000 km above the planetary surface). The heavily dotted area indicates Earth-like exoplanets with a maximum value of the magnetic moment exposed to weak (sparse) CMEs. In this region, CMEs compress the magnetosphere to less than 2 Earth radii. (From Khodachenko *et al.*, 2007)
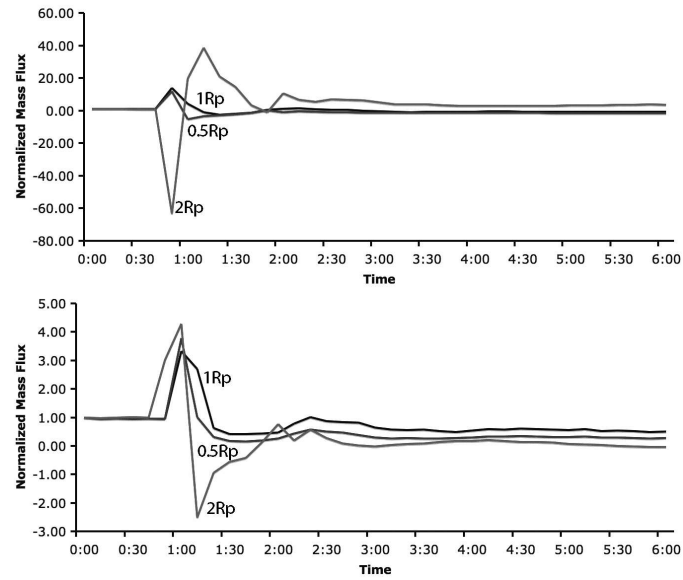
Fig. 4.13. Mass flux for a CME simulation integrated over three spheres around the impacted planet at heights of 0.5, 1, and 2 planetary radii above the surface, shown as a function of time. Fluxes are normalized to the value of the initial state at t=0 (which is positive). The top panel shows results for planetary field strength of 0.5 G, and the bottom panel shows results for planetary field strength of 1 G. (From Cohen *et al.*, 2011)
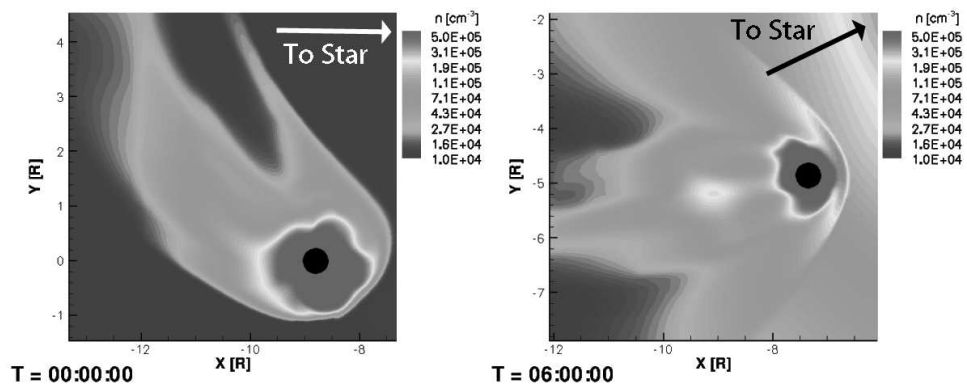
Fig. 4.14. Renderings of the number density around a close-in exoplanet shown on the equatorial plane for the initial, pre-eruption state (left), and during the CME event, 6 hours after the eruption. The plot is in the Astrocentric coordinate system at which the star is located at the origin of the coordinate system. (From Cohen *et al.*, 2011)
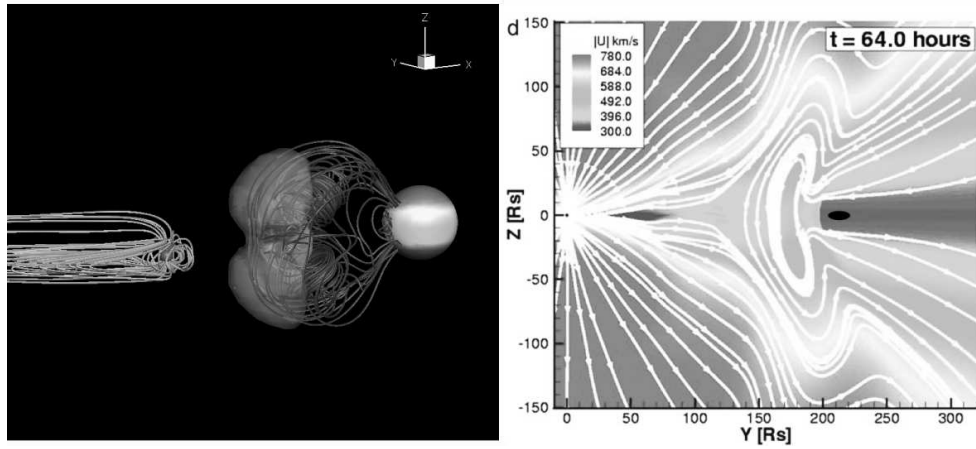
Fig. 4.15. *Left:* a CME approaching a planet. The star is shown on the right with selected CME field lines. The shaded volume represents an iso-surface for speed of 1500 $km\ s^{-1}$. The planet is shown as a small sphere with magnetospheric field lines shown as well. *Right:* meridional cut shows contours of speed between the Sun and the Earth with a small black ellipse representing the Earth's magnetosphere. (From Cohen *et al.*, 2011)
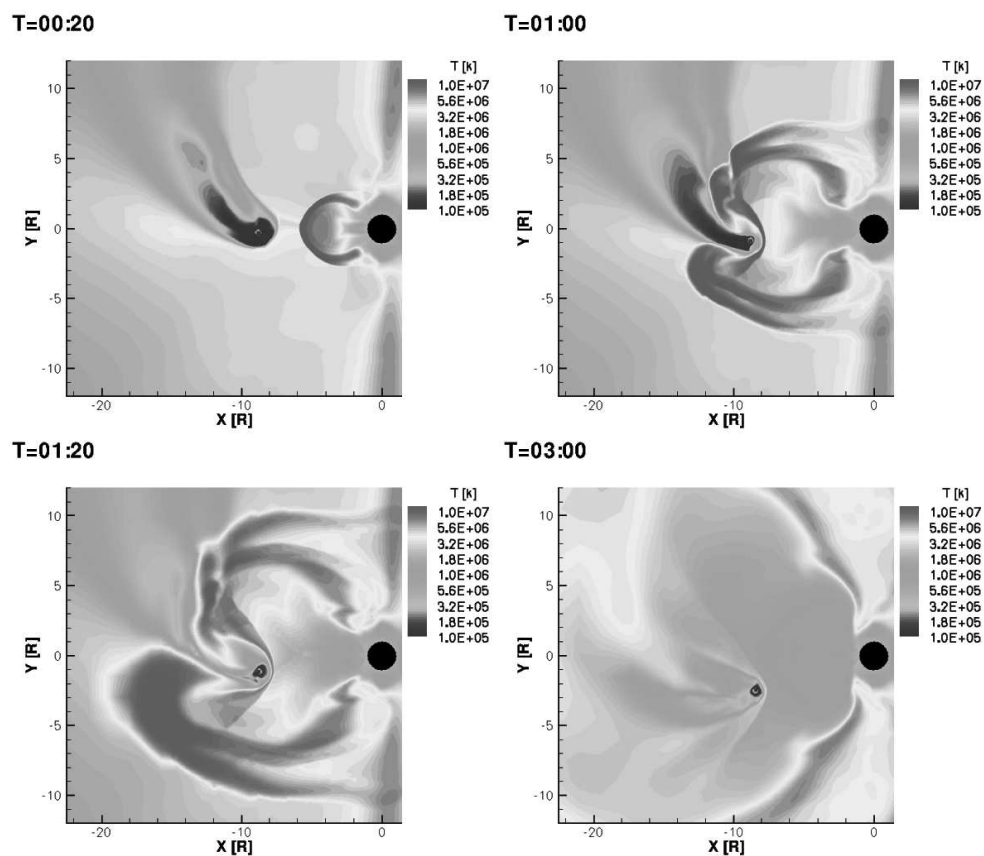
Fig. 4.16. Contours of the temperature displayed on the equatorial plane during a CME event at a close-in planet for four phases of the interaction. Coordinates are shown in units of stellar radius. (From Cohen *et al.*, 2011)

# 5

# Characteristics of planetary systems

*Debra Fischer and Ji Wang*
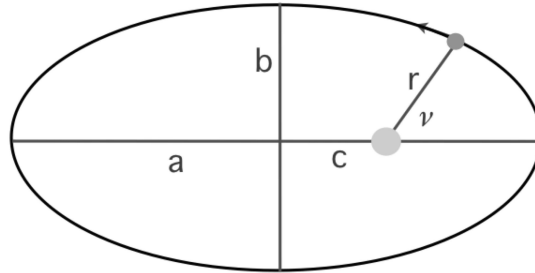
Fig. 5.1. Geometry of an elliptical orbit with semi-major axis $a$, semi-minor axis $b$, and eccentricity $e = c/a$.
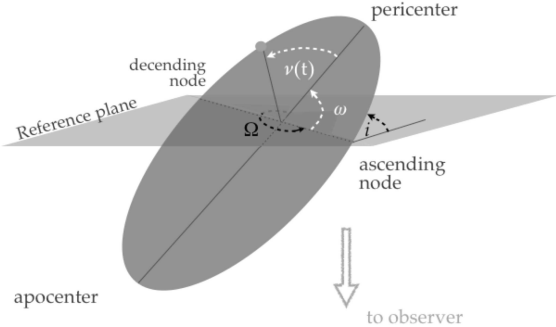
Fig. 5.2. Orbital angles $i$, $\omega$, and $\Omega$ define the orientation of the orbit with respect to the plane of the sky.
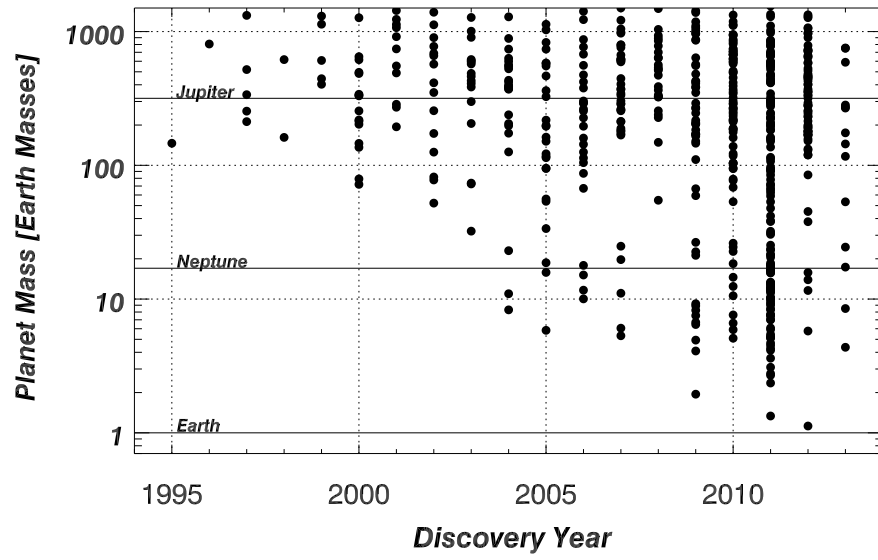
Fig. 5.3. Detection of exoplanets over time. Black dots indicate Doppler detections. Solid horizontal lines indicate the masses of Jupiter, Neptune and Earth.
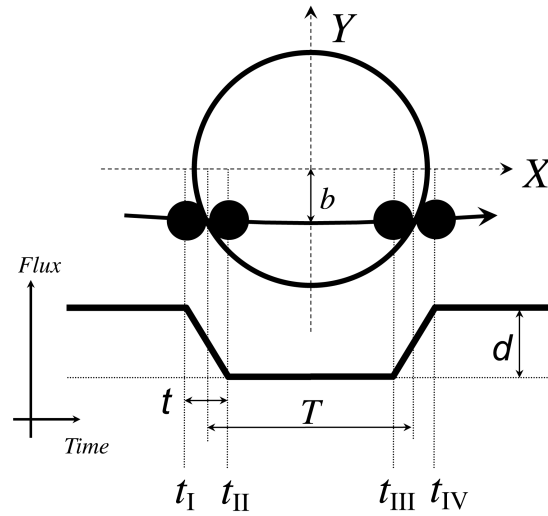
Fig. 5.4. The sketch of a transit light curve shows that the measured flux from the star begins to decrease during ingress. The flux is at a minimum after the planet has completed ingress and before the planet begins egress. After egress, the measured flux returns to the pre-transit value. Reproduced with permission from Winn (2011).
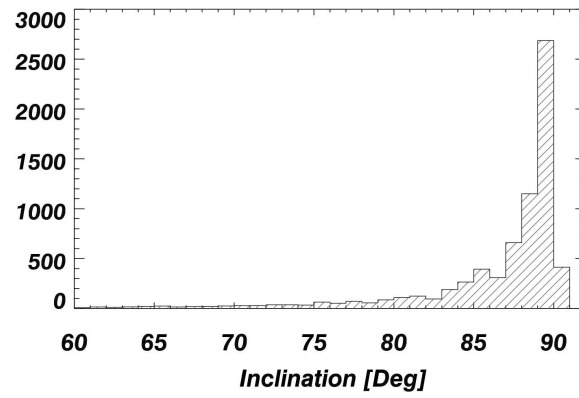
Fig. 5.5. The distribution of inclinations for the *Kepler* transiting planet candidates are highly biased toward edge-on ($i = 90°$) configurations (drawn from the list of KOIs in the NASA Exoplanet Archive).
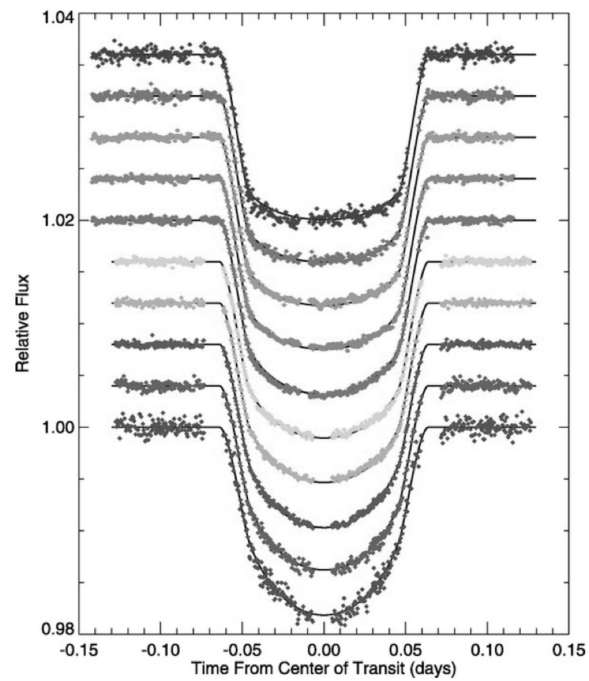
Fig. 5.6. Observations of HD 209458 in different HST bandpasses show the wavelength dependency of limb darkening (red wavelengths at top to blue at the bottom). From Knutson *et al.* (2007).
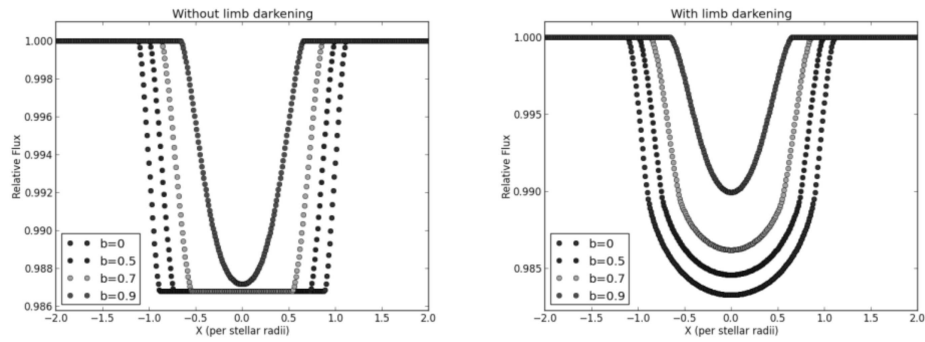
Fig. 5.7. (left) The shape of the transit light curve depends on the impact parameter $b$ (from 0 to 0.9 from the outside inward in the diagram). (right) Inclusion of limb darkening also affects the shape of the ingress and egress, making the curves more rounded. Figures courtesy of Meg Schwamb.
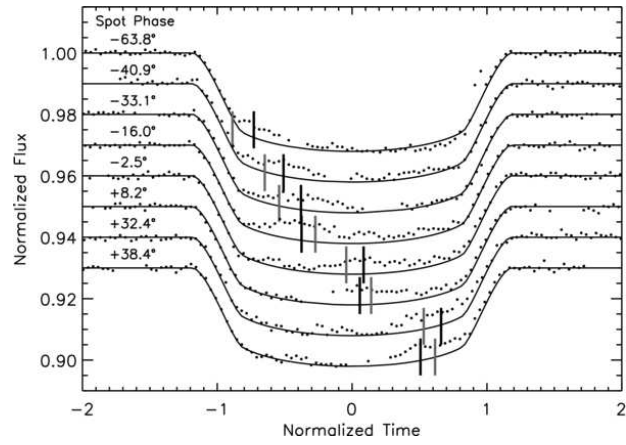
Fig. 5.8. As the planet in CoRot-2 transits starspots on HD 189733, which are cooler than the rest of the star, less flux is blocked. The rotation period of the planet is different from the rotation period of the spots, and the spots advance in this time series of transit light curves. These data were cleverly used to determine the alignment of the planet with the equatorial plane of the star (reproduced from Nutzman *et al.*, 2011).
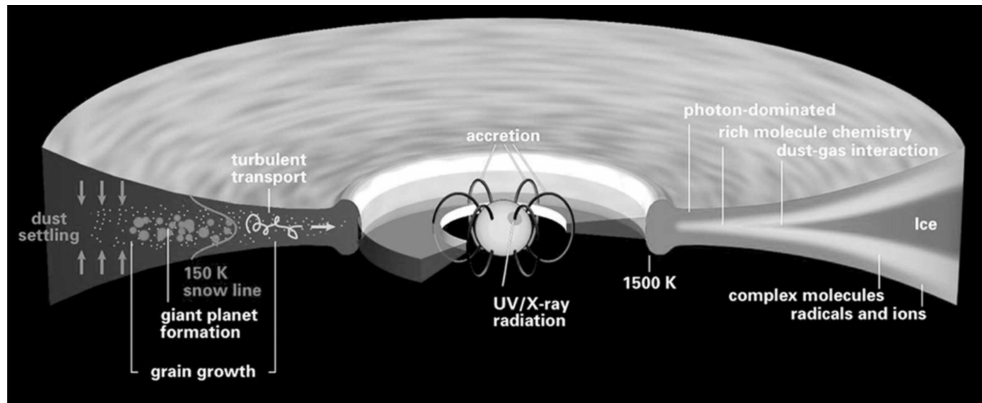
Fig. 5.9. A sketch of the structure and processes of protoplanetary disks. From a talk by Dmitry Semenov PPVI (Henning and Semenov 2014 Chem Reviews, submitted, https://www.youtube.com/watch?v=F2IDOeeNy8c).
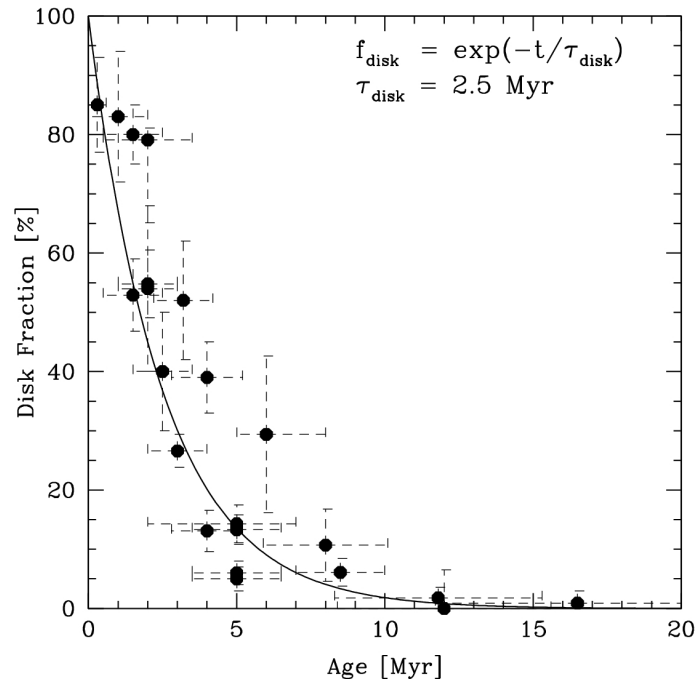
Fig. 5.10. Primordial disk fractions of stars in young clusters (Mamajek, 2009). These observations show that the dust disks only last for a few million years.
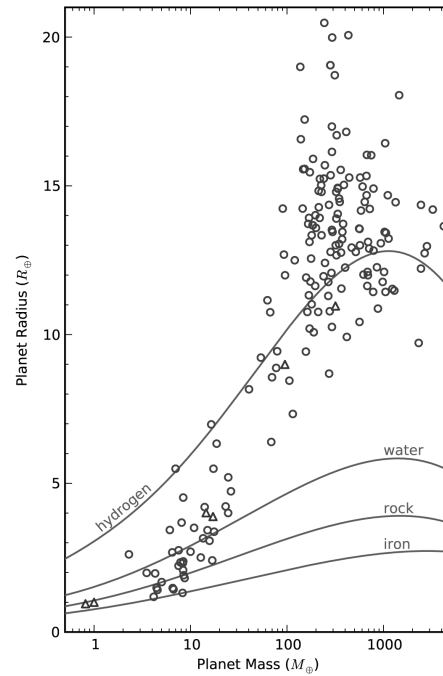
Fig. 5.11. Masses and radii of well-characterized exoplanets (circles) and solar system planets (triangles). Curves show models for idealized planets consisting of pure hydrogen (Seager *et al.*, 2007), water, rock ($Mg_2SiO_4$) or iron. From Howard *et al.* (2013).
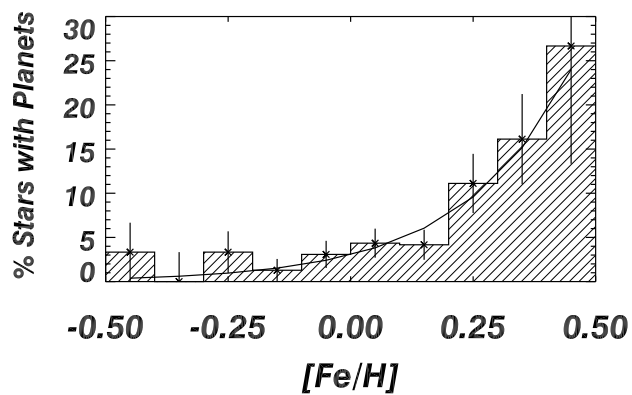
Fig. 5.12. High metallicity stars are more likely to host gas giant planets than sub-solar metallicity stars. Figure from Fischer and Valenti (2005).

# 6

# Planetary dynamos: updates and new frontiers

*Sabine Stanley*
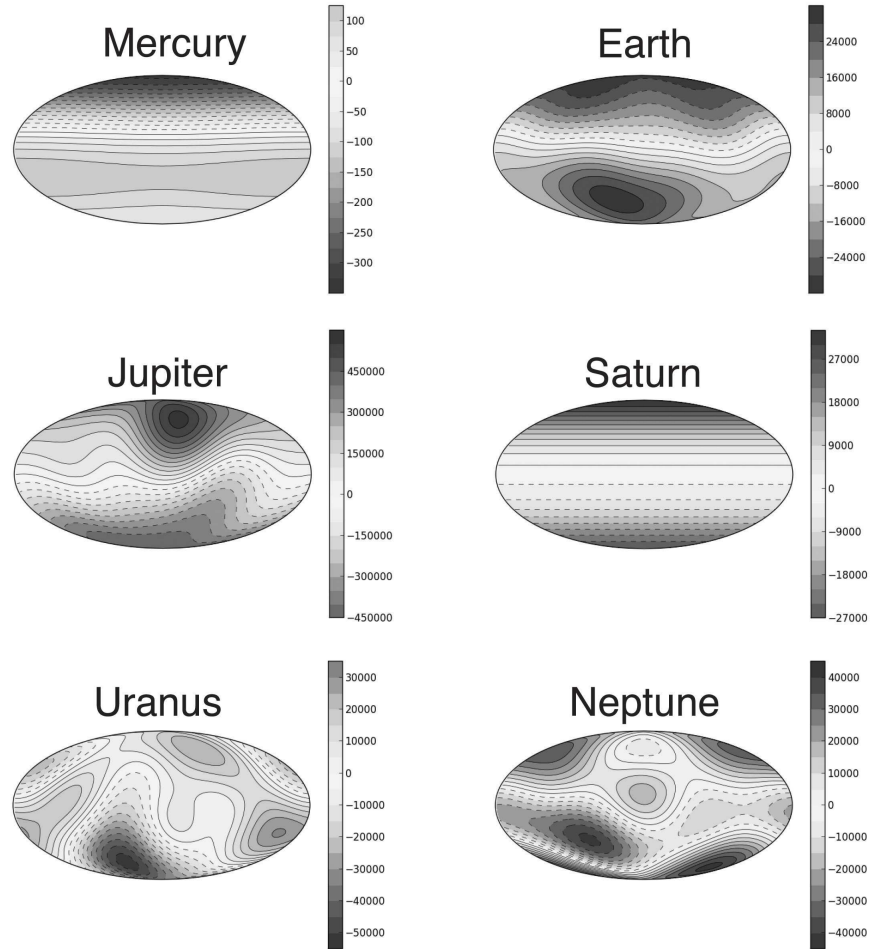
Fig. 6.1. Filled contours of the radial component of the surface magnetic field for planets in our solar system with active dynamos. Dashed contours represent negative values.
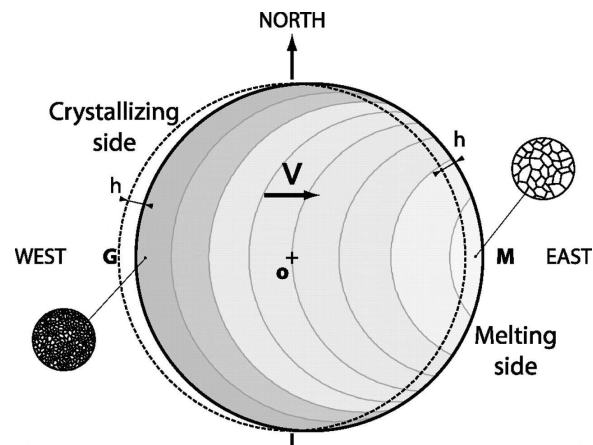
Fig. 6.2. Schematic of a translating inner planetary core due to inner core convection. The dashed circle is the equilibrium position of the inner core. Thermal perturbations from degree-one inner core convection cause the inner core to shift to the right inducing melting on the warm side and crystallization on the cold side. From Monnereau *et al.* (2010).
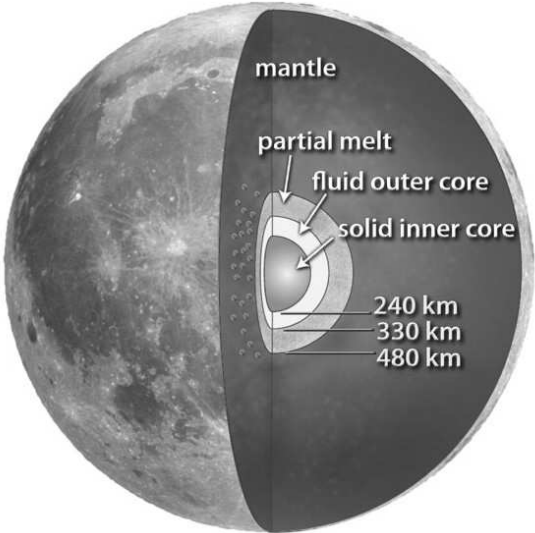
Fig. 6.3. Schematic of the lunar interior from lunar seismic data. From Weber *et al.* (2011).
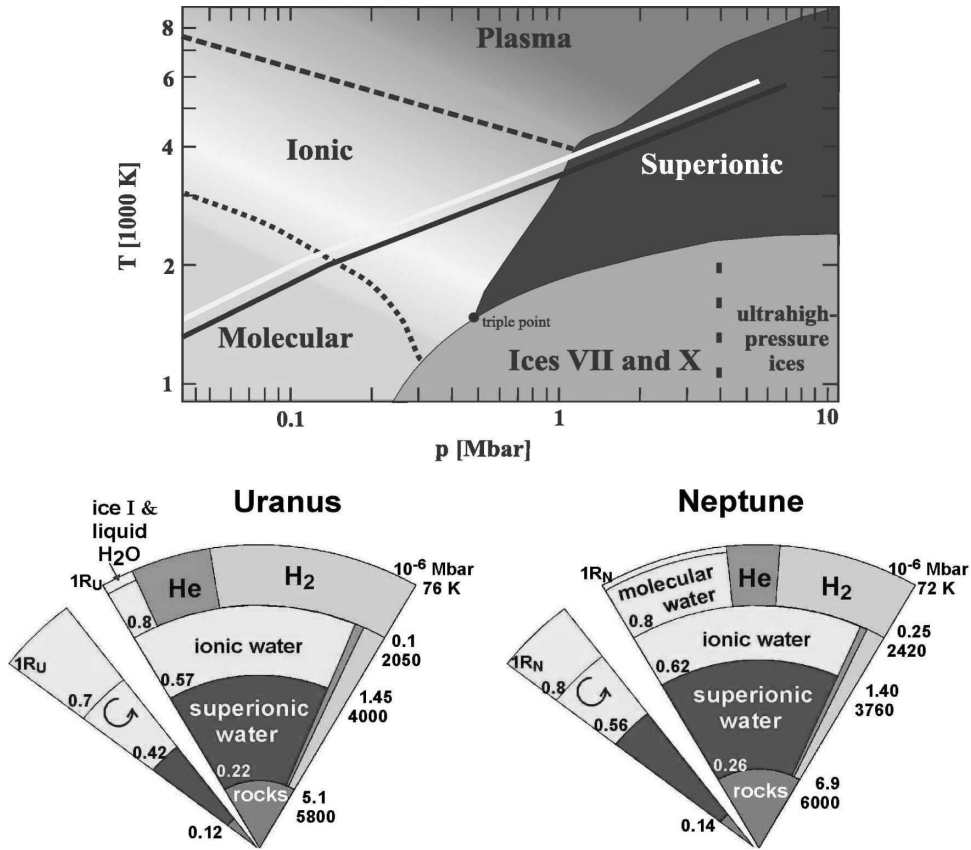
Fig. 6.4. Top: Phase diagram of water for temperatures and pressures relevant to the ice giant planet interiors. Isentropes for Uranus (white) and Neptune (black) are also shown. Bottom: Three-layer interior composition models for Uranus and Neptune that reproduce the gravity field data. The thin slice on the left of each figure is the structure of the dynamo source region used in Stanley and Bloxham (2006) for dynamo models. Figures from Redmer *et al.* (2011).
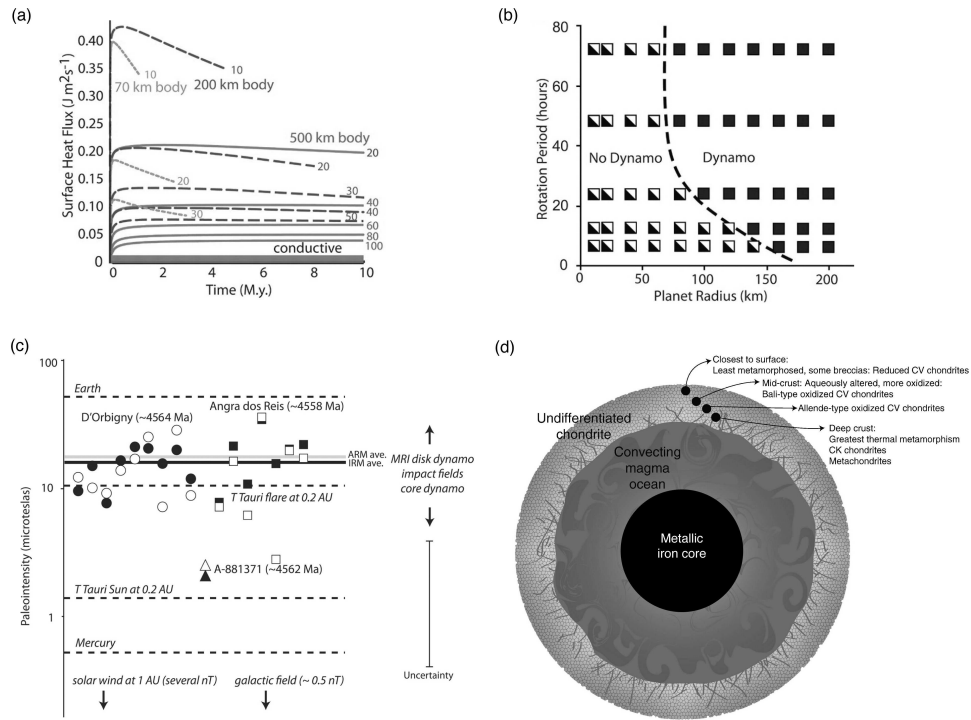
Fig. 6.5. Planetesimal dynamos: (a) Estimates of lifetimes of convection from thermal modelling. (b) Regions of phase space where dynamos have supercritical Magnetic Reynolds Numbers. (c) Paleointensity measurements for various Angrite meteorites as well as thresholds for magnetizing field strengths from different sources. (d) Interior structure of a chondrite parent body. Panels (a), (b) and (c) from Weiss *et al.* (2008). Panel (d) from Elkins-Tanton *et al.* (2011).
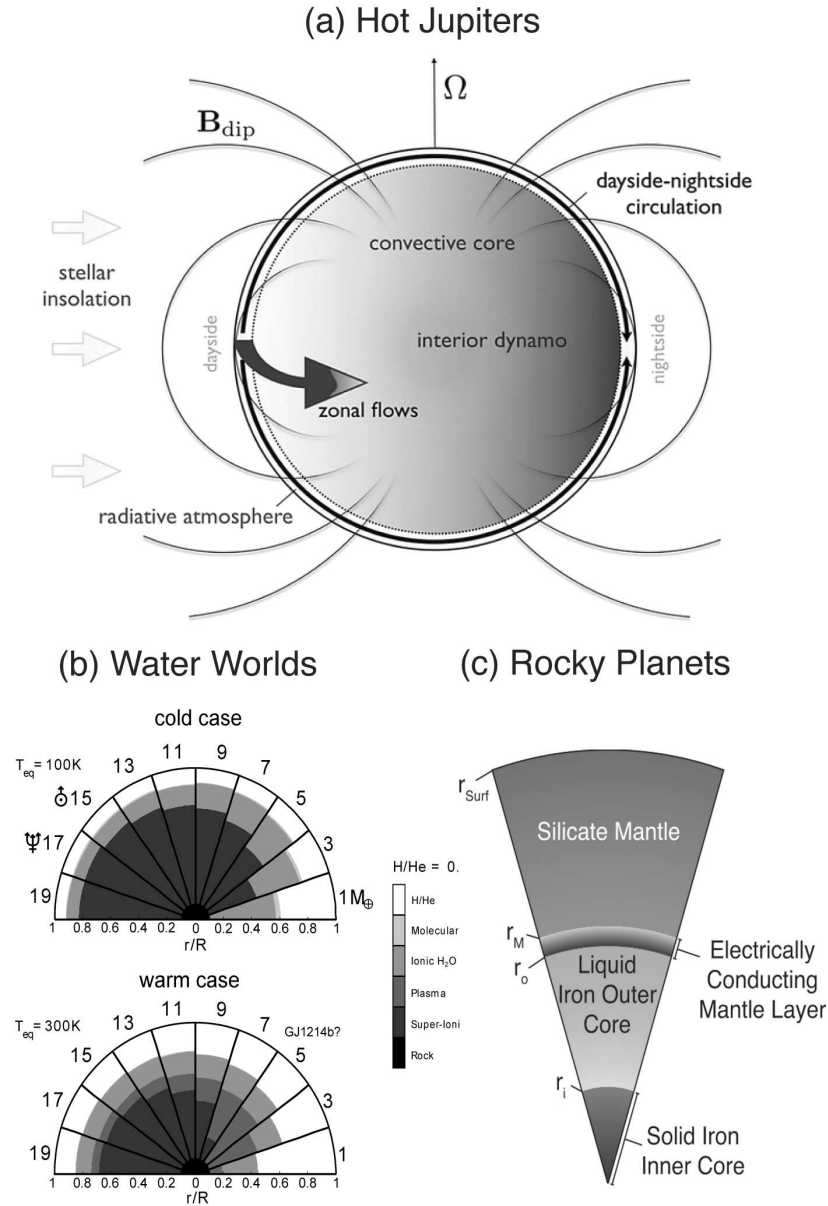
Fig. 6.6. Interior structure diagrams for various categories of exoplanets. (a) Schematic of a Hot Jupiter indicating dayside - nightside atmospheric flows which can interact with a dynamo-generated magnetic field (Batygin *et al.*, 2013), (b) Potential interior structures for water-rich planets of varying mass and equilibrium temperature (Tian and Stanley, 2013). Possible interior structures corresponding to Uranus (♂), Neptune (♀) and GJ1214b are marked. (c) Interior structure schematic for a rocky exoplanet with an electrically conducting mantle layer (Vilim *et al.*, 2013).

# 7

# Climates of terrestrial planets

*David Brain*
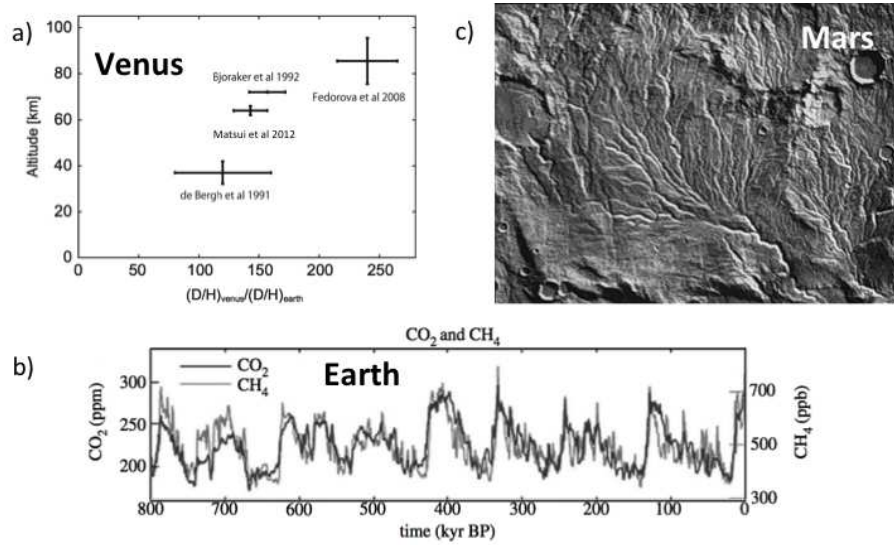
Fig. 7.1. Evidence for climate change on the terrestrial planets. a) Determinations of D/H in the Venus atmosphere relative to terrestrial atmospheric D/H (Matsui *et al.*, 2012); b) Earth's atmospheric carbon dioxide and methane concentrations as a function of time, as determined from ice cores (Hansen *et al.*, 2013); c) A dendritic river valley network in the Warrego Valles region of Mars (courtesy NASA Viking).
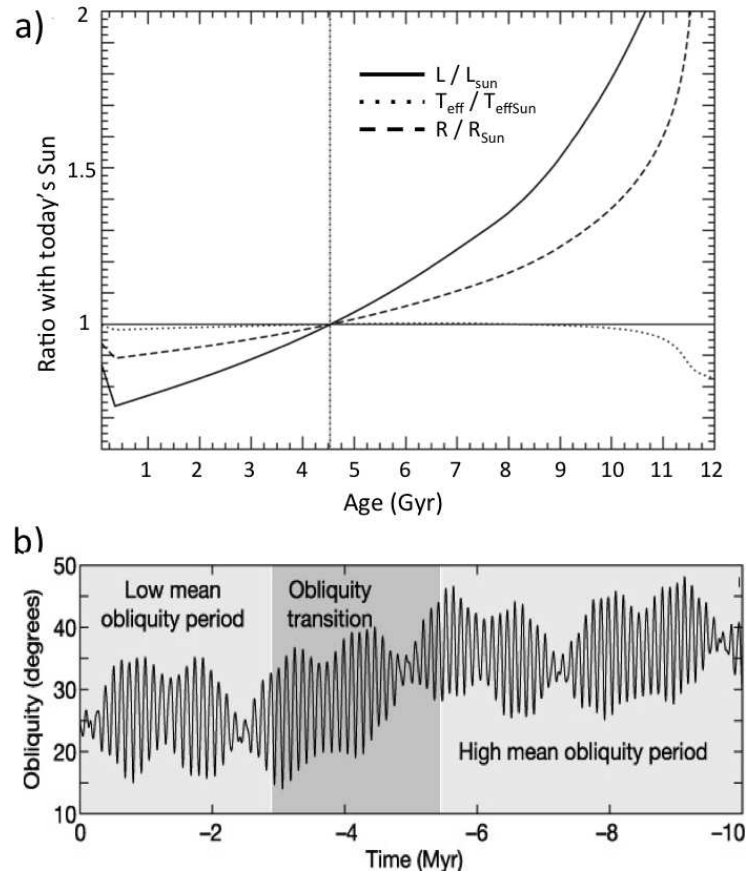
Fig. 7.2. Variation in climate drivers at terrestrial planets. a) Modeled solar properties (luminosity, effective temperature, radius) as a function of time, relative to today's Sun (Ribas *et al.*, 2005); b) Martian obliquity (*i.e.*, tilt) as a function of time. (From Levrard *et al.*, 2004)
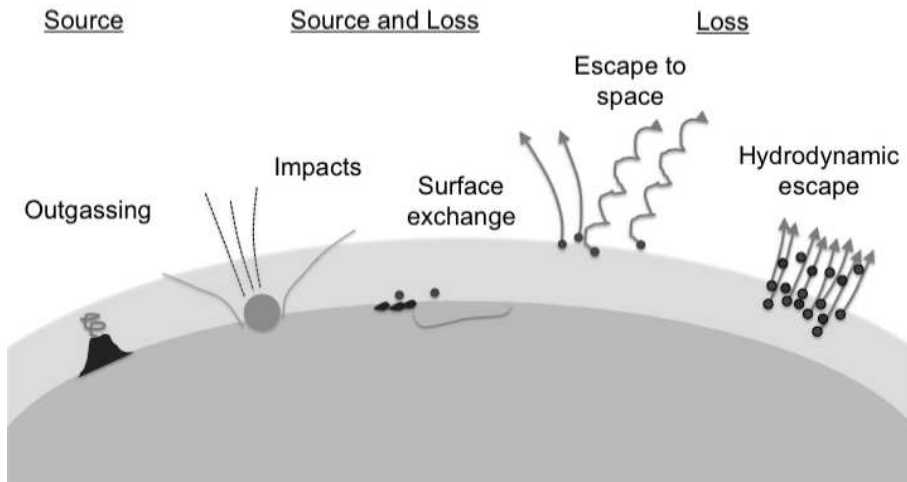
Fig. 7.3. Source and loss mechanisms for planetary atmospheres.
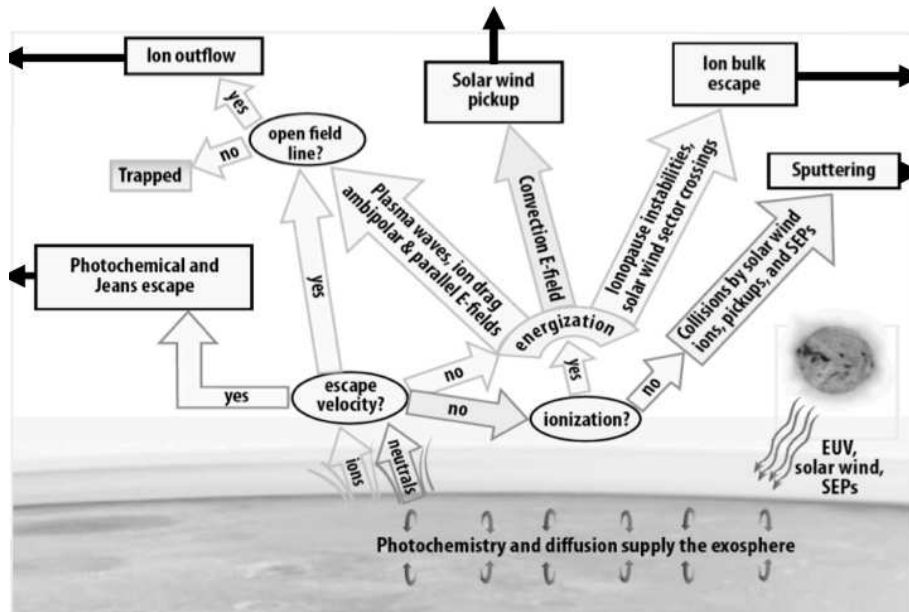
Fig. 7.4. Flowchart showing pathways to energization and escape of particles from a planetary atmosphere. Though Mars is depicted in the diagram, the six processes shown in the rectangular boxes are generic, and can apply to any planet (courtesy NASA MAVEN).
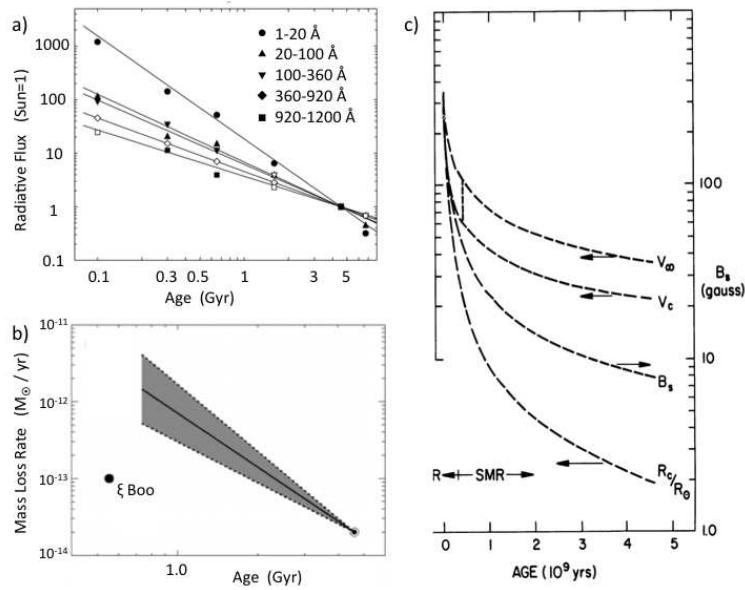
Fig. 7.5. Evolution of solar drivers of atmospheric escape. a) solar EUV photon flux, relative to today (from Ribas *et al.*, 2005); b) solar mass loss rate (*i.e.*, solar wind flux) (from Wood *et al.*, 2005); c) interplanetary magnetic field (curve labeled $B_S$; from Newkirk, 1980).
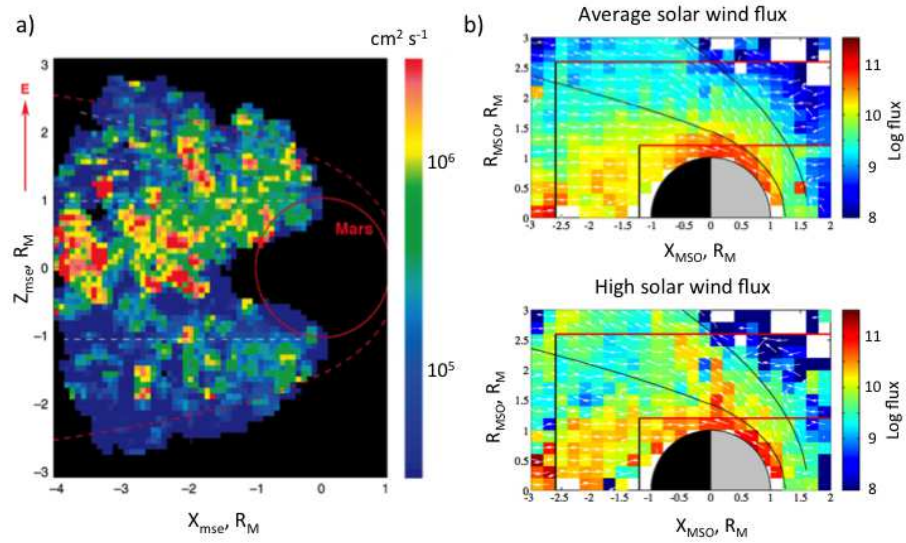
Fig. 7.6. Ion escape from the Martian atmosphere, organized by solar drivers. The Sun is to the right in both panels. a) escaping ion fluxes downstream from Mars are greater in the hemisphere of upward directed' (with respect to the planet) solar wind electric field (Barabash *et al.*, 2007); b) escaping ion fluxes downstream from Mars are greater during periods of high solar wind flux. (From Nilsson *et al.*, 2011)
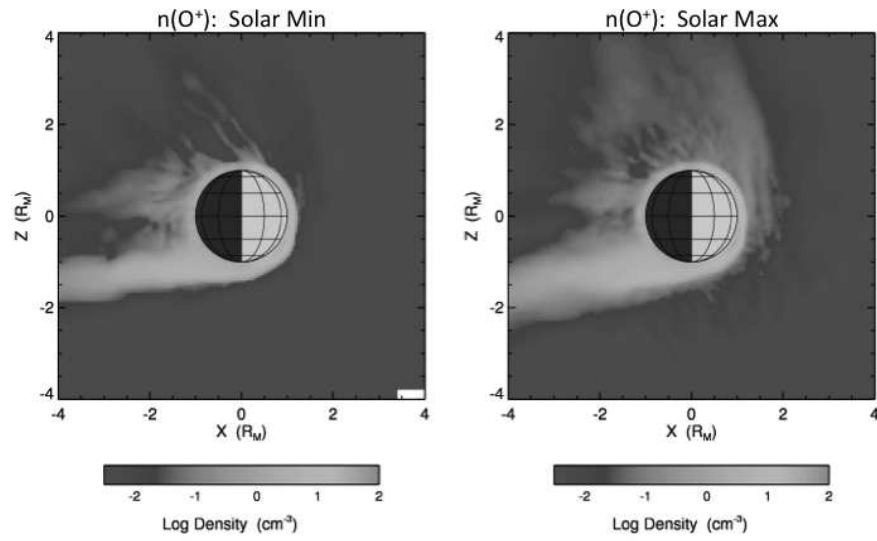
Fig. 7.7. Density of escaping atomic oxygen ions from Mars at solar minimum (left) and solar maximum (right) as predicted by a global hybrid plasma simulation. The Sun is at left in each panel, and the solar wind electric field points toward $+y$. Courtesy E. Kallio and R. Jarvinen.
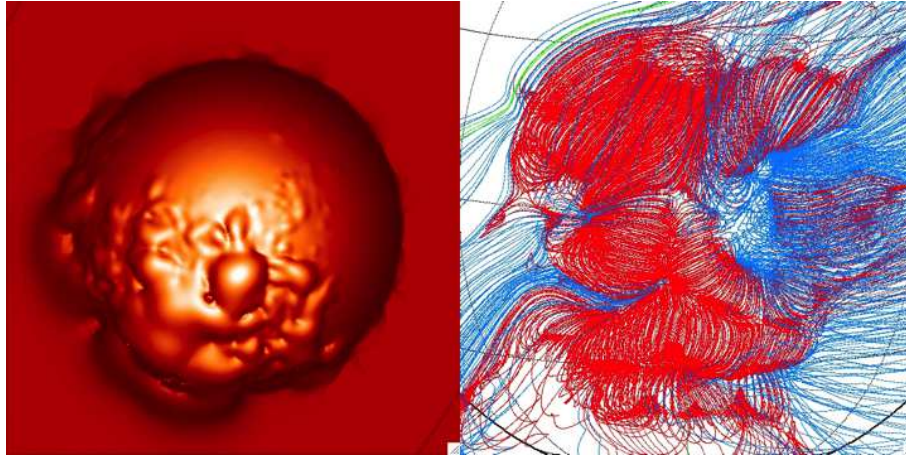
Fig. 7.8. Influence of magnetic fields on planetary near-space environments. Magnetic fields supply magnetic pressure (left: for Martian crustal magnetic fields) that deflect solar wind, but also modify magnetic topology (from Brain, 2006); (right: for the strong Martian crustal fields in the southern hemisphere, where red denotes closed field lines and blue denotes field lines open to the solar wind at one end) that enable exchange of particles and energy between the atmosphere and solar wind. Both renderings result from model calculations that include contributions from crustal fields and external drivers (solar wind or IMF).
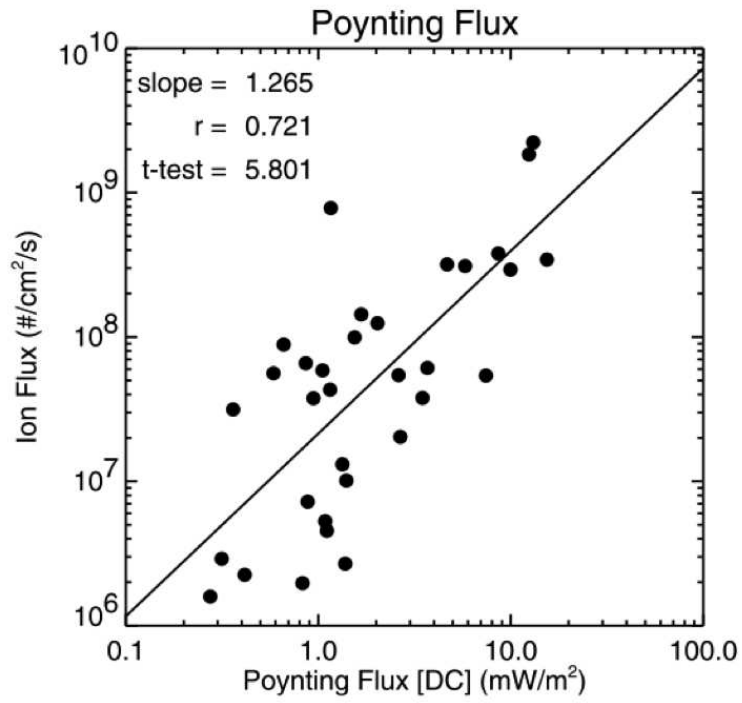
Fig. 7.9. Measurements of outflowing oxygen ions from Earth's cusp regions against solar wind Poynting flux. (From Strangeway *et al.*, 2005)

# 8

# Upper atmospheres of the giant planets

*Luke Moore, Tom Stallard, and Marina Galand*
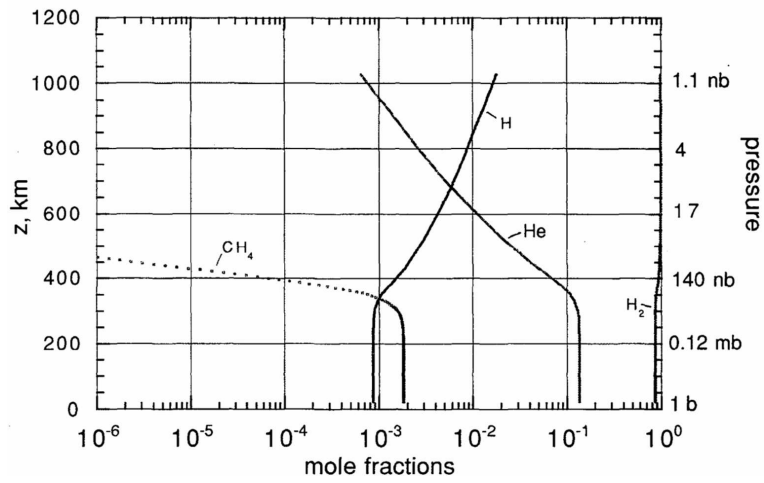
Fig. 8.1. Galileo Probe results showing Jupiter upper atmospheric mixing ratios. Altitudes refer to radial distance above the 1 bar pressure level. (From Seiff *et al.*, 1998)
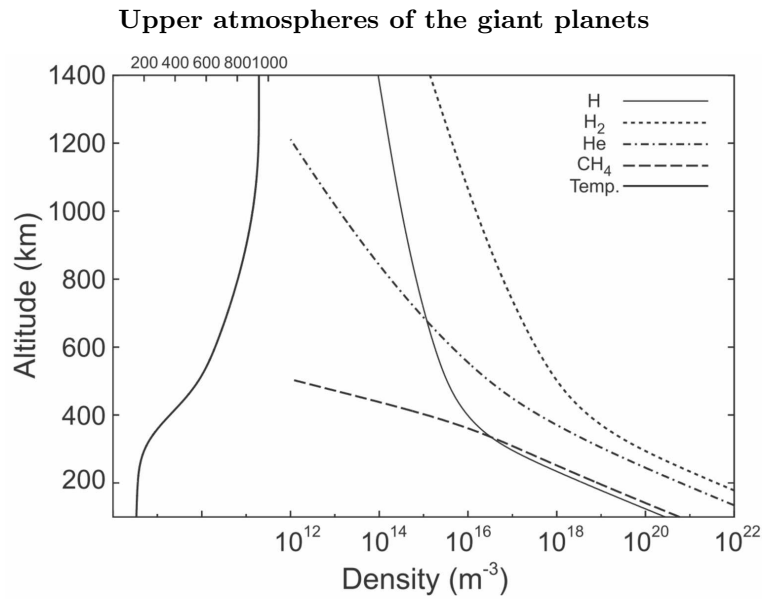
Fig. 8.2. Jupiter thermospheric parameters, based on Galileo Probe measurements. Altitudes refer to radial distance above the 1 bar pressure level. (From Barrow and Matcheva, 2011)
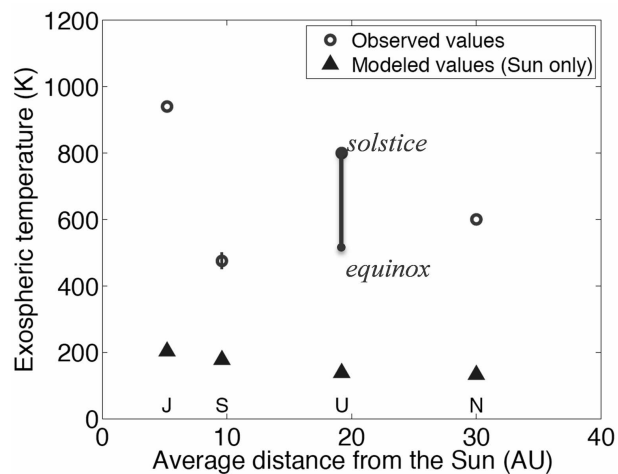
Fig. 8.3. Upper atmospheric temperature as a function of heliocentric distance for the giant planets, comparing observations with model values using only solar irradiance as energy input (after Yelle and Miller, 2004; Melin *et al.*, 2011a, 2013). Note that these values represent a combination of measurements from a range of latitudes with different seasonal and solar conditions. In addition, the Uranus values include both neutral exobase temperatures as well as $H_3^+$ temperatures near the ionospheric peak altitude.
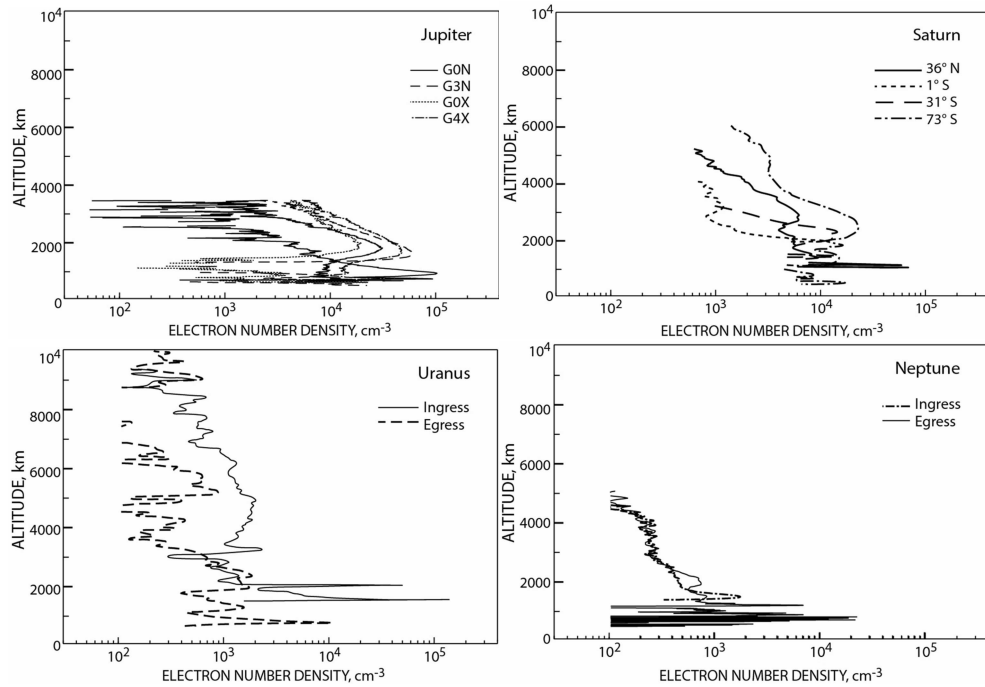
Fig. 8.4. Ionospheric electron density profiles derived from spacecraft radio occultation experiments at (top left) Jupiter, (top right) Saturn, (bottom left) Uranus, and (bottom right) Neptune. Altitudes refer to radial distance above the 1 bar pressure level. Profiles are from the Galileo spacecraft for Jupiter (Yelle and Miller, 2004), and from the Voyager spacecraft for Saturn (Lindal *et al.*, 1985), Uranus (Lindal *et al.*, 1987), and Neptune (Lindal, 1992).
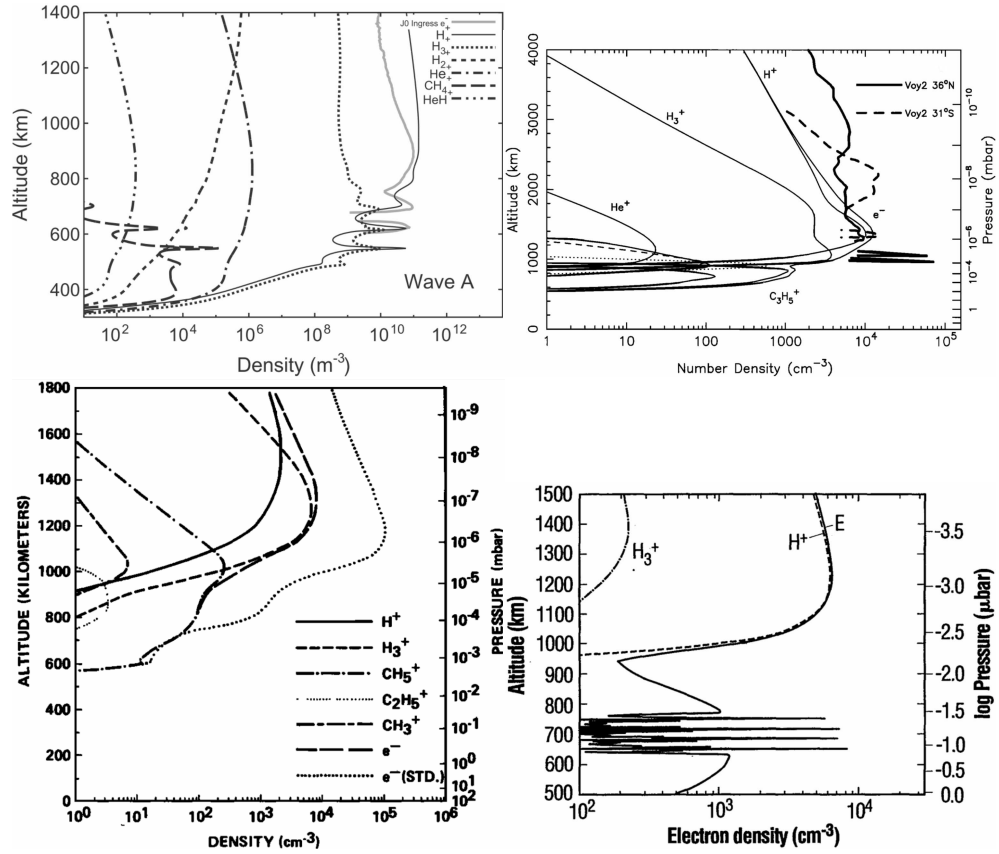
Fig. 8.5. Ionospheric model calculations for (top left) Jupiter, (top right) Saturn, (bottom left) Uranus, and (bottom right) Neptune. Altitudes refer to radial distance above the 1 bar pressure level. Note that electron density profiles are labeled as e- in the Jupiter, Saturn, and Uranus panels, and as E in the Neptune panel. (Sources: Jupiter: Barrow and Matcheva, 2011; Saturn: Moses and Bass, 2000; Uranus: Chandler and Waite Jr., 1986; Neptune: Lyons, 1995)
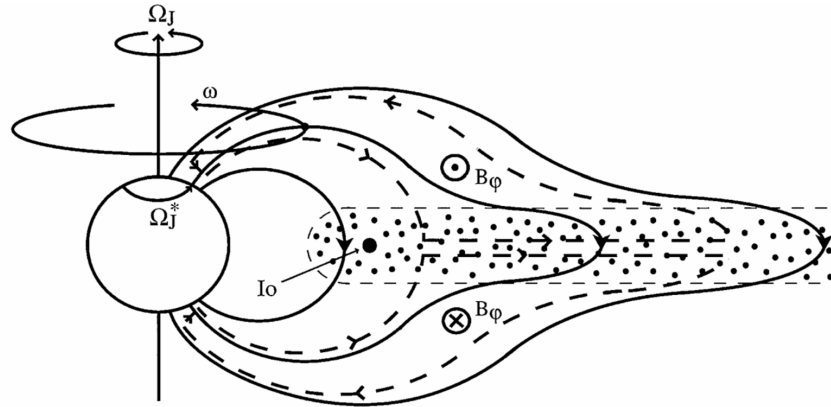
Fig. 8.6. Sketch of a meridian cross-section through the jovian magnetosphere, showing the principal features of the inner and middle magnetosphere regions. The arrowed solid lines indicate magnetic field lines, which are distended outwards in the middle magnetosphere region by azimuthal currents in the plasma sheet. The plasma sheet plasma originates mainly at Io, which orbits in the inner magnetosphere at 6 $R_{\rm J}$, liberating $\sim 10^3$ kg s$^{-1}$ of sulphur and oxygen plasma. This plasma is shown by the dotted region, which rotates rapidly with the planetary field due to magnetosphere-ionosphere coupling, while more slowly diffusing outwards. Three separate angular velocities associated with this coupling are indicated. These are the angular velocity of the planet $\Omega_{\rm J}$, the angular velocity of a particular shell of field lines $\omega$, and the angular velocity of the neutral upper atmosphere in the Pedersen layer of the ionosphere, $\Omega_L^*$. The latter is expected to lie between $\omega$ and $\Omega_{\rm J}$ because of the frictional torque on the atmosphere due to ion-neutral collisions. The oppositely directed frictional torque on the magnetospheric flux tubes is communicated by the current system indicated by the arrowed dashed lines, shown here for the case of sub-corotation of the plasma (*i.e.*, $\omega \leq \Omega_{\rm J}$). This current system bends the field lines out of meridian planes, associated with azimuthal field components $B_\phi$ as shown. (From Cowley and Bunce, 2001)
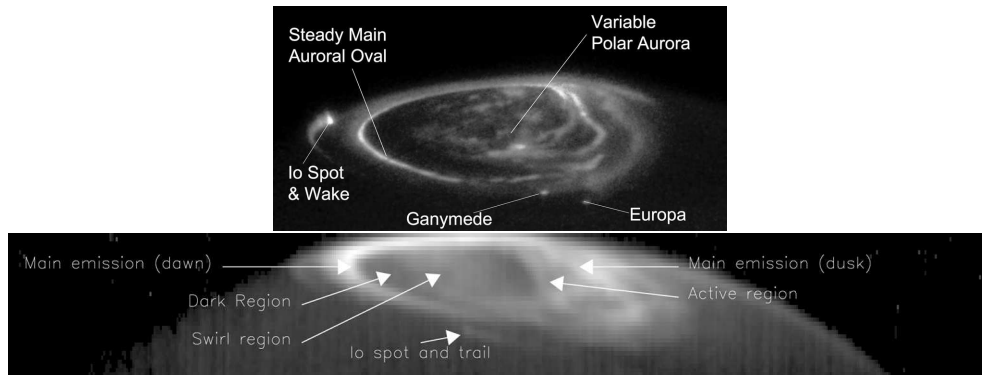
Fig. 8.7. UV (top) and IR (bottom) auroral images of Jupiter, with major features indicated. (From - top - Ch. 13 in Vol. I [Clarke, 2004] and - bottom - T. Stallard, personal communication, 2014)

# 9

# Aeronomy of terrestrial upper atmospheres

*David E. Siskind and Stephen W. Bougher*
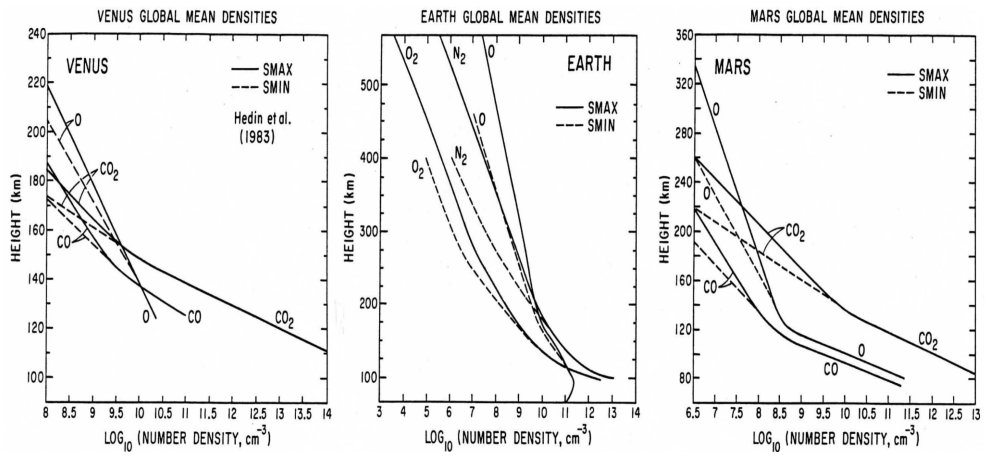
Fig. 9.1. Compositions of the upper atmospheres of Venus, Earth and Mars. (From Bougher and Roble, 1991)
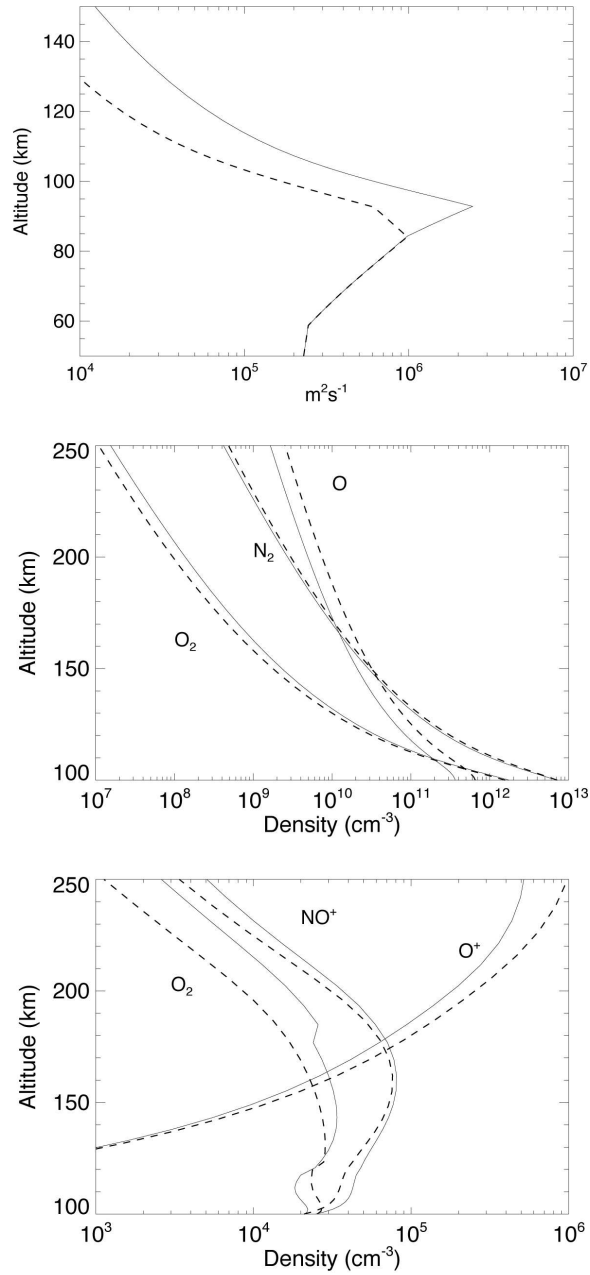
Fig. 9.2. Effect of varying $K_{zz}$ on neutral neutral thermospheric and ionospheric constituent profiles. The top panel shows the two $K_{zz}$ profiles. The center panel profiles shows the resultant neutral constituent profiles where the dashed curves are associated with the dashed $K_{zz}$ profile. The bottom panel shows the resultant ionospheric profiles where using the dashed $K_{zz}$ profiles leads to the largest value of $O^+$ at 250 km.
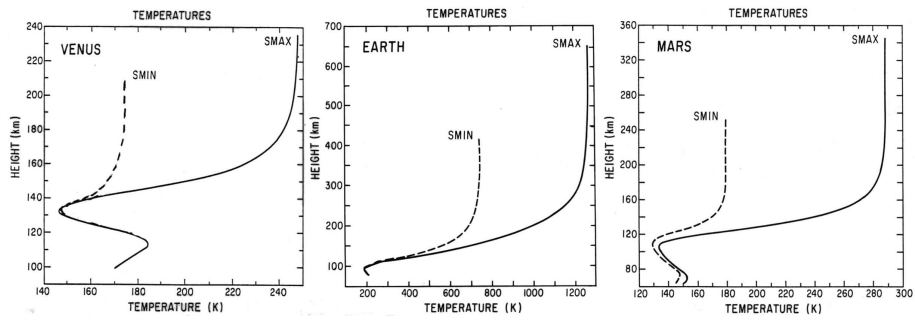
Fig. 9.3. Three planet global mean temperature profiles for solar minimum (SMIN) and maximum (SMAX) conditions. (From Bougher and Roble, 1991)
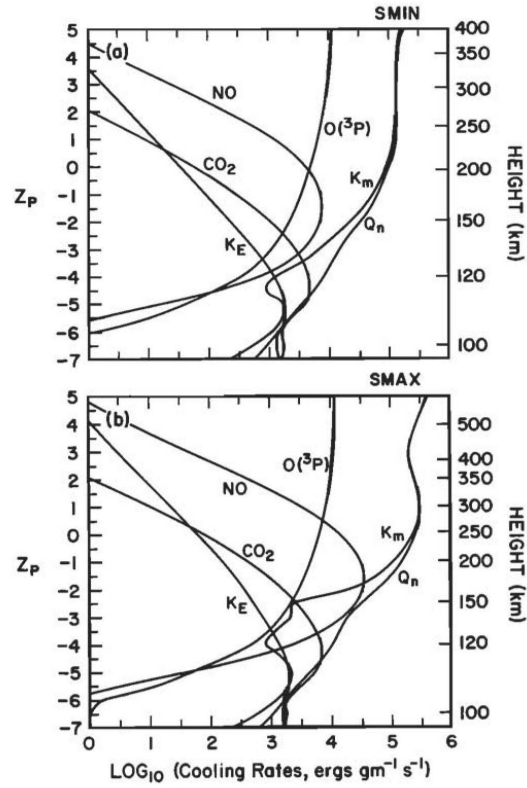
Fig. 9.4. Calculated $\log_{10}$ neutral gas heating and cooling rate profiles (ergs gm$^{-1}$ s$^{-1}$ for (a) solar minimum and (b) solar maximum conditions. $Q_n$ is the total neutral heating rate, $K_m$ is the cooling rate by downward molecular thermal conduction , $K_e$ is for eddy thermal conduction; NO is radiative cooling from the 5.3 $\mu$m emission from nitric oxide, $CO_2$ is radiative cooling from 15 $\mu$m emission from $CO_2$ and $O(^3P)$ is cooling from the fine structure of atomic oxygen. (From Roble *et al.*, 1987)
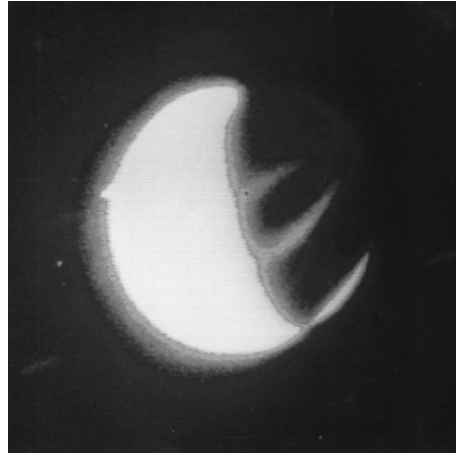
Fig. 9.5. FUV airglow of the Earth as observed with the Apollo 16 lunar camera. (From Carruthers and Page, 1976)

UT:2005/11/14 05:57:22—06:33:04
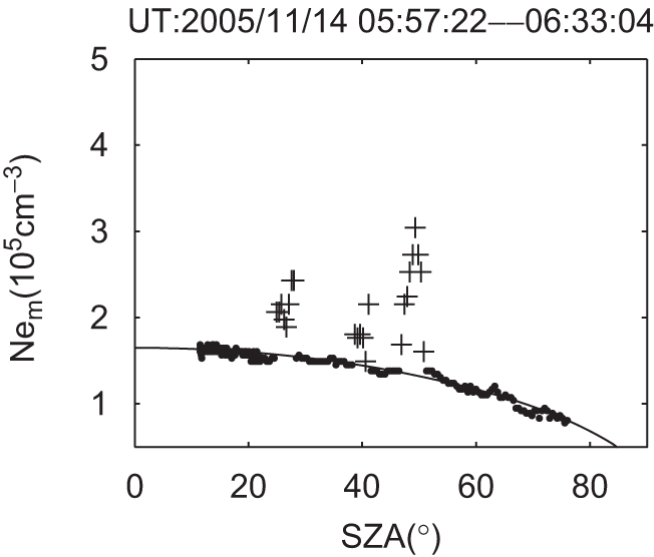


Fig. 9.6. Electron densities from the Mars Express as function of solar zenith angle (SZA). (From Nielsen *et al.*, 2007)
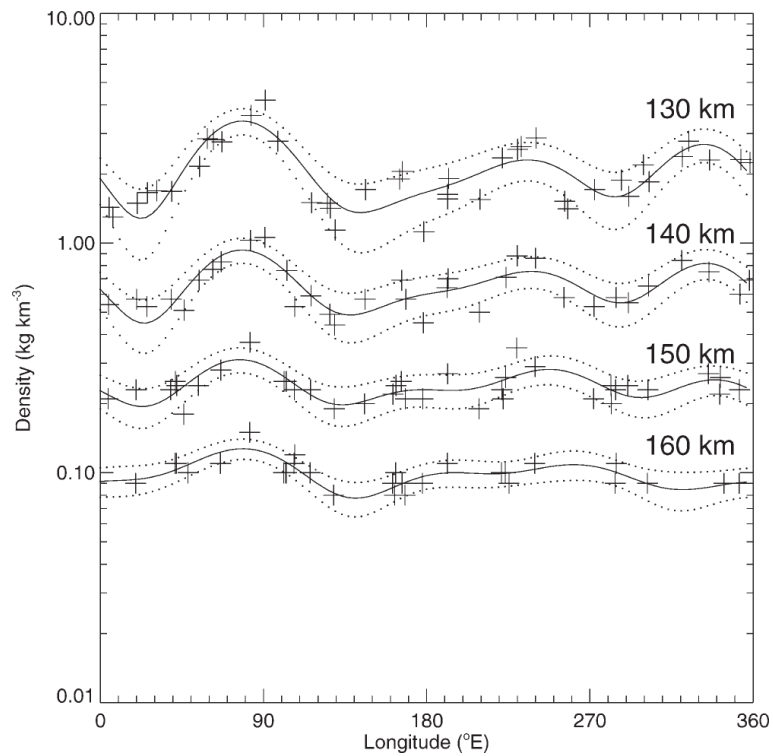
Fig. 9.7. Mass density measurements at 130, 140, 150 and 160 km altitude obtained between $10° - 20°$ N during MGS aerobraking. Model fits to data (waves 1-3) from each altitude are plotted as solid lines and $1-\sigma$ uncertainties about each fit as dotted lines. All data are taken from a local time of 15 hours. Measurements at each altitude were taken over about 1 week. All statistically significant peaks and troughs appear fixed in longitude. (From Withers *et al.*, 2003)
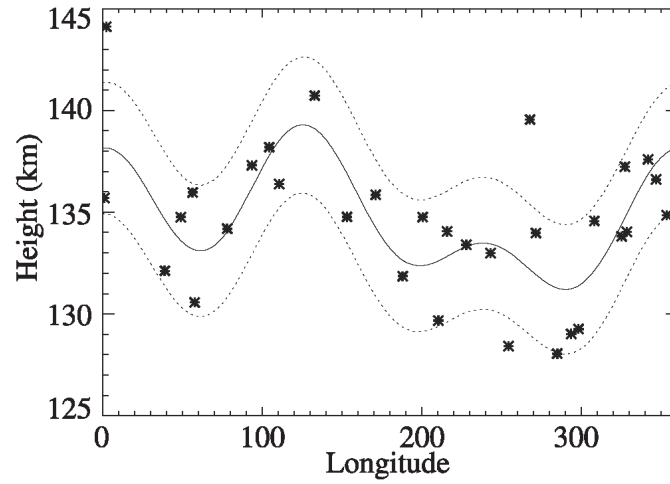
Fig. 9.8. Heights of primary electron density peak showing a wave pattern. (From Bougher *et al.*, 2004)
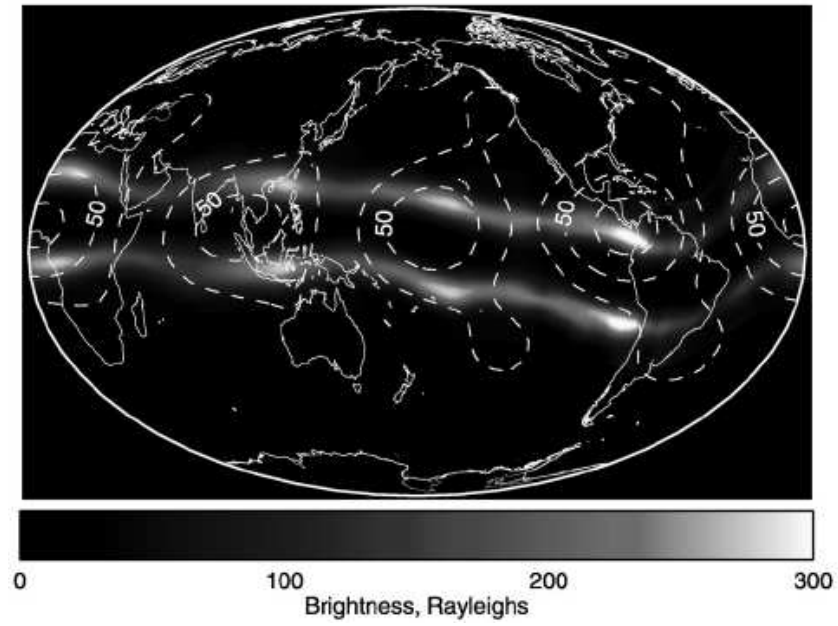
Fig. 9.9. Earth's FUV airglow showing a wave pattern. (From Immel *et al.*, 2006)
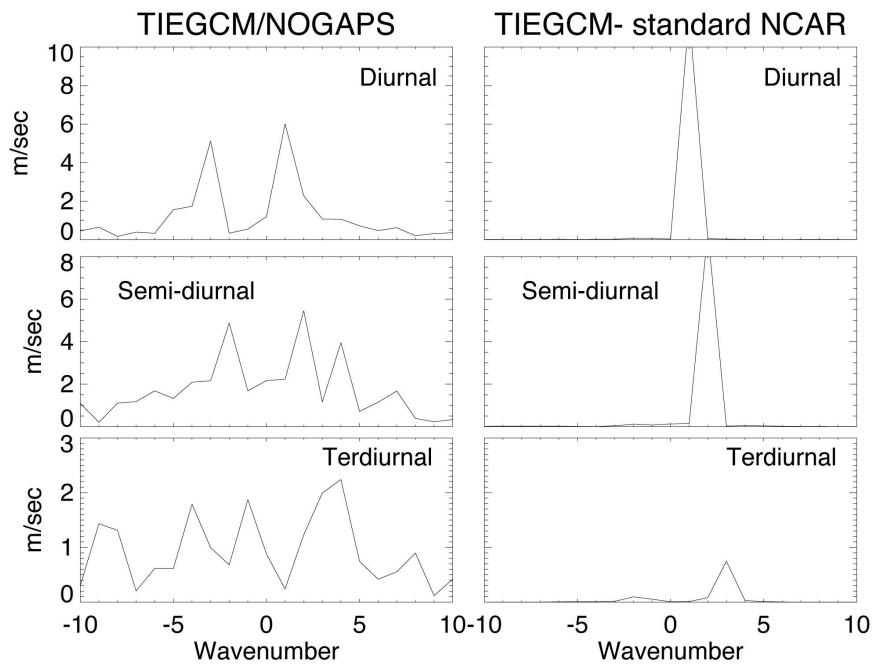
Fig. 9.10. Calculated spectrum of the lower thermospheric vertical wind, monthly averaged (March) at the equator near 115 km. The calculation on the left uses a model forced by realistic meteorological conditions from the NOGAPS-ALPHA assimilation system. The calculation on the right assumes only forcing from migrating diurnal and semi-diurnal tides.
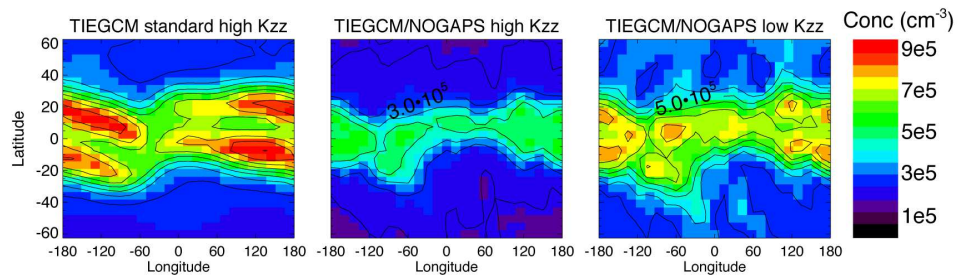
Fig. 9.11. Calculated averaged peak F2 electron density for March, 1300 local for 3 TIEGCM simulations. Left column uses standard $K_{zz} = 125$ m$^2$s$^{-1}$ with vertical winds from the right column of Fig. 9.7. Middle uses NOGAPS-ALPHA vertical winds. Rightmost field is with NOGAPS-ALPHA vertical winds and $K_{zz}$ divided by 5.
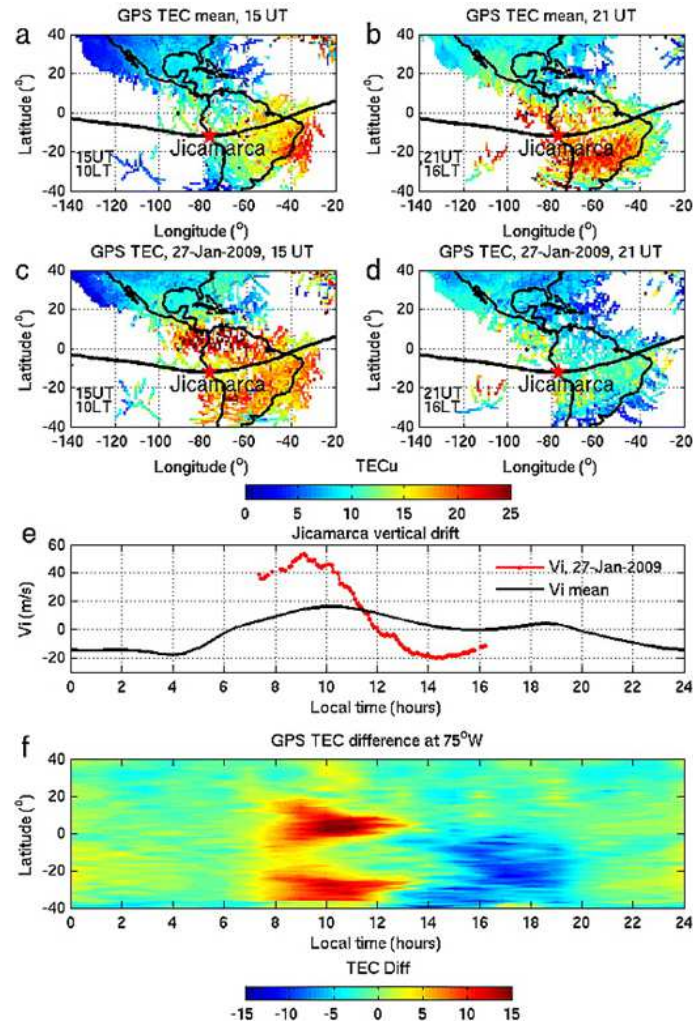
Fig. 9.12. Perturbations to the ionosphere, both total electron content (TEC) and vertical ion drift from the sudden stratospheric warming (SSW) of January 2009. The top row shows typical morning (15 UT = 10 local time at 75° W) and afternoon (21 UT) TEC fields over South America. The second row shows these fields after the SSW with a notable enhancement of TEC in the morning. The third panel shows the difference in the vertical ion drift as measured from Jicamarca Peru. The bottom row shows difference fields between the SSW perturbation and the mean case as a function of local time, emphasizing the morning TEC enhancement and the afternoon depletion. (From Goncharenko *et al.*, 2010)
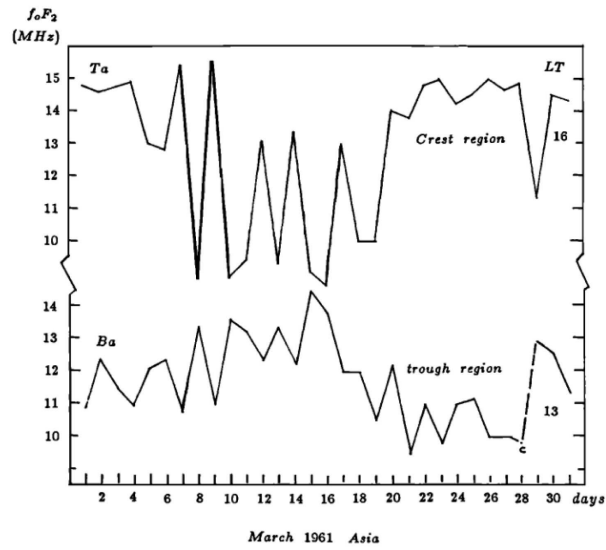
Fig. 9.13. Ionosonde data illustrating the oscillation of the peak F2 electron density variations with a quasi 2 day wave. (From Chen, 1992)
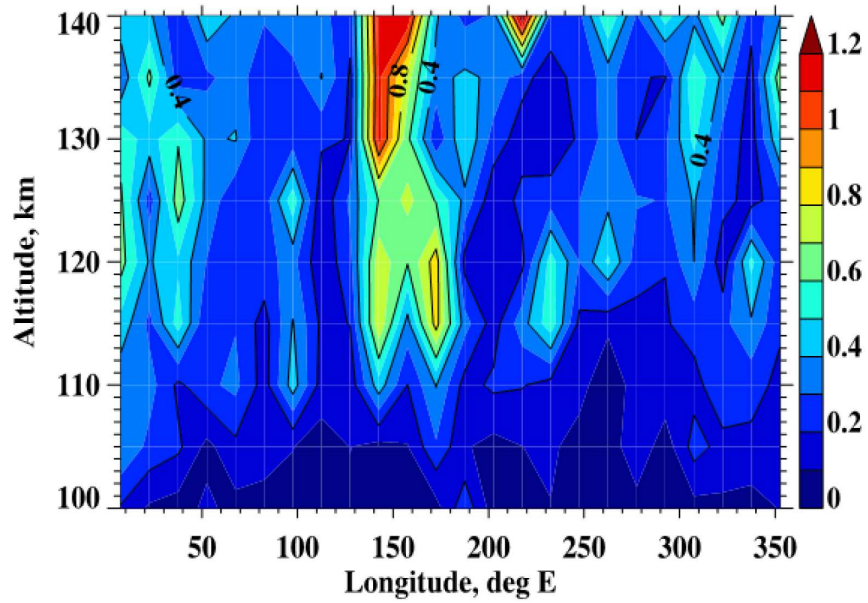
Fig. 9.14. Density variance data from the Mars Odyssey accelerometer in 15° and 5-km bins as function of longitude over about 127 orbits. (From Fritts *et al.*, 2006)

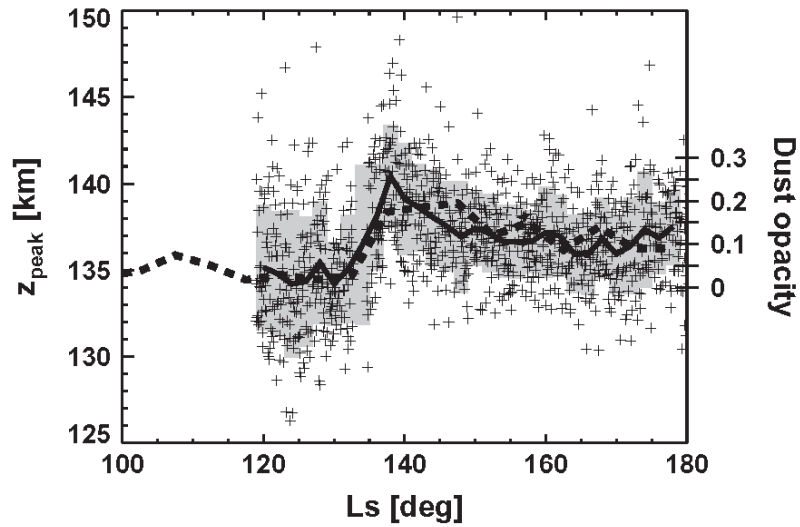Fig. 9.15. Martian ionospheric peak altitudes measured at latitudes $62° - 80°$ N by the MGS radio occultation instrument during a dust storm. Data are shown as crosses, the solid line is a $2°$ average, and the gray shading represents the $1\sigma$ variation. The dashed curve is the average dust opacity referenced to the right hand axis. (From Withers and Pratt, 2013)

# 10

# Moons, asteroids, and comets interacting with their surroundings

*Margaret G. Kivelson*
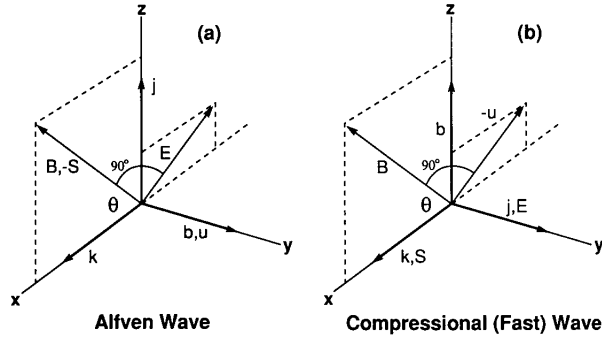
Fig. 10.1. Polarization of MHD waves in a uniform medium. The parameters other than **S** are defined in the text and are plotted with the wave vector along the $x$-axis and the background field (**B**) in the $x - z$ plane. The incompressible Alfvén wave polarization in plotted on the left and the compressional fast wave polarization is plotted on the right. **S** is the Poynting vector oriented in the direction in which energy density is transported by the wave: strictly field-aligned for the Alfvén wave and oblique for the compressional wave. (From Kivelson, 1995)
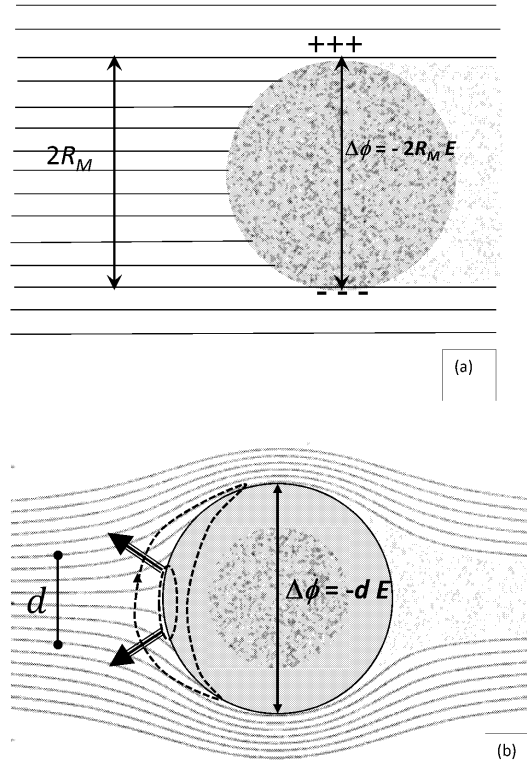
Fig. 10.2. Schematics of plasma flow (shown by lines of flow) at velocity $\mathbf{u}$ from the left onto (a) a non-conducting body and (b) a conducting body. In the plasma, $\mathbf{B}$ is into the paper, $\mathbf{E}$ is $-\mathbf{u} \times \mathbf{B}$ in both cases. Diagram (a) shows that a non-conducting body builds up surface charge that imposes a potential drop $\Delta\phi = -2R_M E$ across the diameter, producing an electric field that opposes the solar wind electric field. Diagram (b) shows the response of a conducting body that does not build up surface charge. Conducting paths allow current (shown schematically as a dashed line) to flow through the body and close in the incident flow. Heavy banded arrows identify the orientation of the resultant $\mathbf{j} \times \mathbf{B}$ force that diverts part of the incident flow. Because much of the incident flow has been diverted, the potential drop across the body is only $\Delta\phi = dE$, where $d < R_M$ is the distance in the incident flow between the flow lines that just graze the body. The electric field that penetrates the body is a fraction of the upstream field determined by the fraction of the upstream flow that impacts the surface. In the wake region, gray in both diagrams, the plasma pressure is reduced and the magnetic pressure is increased relative to the upstream values.
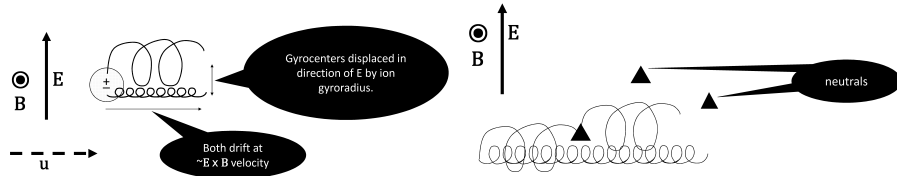
Fig. 10.3. Schematic of interactions with plasma with neutrals. *Left:* Initial motion of pickup ions and electrons. The gray circle represents a neutral composed of a positively charged ion and a negatively charged electron. The directions of plasma flow velocity, $\mathbf{u}$, of the magnetic field, $\mathbf{B}$, and of the electric field, $\mathbf{E}$, are indicated. In the image, following dissociation, the ion path starts upward and the electron path starts downward. Although initial motion is along $\mathbf{E}$ for the ion, but the Lorentz force causes the path to twist, resulting in motion around $\mathbf{B}$ at the ion cyclotron period, leading to a net drift at a velocity of $\mathbf{E}\times\mathbf{B}/B^2$. The electron initially moves in the $-\mathbf{E}$ direction. Its motion also rotates around B, but at the electron cyclotron frequency. The net effect is a transient current in the direction of $\mathbf{E}$. *Right:* Schematic of the effect of collisions with neutrals for a case with the collision frequency of order the ion cyclotron frequency. Pale blue triangles represent neutrals. The effect of collisions is to slow the motion in the $\mathbf{E} \times \mathbf{b}$ direction of the ions but not of the electrons and to displace the ions in the direction of $\mathbf{E}$. A net current arises, with one component along $-\mathbf{E} \times \mathbf{B}$ (a Hall current) and one component along $\mathbf{E}$, a Pedersen current.
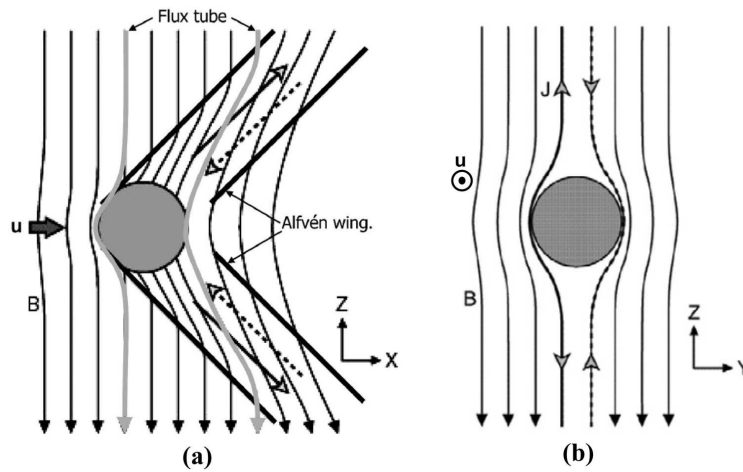
Fig. 10.4. Schematic representations of the interaction of a conducting body in a sub-magnetosonic plasma flow. (a) a cut through the center of the moon in the plane of the unperturbed field and the incident flow; (b) a cut through the center of the moon in the plane perpendicular to the incident flow. Field lines are thin black lines with black arrow-heads but are shown in gray on the edges of the flux tube containing field lines that penetrates the obstacle, the Alfvén wing boundaries are thick black lines, the upstream flow is shown as a heavy black arrow labeled **u**, currents are black lines with open arrow-heads, solid where the currents are directed away from the moon and dashed where they are directed towards the moon. (From Jia *et al.*, 2010)
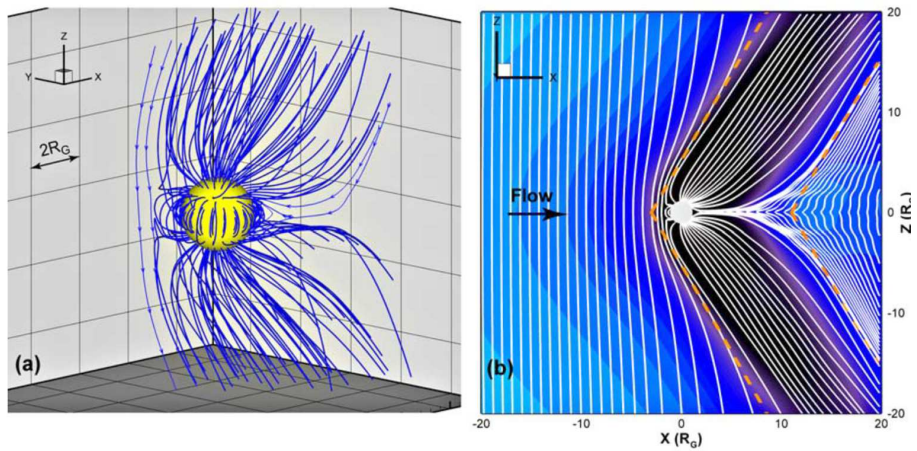
Fig. 10.5. (a) Selected magnetic field lines in Ganymede's magnetosphere from an MHD simulation. (b) Magnetic field lines projected onto the $x - z$ plane at $y = 0$. The $x$-component of the plasma flow velocity is shown in color. Orange dashed lines are tilted relative to the background field at the Alfvén angle and the flow is excluded from regions downstream of the left hand dashed lines, reappearing only in regions about 5 $R_G$ further downstream. In the simulation, the sphere of radius 1.05 $R_G$ is the inner boundary for plasma flow. (From Jia *et al.*, 2008)

(a)        (b)        (c)
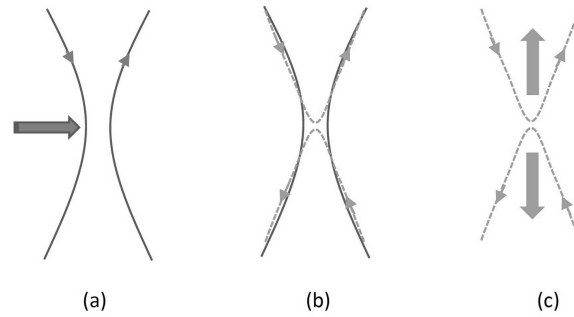
Fig. 10.6. Schematic of reconnection between oppositely oriented field lines. In (a) the southward oriented field of Jupiter flows (heavy blue arrow) towards the northward-oriented field of Ganymede. In (b), the field lines reconnect so that the northern end of a Jovian field line continues into the northern end of a field line from Ganymede. In (c), the kinks in the newly connected field lines accelerate plasma to the north and the south, with red arrows indicating the sense of flow.
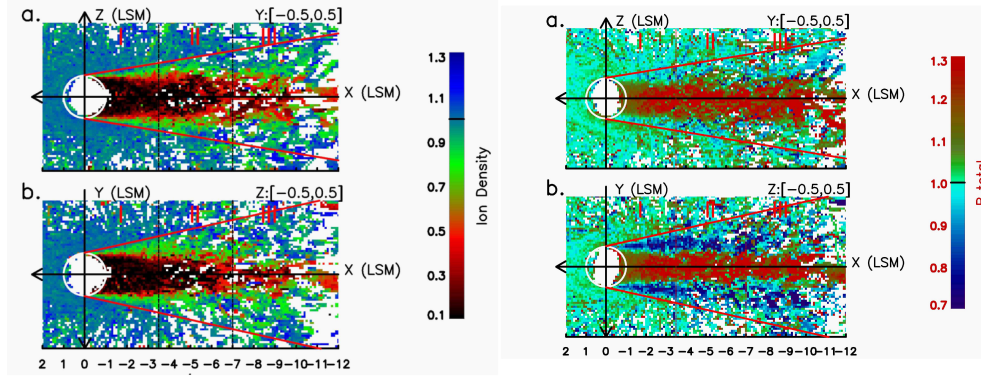
Fig. 10.7. Ion density (left) and magnetic field (right) in the vicinity of Earth's Moon from measurements by the Artemis spacecraft. The parameters represented by color are normalized by their values in the upstream solar wind. The $x$-axis is antiparallel to the solar wind flow. The data are plotted in the $x - z$ plane which is the plane of the solar wind field and the flow, and in the $x - y$ plane, perpendicular to this plane. The red lines diverging in the direction of negative $x$ denote the wake boundary across which the density changes significantly. The divergence from the wake center is controlled by the propagation of fast mode waves. (From Zhang *et al.*, 2014)
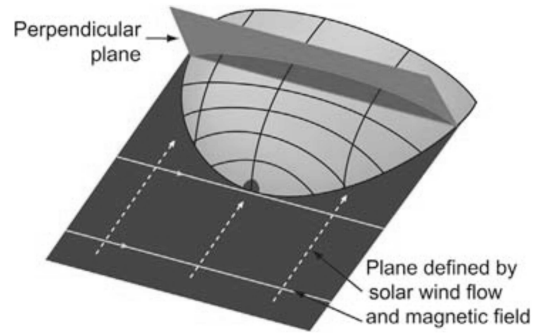
Fig. 10.8. Schematic of interaction region surrounding an asteroid of scale not large compared with ion gyroradii in the solar wind. Notice that the interaction region is extended along the field direction and compressed in the direction perpendicular to the field and the flow. (From Kivelson and Bagenal, 2007; credit: Steve Bartlett)
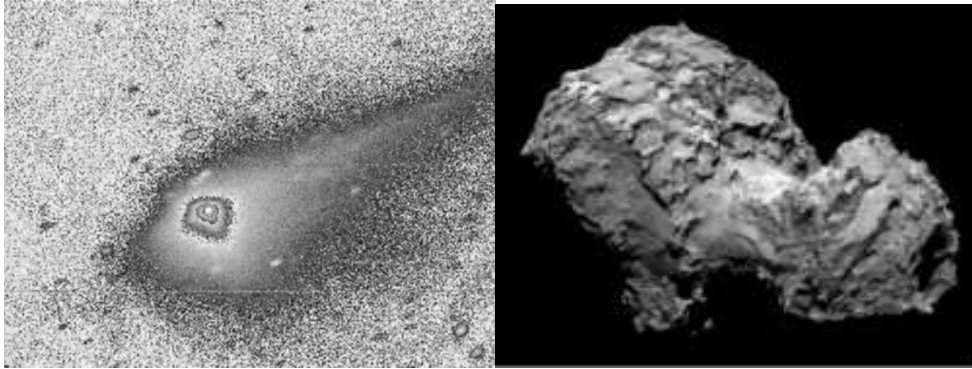
Fig. 10.9. *Left:* Image of comet Churyumov-Gerasimenko from the 3.6 m telescope of the European Southern Observatory, La Silla/Chile. The comet was at 2.49 AU from the Sun when imaged on March 9, 2004. East is to the left and north is up. The nucleus is a source of asymmetric emissions. The scale is 70,000 km EW and 50,000 km NS. (From Glassmeier *et al.*, 2007) *Right:* Image of the nucleus acquired by Rosetta spacecraft on August 3, 2014. (Courtesy ESA/NASA - Rosetta spacecraft.)

# 11
# Dusty plasmas

*Mihály Horányi*
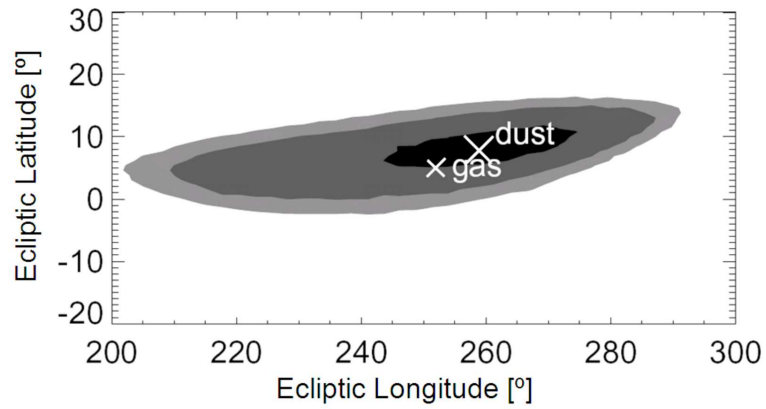
Fig. 11.1. The upstream direction of the interstellar dust flux observed by Ulysses is $\lambda = 259 \pm 20°$ and $\theta = 8 \pm 10°$ ecliptic longitude and latitude, respectively. The contour plot shows 1, 2, and 3 $\sigma$ confidence levels as black, dark gray, and light gray. The helium upstream direction is $\lambda = 254°, \theta = 5.6°$. (From Frisch *et al.*, 1999)
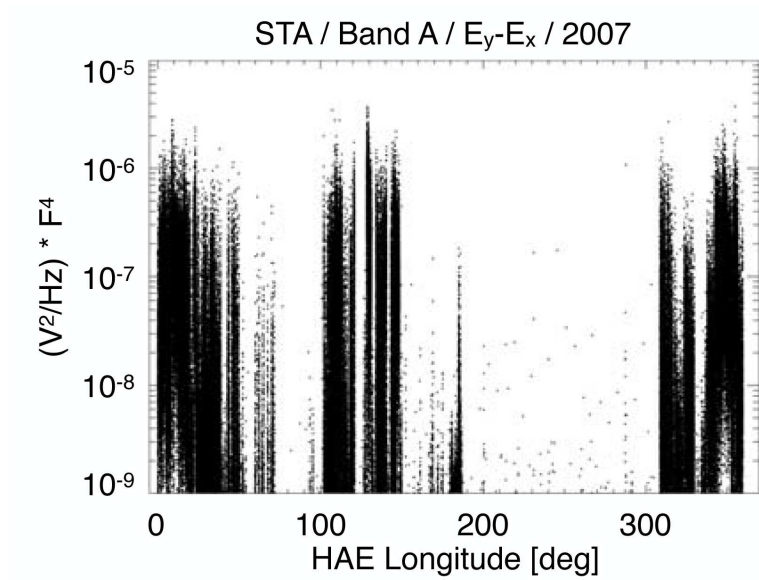
Fig. 11.2. The average power observed by the STEREO/WAVES low-frequency receiver on STEREO A as a function of ecliptic longitude during 2007. The periods of high amplitudes have been suggested to be caused by high-speed nano-dust striking the spacecraft. (From Meyer-Vernet *et al.*, 2009)
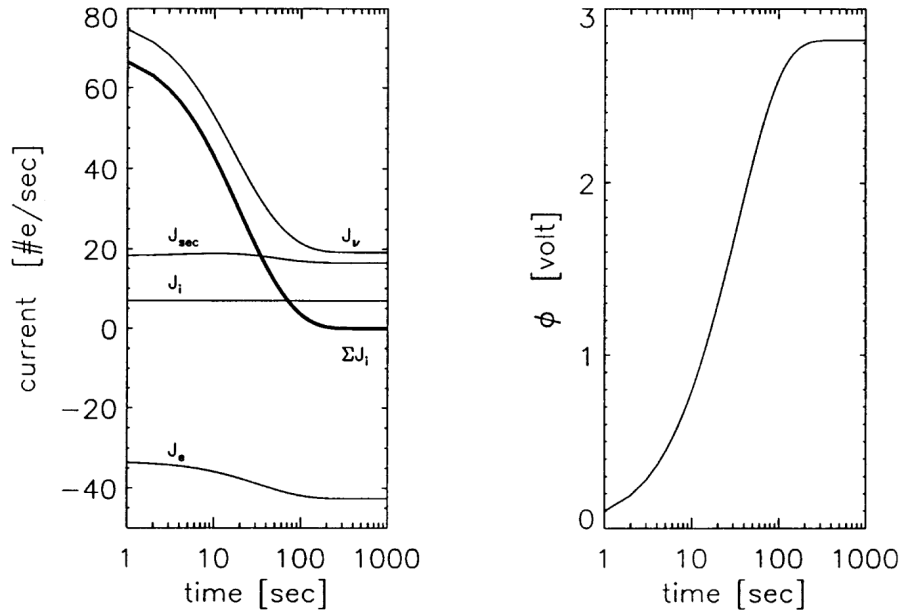
Fig. 11.3. The evolution of the electron and ion thermal currents, $J_e, J_i$; secondary and photo-electron currents $J_{sec}, J_\nu$, and their sum $\sum J_k$ (left panel); and the electrostatic surface potential $\phi$ (right panel) of an initially uncharged dust particle with radius $a = 1$ $\mu$m at a heliocentric distance of 1 AU. (From Horányi, 1996)
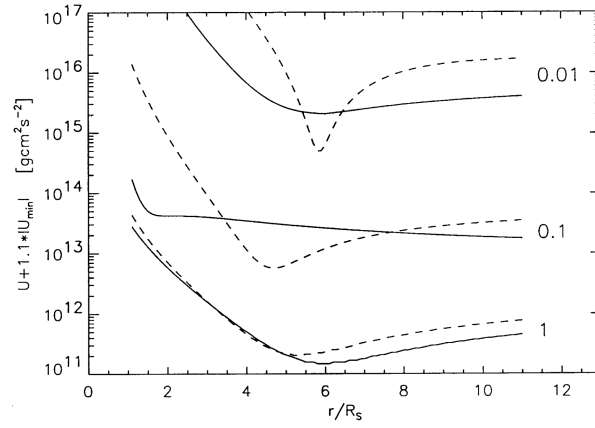
Fig. 11.4. The effective potential for dust grains with $a = 0.01, 0.1,$ and 1 $\mu$m started from Io on circular Kepler orbits with $\phi$ = -30 (dashed lines) and +3 V (continuous lines). To avoid the overlap of these curves, because only their shape is important, we have shifted them apart by plotting $U + 1.1|\text{minimum}(U)|$ instead of $U$ itself. (From Horányi *et al.*, 1996)
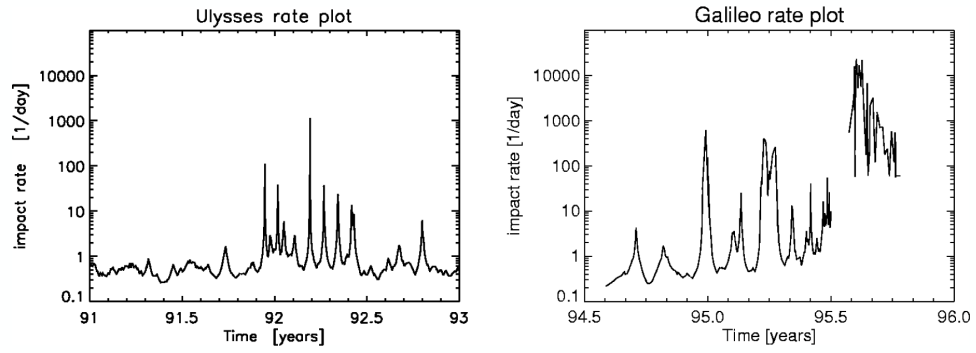
Fig. 11.5. Dust impact rates measured by Ulysses (*left*) and by Galileo (*right*) at Jupiter. (From Horányi *et al.*, 1996)
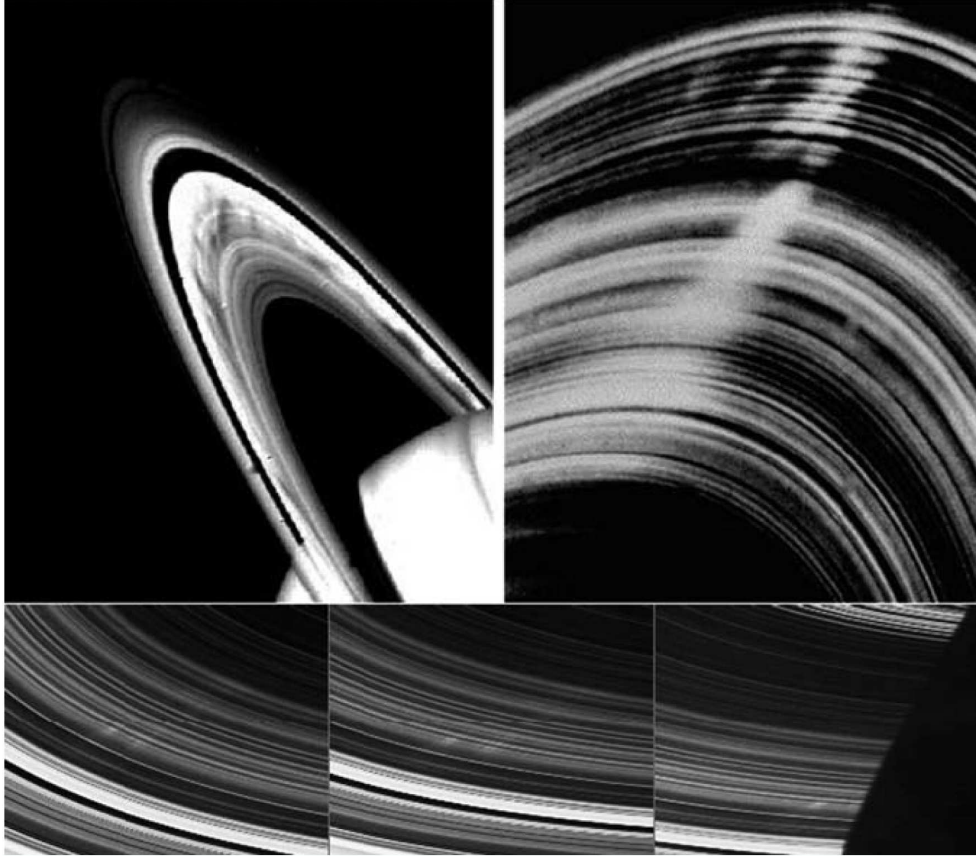
Fig. 11.6. *Top*: Spokes in the B ring as seen by Voyager 2 (Smith *et al.*, 1982). The left image was captured in back-scattered light before closest encounter, with the spokes appearing as dark radial features across the ring's center. The right image was taken in forward-scattered light after the spacecraft crossed the ring plane, and was looking back towards the Sun; the spokes now occur as bright markings. Typical dimensions of these spokes are 10,000 km in length and 2,000 km in width. The nature of the changing brightness indicates that spokes consist of small submicron sized grains, *i.e.*, that are comparable in size to the wavelength of visible light. At the time these images were taken, the rings' opening angle to the sun was $B_0 \simeq 8°$. *Bottom*: The initial spoke observations taken by Cassini on September 5, 2005 ($B_0 \simeq 20°$), over a span of 27 min. These faint and narrow spokes were seen from the un-illuminated side of the B ring. These first spokes are $\simeq 3,500$ km long and 100 km wide, smaller than the average spokes seen by Voyager. These images were taken with a resolution of 17 km per pixel at a phase angle of 145° when Cassini was 135° above the unlit side of the rings as the spokes were about to enter Saturn's shadow (Mitchell *et al.*, 2006).
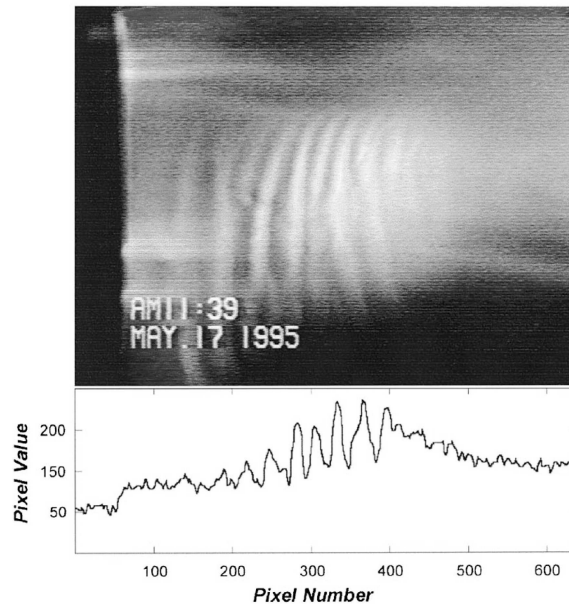
Fig. 11.7. Single video frame image of a Dust Acoustic Wave (DAW) observed in the laboratory. The bright vertical bands correspond to the wave crests (dust compressions). The glow is the light emission from the plasma. The entire image covers 640 (vertical) pixels by 320 (horizontal) pixels. The bottom plot is the horizontal intensity map (pixel values) of pixel row 200. The wavelength of this DAW $\lambda \simeq 0.6$ cm was measured directly from a single frame video image. The wave phase velocity $v_\varphi \simeq 9$ cm/s was determined from an analysis of successive frames of video images. (From Thompson *et al.*, 1999)

# 12

# Energetic-particle environments in the solar system

*Norbert Krupp*
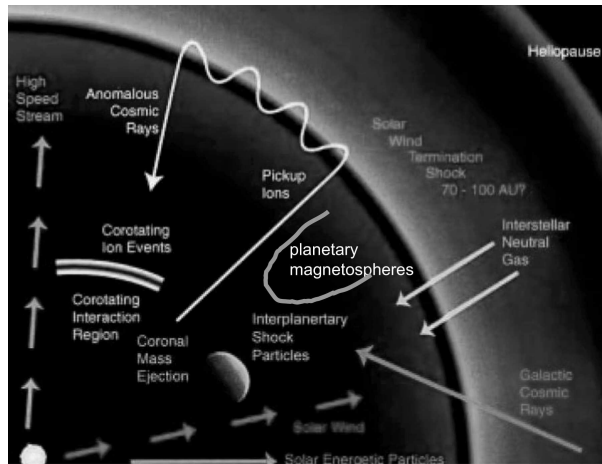
Fig. 12.1. Sources of energetic particles in the heliosphere. (Adapted from www.issibern.ch/teams/Suprat)
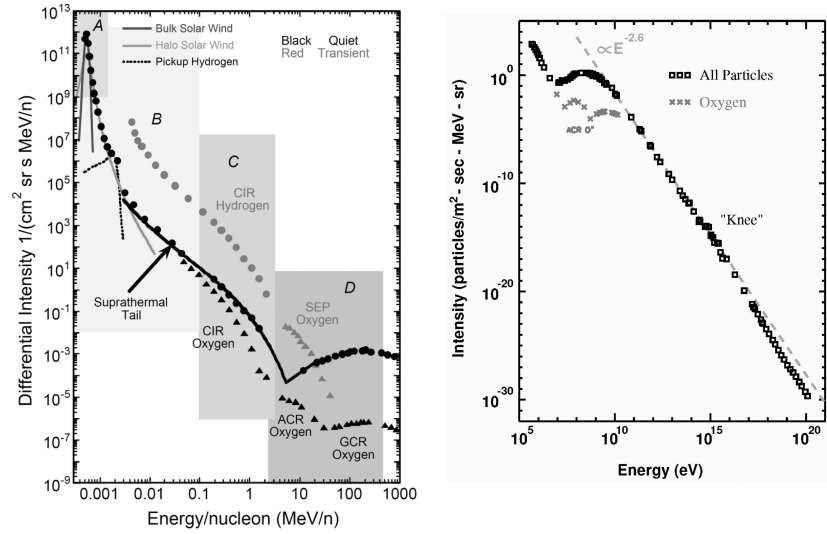
Fig. 12.2. Energy spectra of energetic particles in the heliosphere (left) and for cosmic rays (right). The curves illustrate the energy spectra during quiet time and disturbed solar wind conditions. The dots and triangles represent the suprathermal part of the spectrum and the particles accelerated at corotating interaction regions (CIRs), galactic cosmic rays (GCRs), and the anomalous cosmic rays (ACRs) together with Solar Energetic Particles SEPs. The right figure shows the high-energy part of the galactic cosmic ray energy spectrum to TeV energies. Note the characteristic peak at about 10 MeV and the $E^{-2.6}$ power law dependence for energies above the peak. (Figure adapted from Ch. 3 in Vol. II)
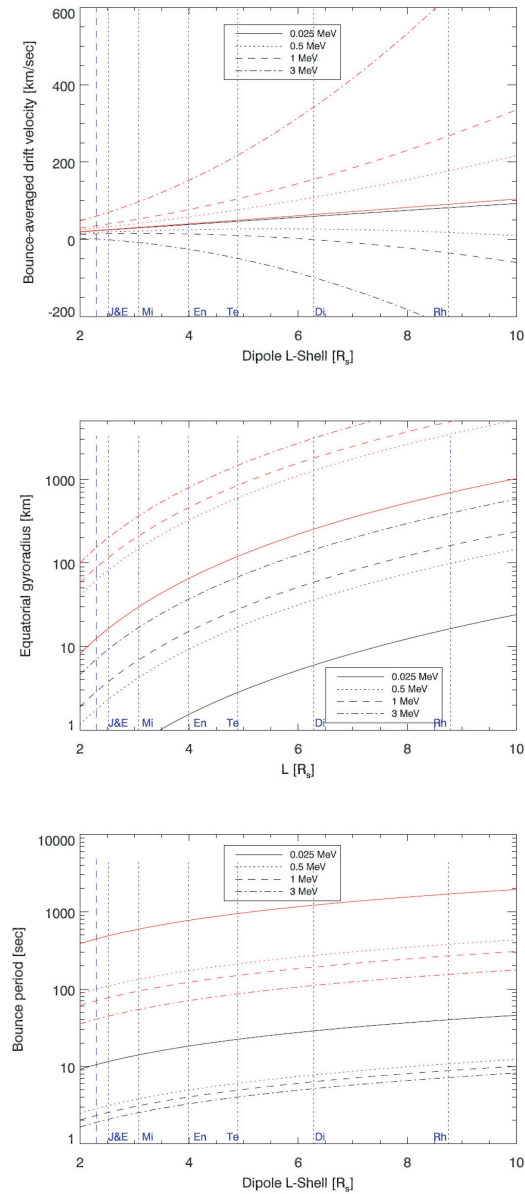
Fig. 12.3. *Top*: Bounce averaged drift velocities at Saturn as a function of energy and L-shell (black curves for electrons and red curves for ions). All values are for equatorial particles (90 degree pitch angle) assuming rigid corotation in an inertial, Saturn-centered coordinate system. *Middle*: Same plot for the gyroradius of equatorial electrons and ions. *Bottom*: Bounce period of electrons and ions with a pitch angle of 45 degrees. In all panels, the location of the various icy moon L-shells are indicated with blue, dotted lines. The blue dashed line indicates the L-shell of the main rings outer edge. (From Roussos, 2008)
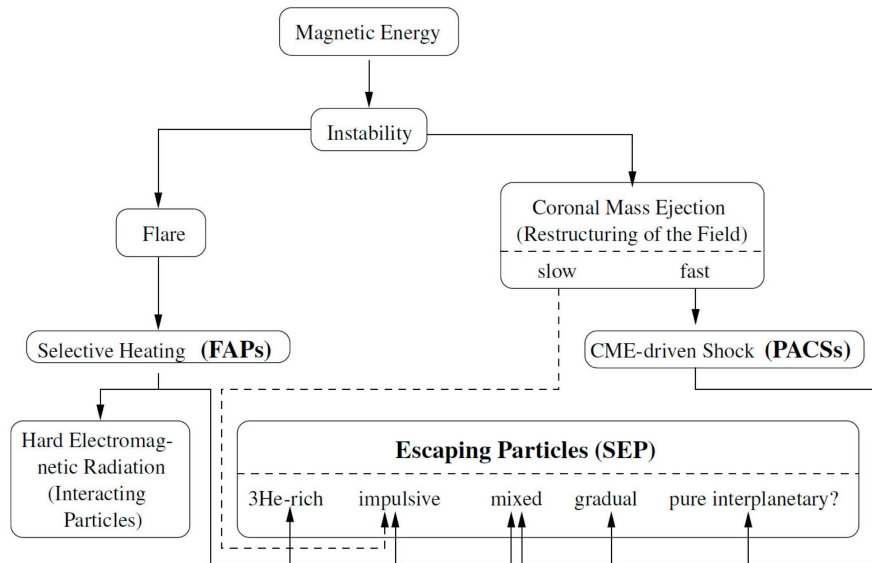
Fig. 12.4. Classification of solar energetic particle events. (From Kallenrode, 2003)
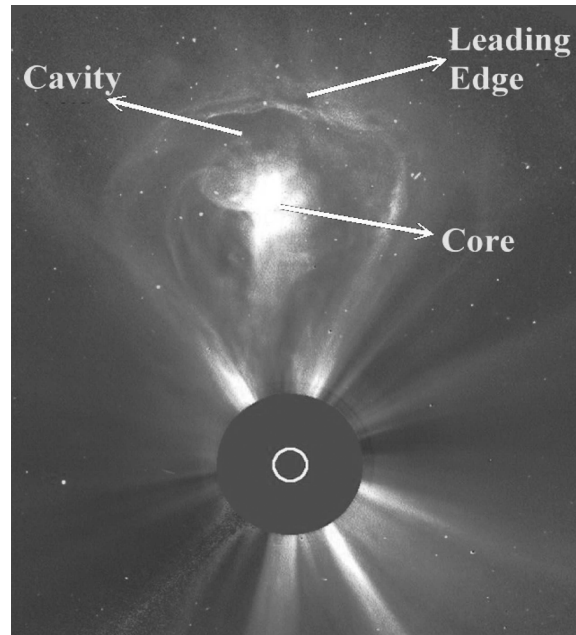
Fig. 12.5. CME spatial structures. (From Rodriguez, 2005)
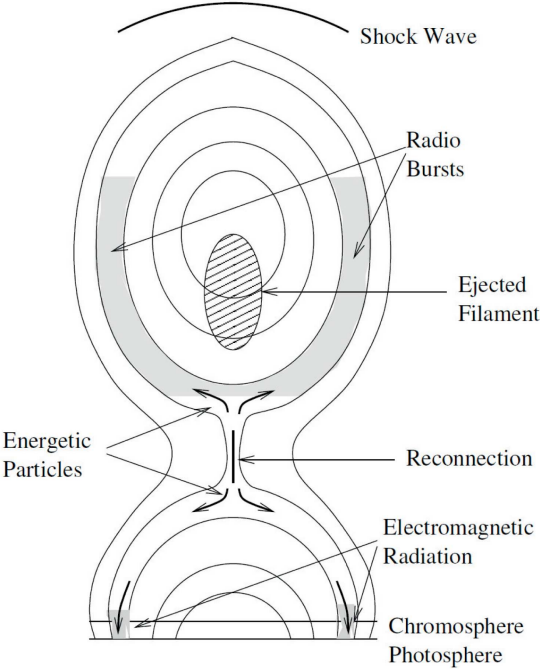
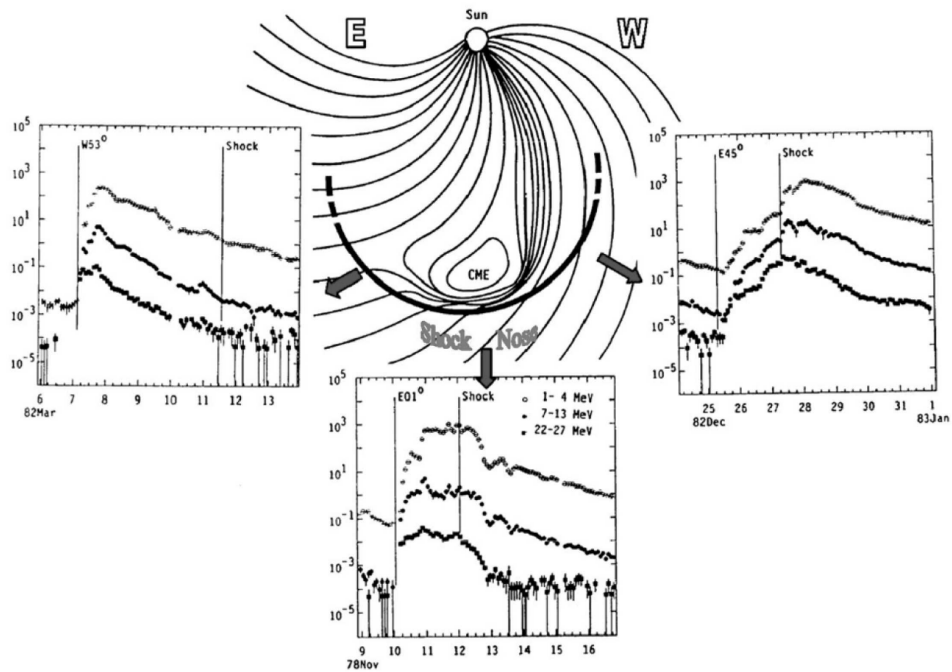Fig. 12.6. Concepts of particle acceleration in a solar gradual event. (Adapted from Kallenrode, 2003)

Fig. 12.7. Intensity-time plots of particle fluxes ejected from three different solar longitudes with respect to the nose of the shock front. (From Reames, 2013)
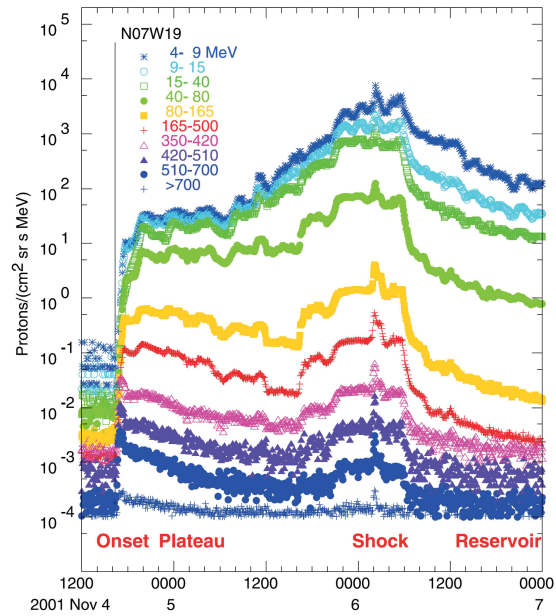
Fig. 12.8. The four phases of a large gradual CME event compared to energy-dependent energetic particle fluxes. This event was observed by NOAA/GOES space-craft at 1 AU. Different colors indicate the intensities of protons for different energies. (From Reames, 2013)
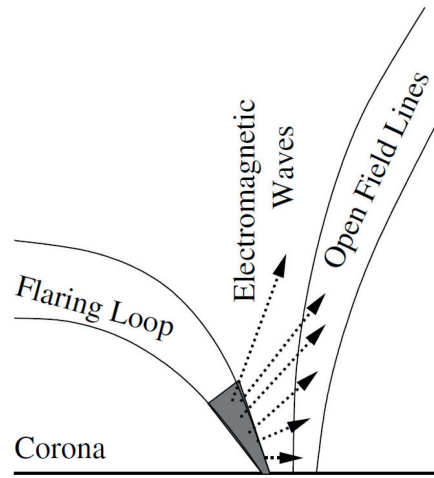
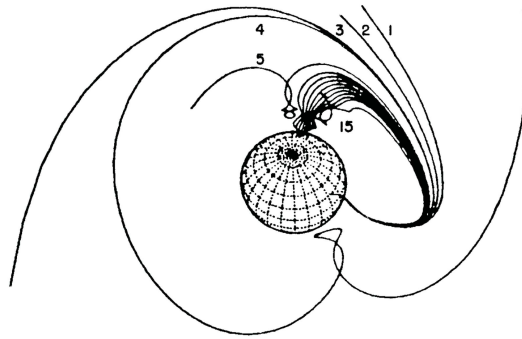Fig. 12.9. Concept of particle acceleration in an impulsive flare. (Adapted from Kallenrode, 2003)
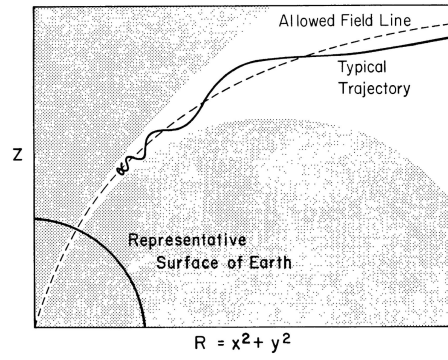
Fig. 12.10. Trajectories of cosmic rays in a planetary dipole field. (Adapted from Smart *et al.*, 2000)
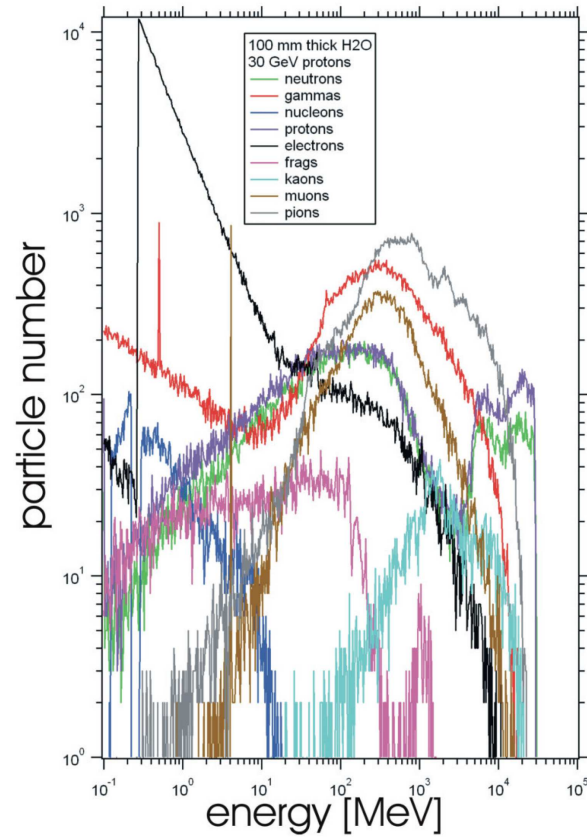
Fig. 12.11. Galactic cosmic ray spectra for various particle populations. (Diagram provided by D. Haggerty, JHUAPL)
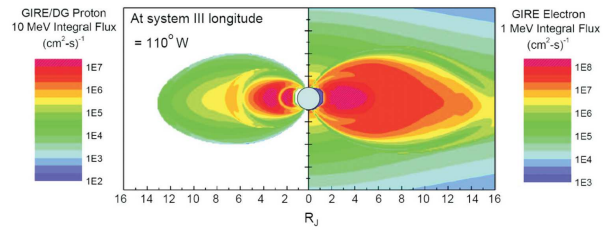
Fig. 12.12. Two-dimensional integral flux distributions for electrons (right section) and protons (left section) at Jupiter based on the Divine-Garrett/GIRE radiation models. (From Paranicas *et al.*, 2009)
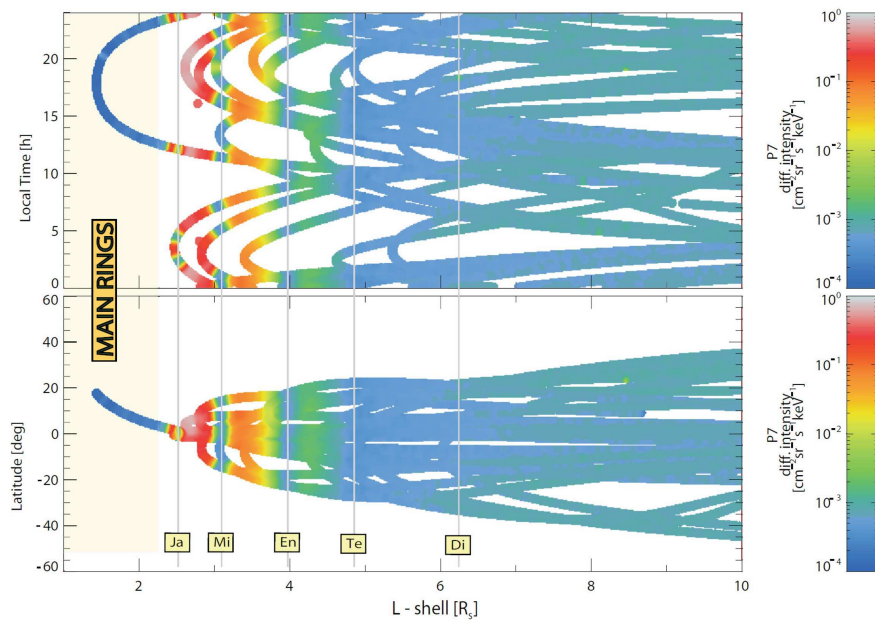
Fig. 12.13. Macrosignatures of energetic ions in the inner magnetosphere of Saturn as a function of L-shell and either local time (upper panel) or latitude (lower panel). Color-coded are the differential intensities of ions ($> 10\,\mathrm{MeV/nucleon}$) as measured between 2004 and 2007 by the Low Energy Magnetospheric Measurement System LEMMS onboard the Cassini spacecraft. (From Roussos 2008)
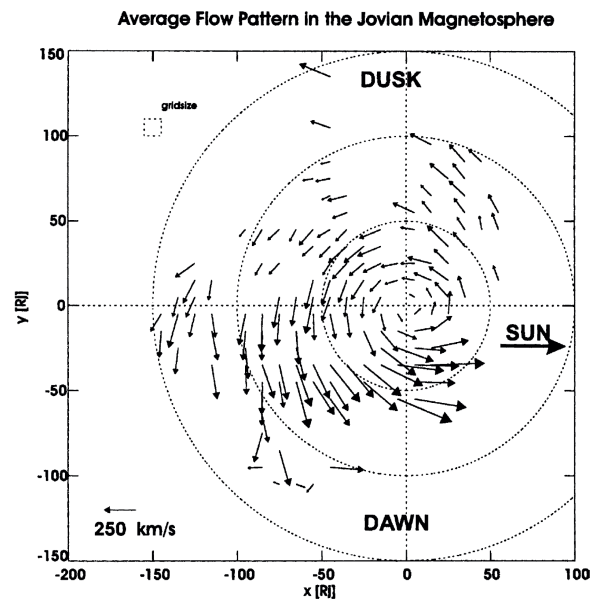
**Average Flow Pattern in the Jovian Magnetosphere**



Fig. 12.14. Global flow patterns around Jupiter as derived from Galileo emetic particle measurements binned in 10x10 $R_J$ bins. (From Woch *et al.*, 2004)
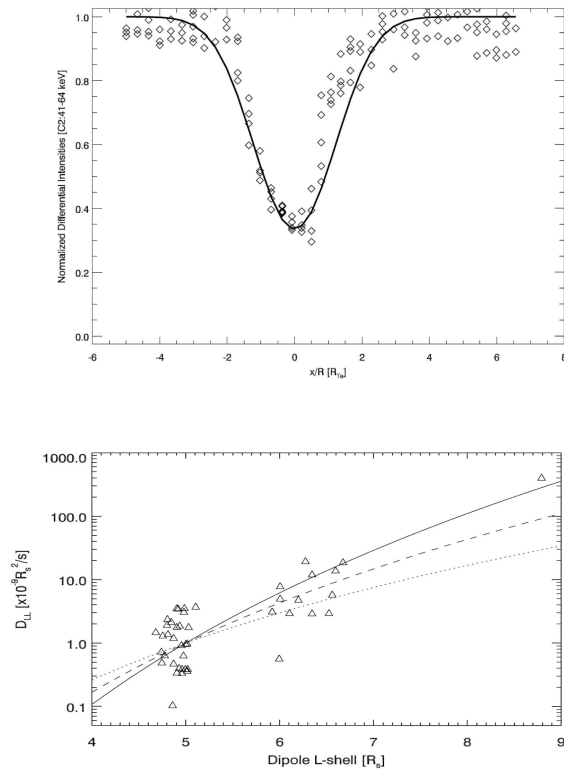
Fig. 12.15. *Top*: The symbols are the microsignature of Saturn's moon Tethys, the solid curve is the best fit. *Bottom*: L-dependence of radial diffusion coefficient $D_{LL}$. (From Roussos *et al.*, 2007)
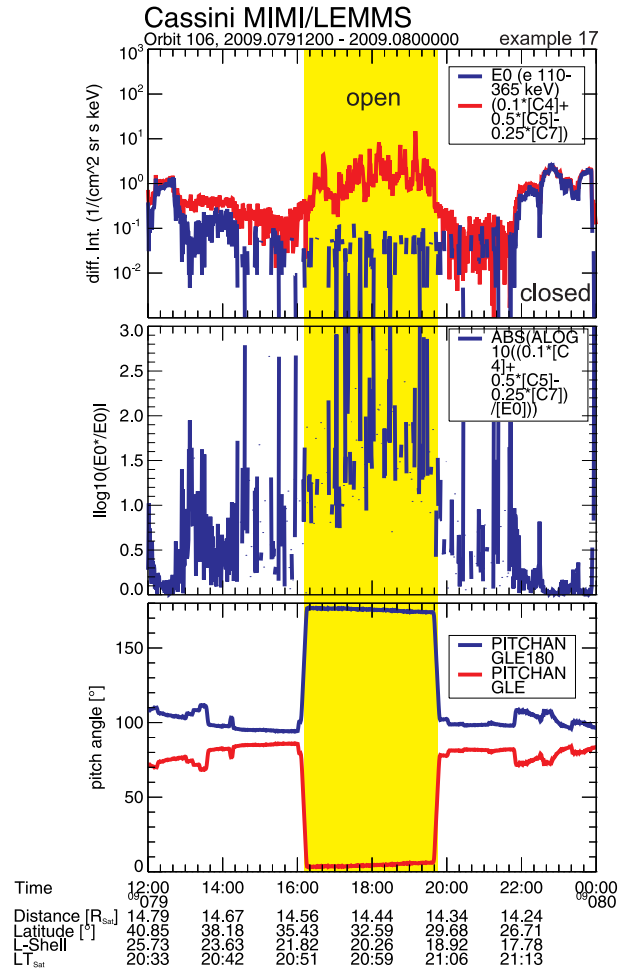
Fig. 12.16. Intensity of electrons along and against the magnetic field direction inside Saturn's magnetosphere.

# 13

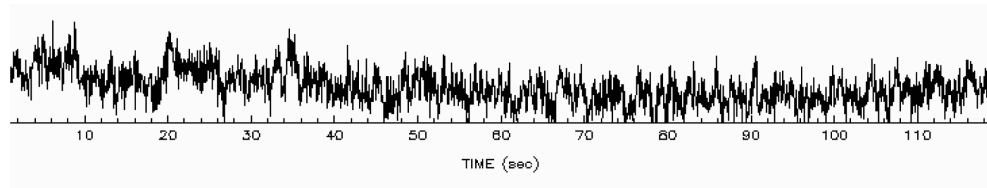# Heliophysics with radio scintillation and occultation

*Mario Bisi*

Fig. 13.1.  Intensity fluctuation seen in a single observation of IPS using the Sodankylä site during an EISCAT observation on 05 September 2004 with radio source J1256-057 (3C279). (From Bisi, 2006)
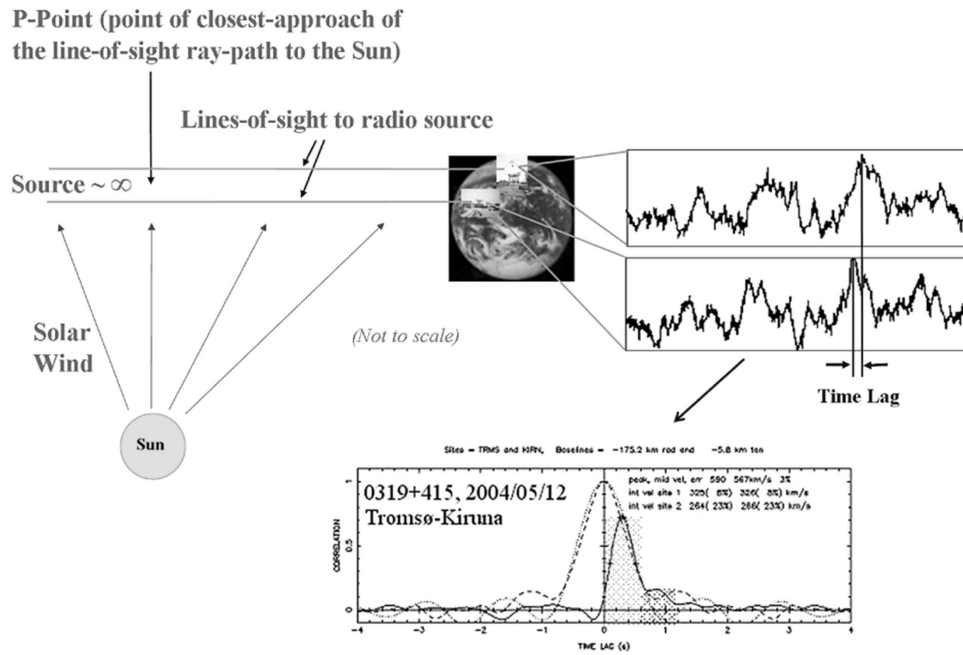
Fig. 13.2. The basic principles of multi-site IPS (in this case two EISCAT radar antennas, Tromsø and Kiruna) through the simultaneous observation of a single radio source as described in the text. The signal's amplitude variation is directly related to turbulence and density variation in the solar-wind outflow crossing the line of sight (LOS). A cross-correlation analysis of the two simultaneous signals received yields what is known as a cross-correlation function (CCF) which can be used as a first estimate of the velocities crossing the LOS. (From Bisi *et al.*, 2010b)
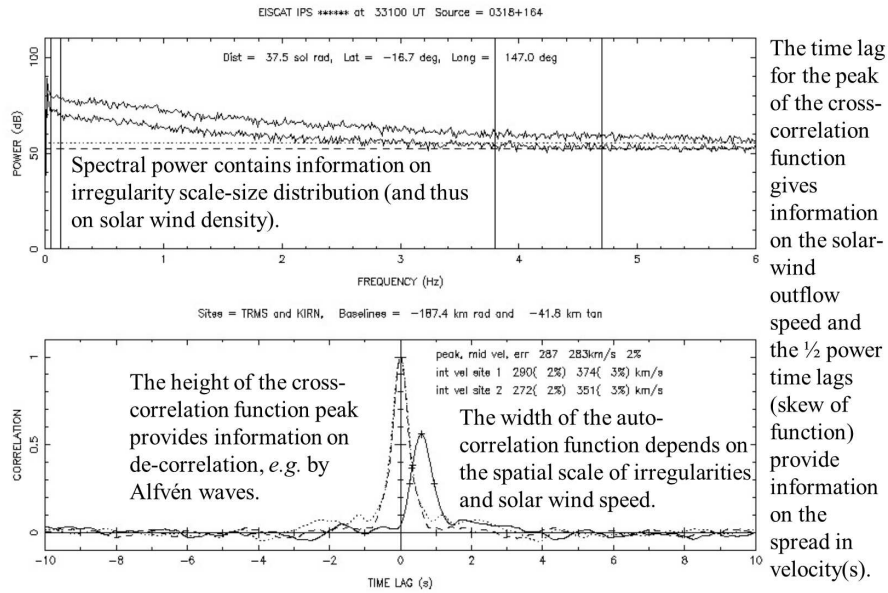
Fig. 13.3. The top plot displays an example Fourier-transformed spectrum from the two time series of a multi-site observation of IPS with EISCAT. The bottom plot shows a CCF of this observation. The vertical lines on the power spectrum to the left are the high-pass filters for each of the two sites and similarly to the right are the low-pass filters for each of the two sites. (Courtesy of R.A. Fallows)
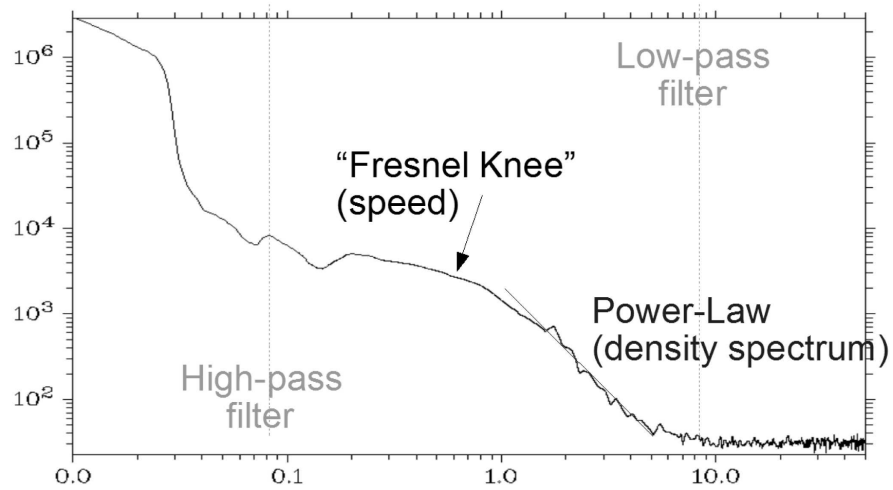
19950529 : 01:30:00 : 0318+164 : Sdky



Fig. 13.4. An example IPS power spectrum on a log-log scale. The aforementioned low- and high-pass filters are more-clearly illustrated and individually labeled. The Fresnel knee is related to the speed/velocity of the solar-wind outflow, and the power-law is related to the density. (Courtesy of R.A. Fallows)
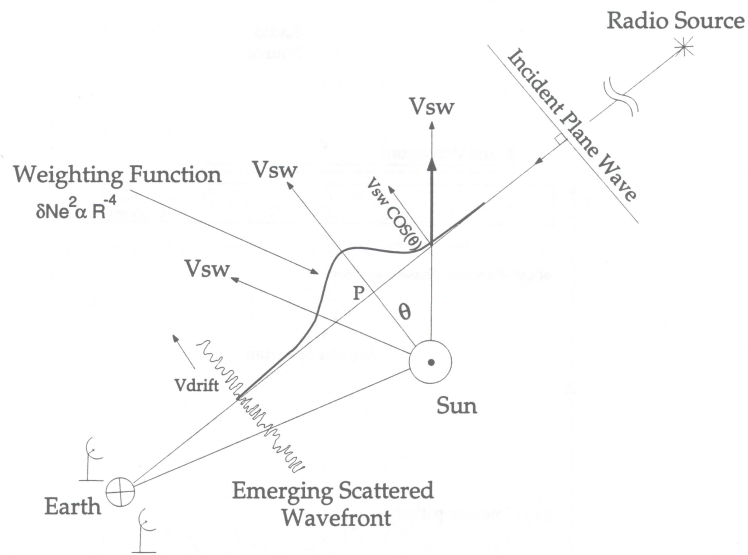
Fig. 13.5. The geometry of observations of IPS and how the weighting of scintillation potential along the LOS from the radio telescopes to the source varies due to the solar wind flowing across the LOS at different angles. (From Grall, 1995)
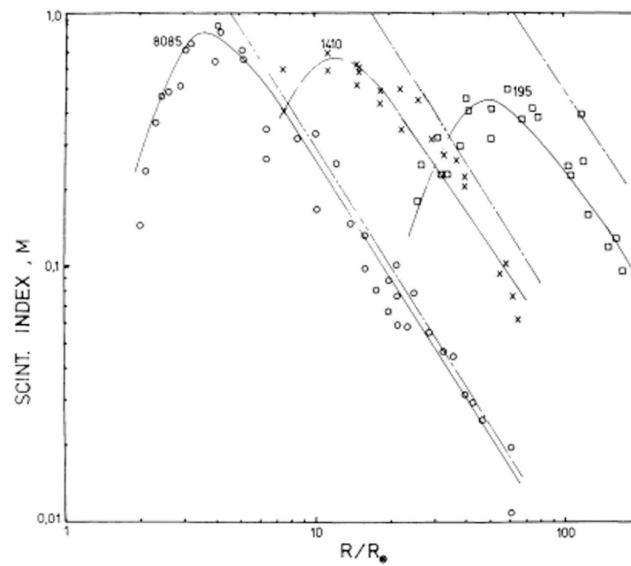
Fig. 13.6. A log-log plot showing for three different IPS observing frequencies of 8085 MHz, 1410 MHz, and 195 MHz, the scintillation index (m) response with distance from the Sun (in units of solar radius Rsun). The scintillation index is the square of the scintillation power received at the antenna while observing a particular radio source. As illustrated by the figure, the higher the observing frequency, the closer-in to the Sun the peak in the scintillation index occurs and hence higher observing frequencies can be used to enable observations in the weak-scattering regime closer-in to the Sun as described by the earlier equations. (From Coles, 1978)
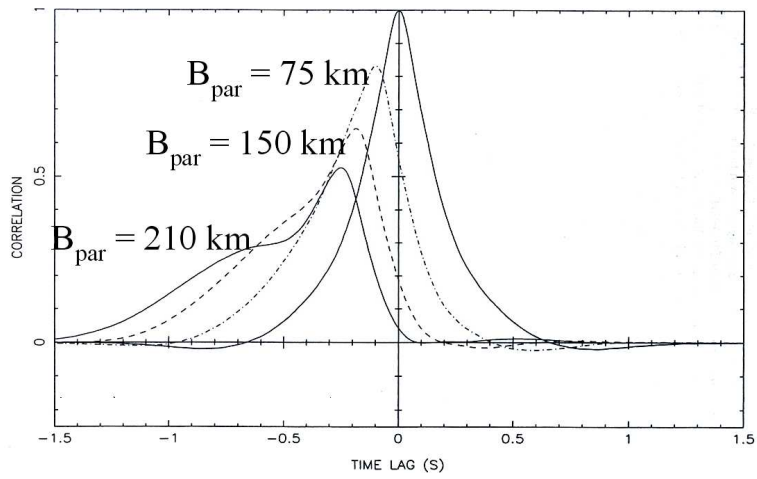
Fig. 13.7. The effect of increasing the parallel baseline ($B_{\mathrm{Par}}$) of a multi-site observation of IPS on the CCF. (From Klinglesmith, 1997)
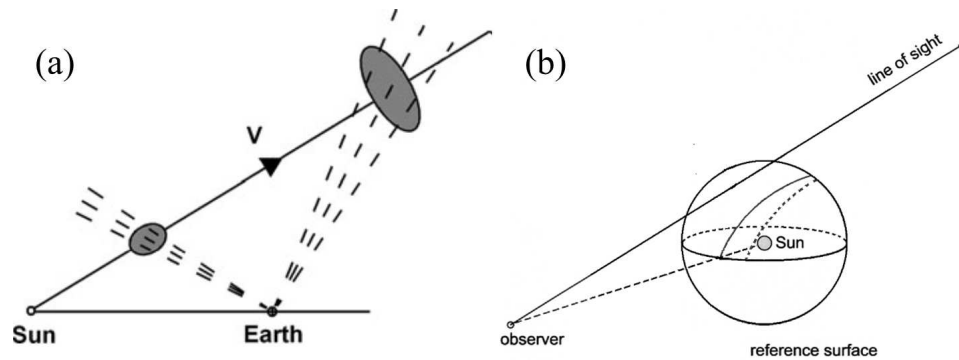
Fig. 13.8. The left-hand image (a) shows a schematic of the outward-flowing solar-wind structure which we know follows very specific physics as propagation away from the Sun takes place. By observing large areas of the sky with time, this allows individual features to be observed several times over time and this has the same effect as a moving detector in a comparable-instantaneous time such as CAT scans used in medical imaging where sensors rotate around the body and not the body moving through the sensors in time. The right-hand image (b) depicts a schematic of how an individual IPS LOS maps/projects onto the source (reference) surface for use in the UCSD 3-D CAT; the solid line is the immediate projection of the LOS to this surface and the dashed line is the projected location that takes into account the solar wind speed. (adapted and combined from Jackson *et al.*, 2010a; 2011b)
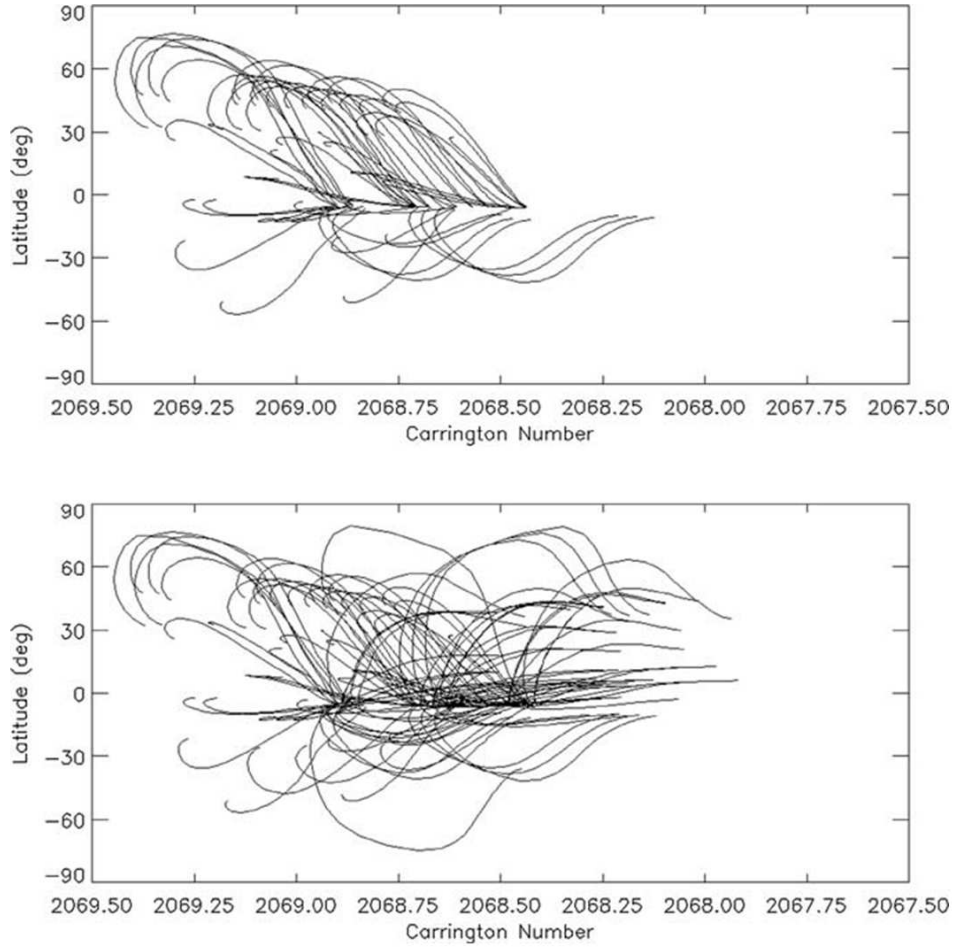
Fig. 13.9. The STELab IPS lines of sight used by the UCSD 3-D CAT from $g$-level (top) and velocity (bottom) determinations from observations of IPS using the STE-Lab system mapped back to the $15\,R_\odot$ source surface (lower boundary) in the UCSD 3-D CAT. The display is over two Carrington rotations (CRs), and as can be seen, the velocity coverage is far greater onto these two CR maps used for the tomography (CR2067.50 to CR2069.50) than that of the $g$-level coverage in this particular example. The numbers of data points (lines of sight used) for velocity and $g$-level need not be the same and indeed often differ. (From Bisi *et al.*, 2009a)
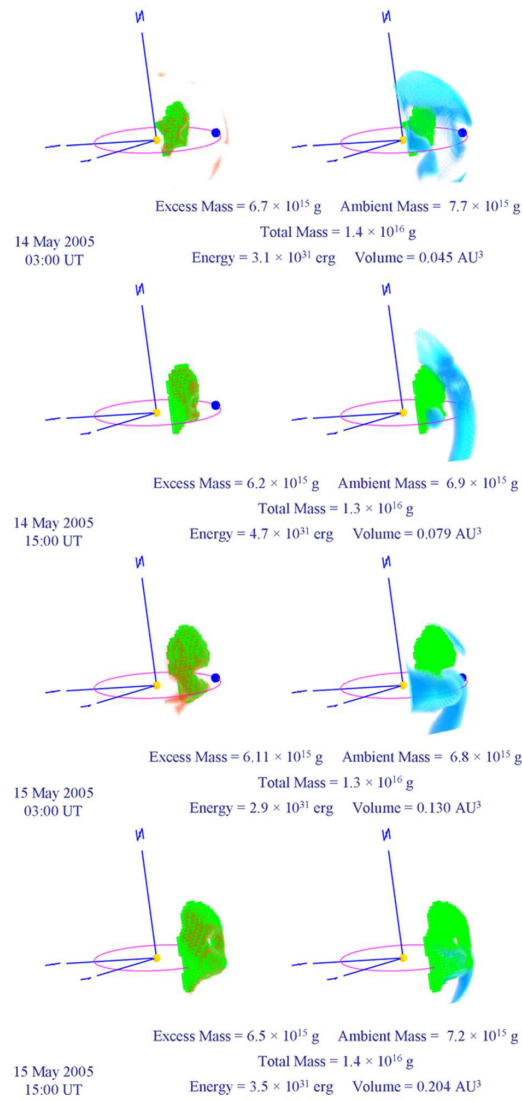
Fig. 13.10. The 3-D CAT reconstructed visualization of the distribution of solar-wind density upwards of $8\,\mathrm{e\,cm^3}$ (brighter colors toward yellow mean increasing density) on the left-hand side and high-velocity portions (blue) on the right-hand side showing the developing and changing reconstructed structure of the 13 to 15 May 2005 coronal mass ejection (CME) event sequence. The left-hand density images are highlighted with green cubes to encompass the reconstructed volume of the mass portion of the CME. This same highlighted volume is depicted on the right-hand velocity reconstructions for illustrative purposes. Each image is labeled with the masses, volume, and energy values on each date and time. All non-CME-related features have been removed for clarity of viewing when displaying the 3-D volume. The axes are heliographic coordinates with X-axis direction pointing toward the vernal equinox, and Z-axis directed toward solar heliographic North. A $\mathrm{r}^2$ density increase has been added to better-show structures further out from the Sun (the central sphere) to the Earth (the blue sphere) along with the Earth orbit (ellipse). (From Bisi *et al.*, 2010a)
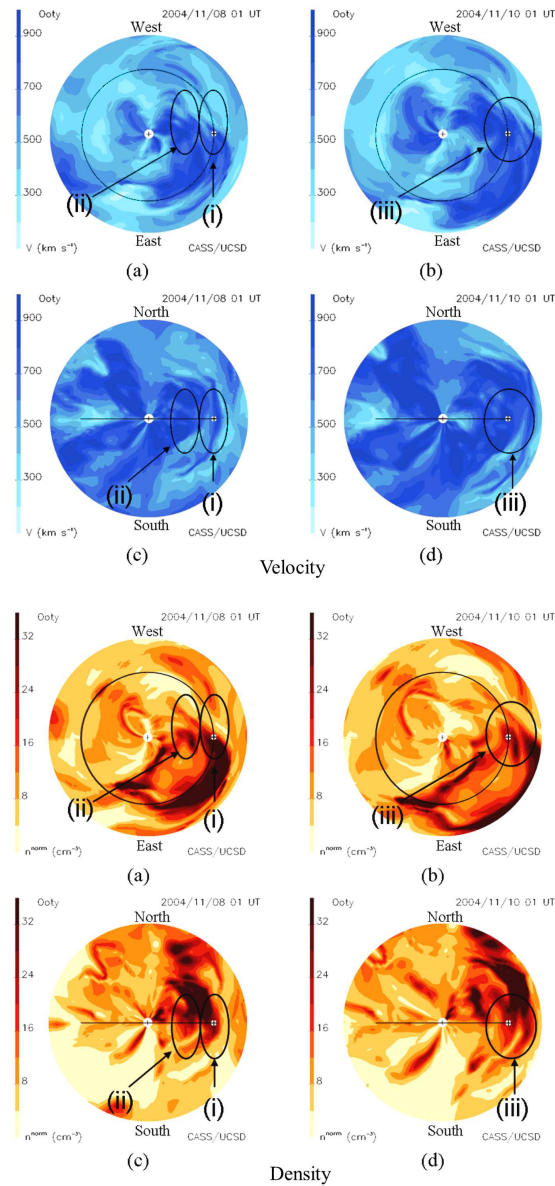
Fig. 13.11. Summary figure of the Ooty ecliptic-, (a) and (b), and meridional-, (c) and (d), cuts through the 3-D velocity (blue color scale – top set of images) and density (orange color scale – bottom set of images) reconstruction out to 1.5 AU at the date and times shown. Various features are circled in the images which relate to various CME features from interacting CMEs which ultimately result in multiple geomagnetic storms at Earth; the *in-situ* time series from such are shown in Fig. 13.12. Earths orbit is shown as a near-circle or line with the Earth, $\oplus$, indicated on each panel. Velocity contours are shown to the left of each of the four velocity images and similarly those are also given for the density cuts. These are prime examples of how the IPS CAT can work for interacting CMEs through the inner heliosphere. (From Bisi *et al.*, 2009b)
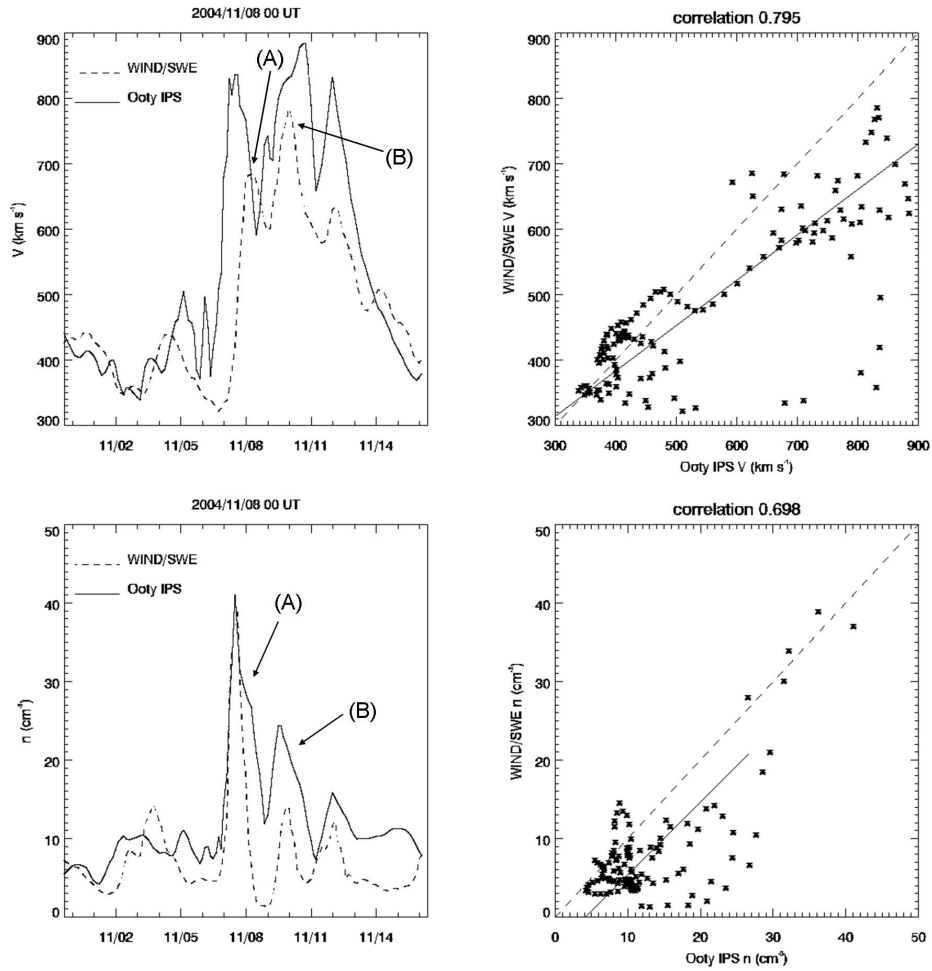
Fig. 13.12. The top-left plot compares the velocity time series at the Wind spacecraft extracted from the Ooty IPS reconstruction (solid line) with Wind solar wind velocity measurements (dashed line), and similarly the bottom-left plot for Wind density measurements. Both the Wind spacecraft velocity and density data are hourly-averaged data that were further averaged with a half-daily cadence to match that of the 3-D reconstruction cadence. The top-right plot shows a scatter diagram for the two data sets for velocity, and similarly the bottom-right plot for density; the dashed line on each correlation plot is for a 100% correlation while the solid line shows the best-fit of the data here. (A) and (B) on the left-hand plots relate to features also highlighted earlier in Fig. 13.11. (From Bisi *et al.*, 2009b)